Energy Resolution of Plastic Scintillation Detector for Neutrinoless Double Beta Decay Experiments

A dissertation

by

VO HONG HAI

Department of Physics

Graduate School of Science,

Osaka University

June, 2008

Energy Resolution of Plastic Scintillation Detector for Neutrinoless Double Beta Decay Experiments

A dissertation

by

VO HONG HAI

Department of Physics

Graduate School of Science,

Osaka University

June, 2008

ABSTRACT

Neutrinoless double beta (0ν-$\beta\beta$) decay is a key issue in current neutrino physics for studying the Majorana mass of neutrinos. 0ν-$\beta\beta$ decay is known as only the practical way to achieve the Majorana mass of neutrinos. In neutrinoless double beta decay experiment, 2ν-$\beta\beta$ decay, which has higher decay probability than that of 0ν-$\beta\beta$ decay, are considered as the background signal. 2ν-$\beta\beta$ (background signal) and 0ν-$\beta\beta$ (signal of interest) are distinguished by their beta-ray energy. Because of the finite energy resolution of the detector, 2ν-$\beta\beta$ background events are in the 0ν-$\beta\beta$ energy region of interest. Good energy resolution is necessary to reduce the 2ν-$\beta\beta$ background events in the 0ν-$\beta\beta$ region.

The next generation of double beta decay experiments, MOON and SuperNEMO, claim the sensitivity to the 0ν-$\beta\beta$ half life up to $\sim 10^{26}$ years, corresponding to mass hierarchy case inverted. They may use plastic scintillator to measure the beta-ray energy. The objective of the thesis is to study the energy resolution of the plastic scintillation detector.

Recent works have shown that the energy resolution consists of not only the statistical fluctuation, but also an "excess" fluctuation. To improve the energy resolution, we need to study the origin of this excess component. To do that, the excess component must be separated from the statistical component. In this work, the energy resolution is analyzed in separated components.

We use small plastic scintillator (6cm×6cm×1cm) with 4 PMTs covering 4 sides of plastic scintillator. This arrangement obtains high photo collection efficiency and the correlation between signals in PMTs. We employ the mono-energetic electron beams in the range of energies from 0.7 MeV to 1.7 MeV extracted from the electron spectrometer. The 0.975-MeV conversion electron from ^{207}Bi radioactive source is also used. Proton micro-beams with energies of 2.8 MeV and 3.4 MeV are used for comparison with electron data. Several additional experiments are needed to study the energy resolution.

To measure the amount of the excess component, we need to clarify the statistical component. In this work, the statistical component is obtained by the

correlation between signals in PMTs. The excess component is derived subtracting the statistical component from the total energy resolution.

There are several possibilities which may cause the excess component. In this work, we study the effect of position dependence of photo collection efficiency, the non-uniformity of the materials, different scintillator configurations (different photo collection efficiency and different thicknesses). Addition to that, the energy spread of beams, electrical noise is also discussed. The results of those studies show that, none of them can explain the excess component. Those studies suggest that the excess component is the intrinsic property of plastic scintillation detectors i.e. intrinsic energy resolution. It causes the limitation in energy resolution of the detector.

We compare the intrinsic energy resolution for electron and proton. The result shows the large intrinsic energy resolution for electrons and a small one for protons. The measured difference may be related to the difference of the energy loss process of charged particles in matter. It may tell us the hint of the origin of the intrinsic property of the plastic scintillator.

The plastic scintillation detector is limited by the intrinsic energy resolution. The energy resolution we obtain in small plastic scintillator (6cm×6cm×1cm) is close to the limitation of the detector.

We estimate the sensitivity of the detector using the plastic scintillator. Because of the limitation of the energy resolution, which we found in this work, it is hard to measure the neutrino mass region beyond inverted hierarchy case. However, it is possible to obtain around 6σ statistical significance in 10- ton·year measurement for inverted mass hierarchy case, which corresponds to the 0ν-ββ half life ∼ 10^{26} years. In short, the plastic scintillator can be used for the next generation double beta decay experiment, MOON and SuperNEMO.

Acknowledgements

Contents

1. INTRODUCTION

1.1 Overview

Neutrinoless double beta (0ν-$\beta\beta$) decay is a process beyond the Standard Model which violates lepton number by 2 units. The observation of the neutrinoless double beta decay is an exciting physics in searching for the effective mass of neutrinos and telling us that neutrinos are Majorana particles [1], [2]. Two neutrino double beta (2ν-$\beta\beta$) decay is a process in the Standard Model. It is the background event for 0ν-$\beta\beta$ measurement.

There are several radioisotopes to be considered as sources of double beta decays. Molybdenum isotope (^{100}Mo) is a source of 0ν-$\beta\beta$ decays with a high Q-value of 3.034 MeV. ^{100}Mo has a half-life of two-neutrino double beta (2ν-$\beta\beta$) decays $T_{1/2}^{2\nu\beta\beta}$ ~ 7.1×10^{18} years [3] with a continuous spectrum energetically. 2ν-$\beta\beta$ (background signal) and 0ν-$\beta\beta$ (signal of interest) are distinguished by their beta-ray energy. Because of the finite energy resolution of detectors, many 2ν-$\beta\beta$ background events are in the 0ν-$\beta\beta$ energy region of interest (around 3 MeV). Therefore, good energy resolution is necessary to reduce the 2ν-$\beta\beta$ background events in the 0ν-$\beta\beta$ region.

NEMO3 [3] for double beta measurement for ^{100}Mo achieved the sensitivity to the 0ν-$\beta\beta$ half life $T_{1/2}^{0\nu\beta\beta}$ up to 4.6×10^{23} years. In next-generation double beta decay experiments, MOON [4],[5] and SuperNEMO [6], claim the detection sensitivity to $T_{1/2}^{0\nu\beta\beta}$ up to ~ 10^{26} years. They will be sensitive to 0ν-$\beta\beta$, assuming the effective mass of neutrinos ~ 50 meV [2]. MOON and SuperNEMO use a plastic scintillator for measuring the beta-ray energy. From the simulation for ^{100}Mo foil shows that if the sensitivity up to $T_{1/2}^{0\nu\beta\beta}$ ~ 10^{26} years is conditioned, good energy resolution is required for the detector. The objective of the thesis is to study whether the energy resolution of the plastic-scintillator detector can meet the sensitivity of $T_{1/2}^{0\nu\beta\beta}$ up to 10^{26} years.

We study the energy resolution of the plastic scintillator detector. Recent works [7],[8] show that energy resolution comes from not the statistical component, but also an excess component. To improve the energy resolution, we need to study the origin of this excess component.

In this work, we study the energy resolution in statistical and excess components. The statistical component is obtained by the correlation between signals in PMTs. The excess component is derived subtracting the statistical component from the total energy resolution.

Several additional experiments are needed to study the origin of the excess component. They are (1) position dependence of photo collection efficiency, (2) uniformity of plastic materials and (3) different scintillator configurations on the excess component. Energy spread of beams and electrical noise are also measured. In addition to that, we compare that for electron and proton.

The results of those studies of the energy resolution are used to discuss the sensitivity to the 0ν-$\beta\beta$ signals for next generation double beta decay experiments, MOON and SuperNEMO.

1.2 Neutrino mass and double beta decay

In recent years, experiments have discovered that neutrinos have nonzero mass and mixings, and have pinned down many of the associated parameters. Although we now know the differences in the mass squares, we do not know the mass of the lightest neutrino, nor the mass hierarchy. Neutrinoless double beta (0ν-$\beta\beta$) decays have potential to show us about these matters.

0ν-$\beta\beta$ decay is a process beyond the Standard Model which violates lepton number by 2 units [2]. The discovery of this decay would be experimental proof that the neutrino is a Majorana particle. It would also constrain the mass spectrum and the absolute mass of the neutrinos.

1.2.1 Neutrino mass

All matters are constructed with quarks and leptons, which is shown in Table 1.2.1. The mass of these particles have almost discovered. However, for neutrinos, the absolute mass has not yet observed experimentally.

Recent experiments (Super Kamiokande [9], SNO [10], KamLAND [11], etc.) on the neutrino oscillation for the solar, the atmospheric and the reactor neutrinos provide evidences for the neutrino mass square differences and the mixings. Table 1.2.2 shows the measured mass square difference of neutrinos. However, the absolute mass of neutrino has not been measured yet, and it seems to be hard to measure the mass of neutrino directory as well as in the future.

There is another problem concerning on the neutrino mass hierarchy. When we think about the relation between the mass eigenstates, there are two solutions which are consistent with the result of neutrino oscillation experiments. These two solutions are called Normal Hierarchy (NH) and Inverted Hierarchy (IH).

Table 1.2.1 Mass of the fundamental particles of Quarks and Leptons [12]

Generation	1st	2nd	3rd
Quark	u $1.5 \sim 3$ (MeV)	c 1.25 ± 0.09 (GeV)	t 172.5 ± 2.7 (GeV)
	d $3 \sim 7$ (MeV)	s 95 ± 25 (MeV)	b 4.2 ± 0.07 (GeV)
Lepton	e^- 0.51 MeV	μ^- 105.7 (MeV)	τ^- 1776.9 ± 0.2 MeV
	ν_e -	ν_μ -	ν_τ -

Table 1.2.2 Measured mass square difference of neutrino

Atmospheric ν mass square difference, $\Delta m^2_{atm} \equiv \left| \Delta m^2_{23} \right|$ ($\times 10^{-3}$ eV^2) [13]	$1.9 < \Delta m^2_{atm} < 3.0$
Solar ν mass square difference, $\Delta m^2_{solar} = \left| \Delta m^2_{12} \right|$ ($\times 10^{-5}$ eV^2) [14]	$\Delta^2_{solar} = 8.0^{0.6}_{-0.5}$

1.2.1.1 Neutrino oscillation

Neutrino oscillations are due to a misalignment between the flavor basis $v'\equiv(v_e, v_\mu, v_\tau)$ and the mass eigenstates $v\equiv(v_1, v_2, v_3)$, described by

$$v' = Uv \tag{1.2.1}$$

where U, the unitary 3×3 mixing matrix, is described as

$$U = \begin{pmatrix} 1 & 0 & 0 \\ 0 & c_{23} & s_{23} \\ 0 & -s_{23} & c_{23} \end{pmatrix} \begin{pmatrix} c_{13} & 0 & s_{13}e^{i\varphi} \\ 0 & 1 & 0 \\ -s_{13}e^{-i\varphi} & 0 & c_{13} \end{pmatrix} \begin{pmatrix} c_{12} & s_{12} & 0 \\ -s_{12} & c_{12} & 0 \\ 0 & 0 & 1 \end{pmatrix} \tag{1.2.2}$$

where $s_{ij} \equiv \sin\theta_{ij}$ and $c_{ij} \equiv \cos\theta_{ij}$.

The effective neutrino mass $<m_v>$ is expressed in case of the Majorana neutrinos, using the mixing coefficients and Majorana phases as

$$|< m_v >| = \left\| U_{e1}^2 \right| . m_1 + \left| U_{e2}^2 \right| . m_2 . e^{i\phi_2} + \left| U_{e3}^2 \right| . m_3 . e^{i\phi_3} \right| \tag{1.2.3}$$

where $m_{1,2,3}$ are the neutrino mass eigenvalues; $\phi_{2,3}$ are the phase for m_2 and m_3 with respect to m_1. They are either 0 or π in case of CP conservation. U's are the elements of the Weak Mixing matrix and are described as

$$\begin{aligned} U_{e1}^2 &= c_{13}^2 . c_{12}^2 \\ U_{e2}^2 &= c_{13}^2 . s_{12}^2 \\ U_{e3}^2 &= s_{13}^2 \end{aligned} \tag{1.2.4}$$

The atmospheric neutrino oscillation data [2] indicates that θ_{23} is near 45°. The solar and reactor neutrino oscillation data [2] indicates that θ_{12} is about 30° and the CHOOZ experiment [2] indicates that θ_{13} is near 0°. In addition, these experiments show values of $\Delta m_{atm}^2 \equiv |\Delta m_{23}^2| = m_3^2 - m_2^2$ and $\Delta m_{solar}^2 = |\Delta m_{12}^2| = m_2^2 - m_1^2$ as in Table 1.2.2.

1.2.1.2 Neutrino mass patterns

The measured values of Δm_{atm}^2 and Δm_{solar}^2 give the pattern of masses in two possible hierarchy schemes, shown in Fig. 1.2.1. In case of Normal hierarchy (NH), m_3 is much greater than m_1 and m_2, and In case of Invert hierarchy, $m_1 \sim m_2$ is much greater than m_3. Here, m_1 and m_2 have small splitting $\Delta m_{12}^2 \equiv \Delta m_{solar}^2$.

1.2.2 Neutrinoless double beta (0v-ββ) decay

Ordinary beta decay of many even-even nuclei is energetically forbidden. However, a process, in which a nucleus changes its atomic number (Z) by two while

simultaneously emitting two beta particles, is energetically possible for some nuclei. Such process is called double beta decay. Fig. 1.2.2 shows the decay scheme for double beta decay.

Two-neutrino double beta (2ν-ββ) decay, which is shown in Fig. 1.2.3a, is defined by

$$(A,Z) \rightarrow (A,Z+2)+2\beta+2\overline{\nu}_e , \qquad (1.2.1)$$

is an allowed second-order weak process that is observed experimentally, although its rate is extremely low. Half-lives for this decay mode have been measured at $\sim 10^{18}$ years or longer [12]. In this case, two anti-neutrinos ($\overline{\nu}_e$) brings away a part of energy (Q-value) which is provided by the decay process. Remaining energy is taken by 2 β rays. Consequently, the sum energy spectrum of these 2 β rays result in broadened.

A more interesting process, which is possible to happen, is neutrinoless double beta (0ν-ββ) decay. It is described as

$$(A,Z) \rightarrow (A,Z+2)+2\beta , \qquad (1.2.2)$$

which is shown in Fig. 1.2.3b schematically. In this decay process, no neutrinos are emitted. It is clear from equation (1.2.2) that, unlike 2ν-ββ decay, 0ν-ββ violates lepton number conservation by two and hence requires physics beyond the Standard Model. For 0ν-ββ decay, final state consists of only 2 β rays, all of Q-value is given to these 2 β rays. Therefore, the sum energy spectrum of the 2 β rays is the monochromatic energy, which has the same as Q-value energy.

One can visualize 0ν-ββ as an exchange of a virtual neutrino between two neutrons within nucleus. In this frame work of the Standard Model of weak interactions, the first neutron emits a right-handed anti-neutrino. However, the second neutron requires the absorption of a left-handed neutrino. In order for this happen, the neutrino would have to be massive so that it is not a pure helicity state, and the neutrino and anti-neutrino would have to be indistinguishable. That is, the neutrino would have to be a massive Majorana particle. Neutrinoless double beta decay is the only known practical way to determine if neutrinos are Majorana particles.

The decay rate for 0ν-ββ process is expressed as:

$$\left[T_{1/2}^{0\nu}\right]^{-1} = G^{0\nu}\left|M^{0\nu}\right|^2 \left|<m_\nu>\right|^2 \qquad (1.2.3)$$

Where, $T_{1/2}^{0\nu}$ is the half-life of 0ν-ββ.

$G^{0\nu}$ is the phase space factor (which depends on the nuclear charge Z through the wave-functions of the outgoing electrons).

$M^{0\nu}$ is the nuclear matrix elements.

$<m_\nu>$ is the effective mass of neutrino.

It is also interesting for 0ν-$\beta\beta$ experiment to discern the correct hierarchy. Fig. 1.2.4 shows the effective neutrino mass as a function of the lightest neutrino mass [43]. At high values of the minimum neutrino mass, the mass spectrum is quasi-degenerate, and bands in Fig. 1.2.4 are not resolved. For a minimum neutrino mass of about 50 meV, the degenerate band splits into two, representing the normal (m_1 lightest) and inverted (m_3 lightest) hierarchies.

Normal hierarchy (NH)   Inverted hierarchy (IH)
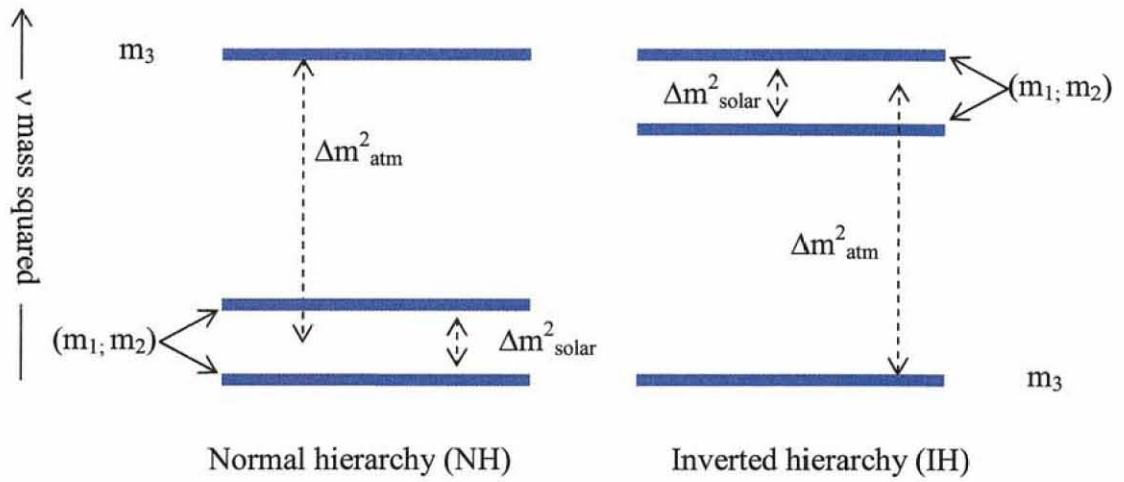
Fig. 1.2.1 Normal and inverted mass hierarchies.

$$\Delta^2_{atm} \equiv \Delta m^2_{32} \equiv \left| m^2_3 - m^2_2 \right| = (1.9 \div 3.0) \times 10^{-3} eV^2 \ [13]$$

$$\Delta^2_{solar} \equiv \Delta m^2_{21} \equiv \left| m^2_2 - m^2_1 \right| = 8.0^{0.6}_{-0.5} \times 10^{-5} eV^2 \ [14]$$
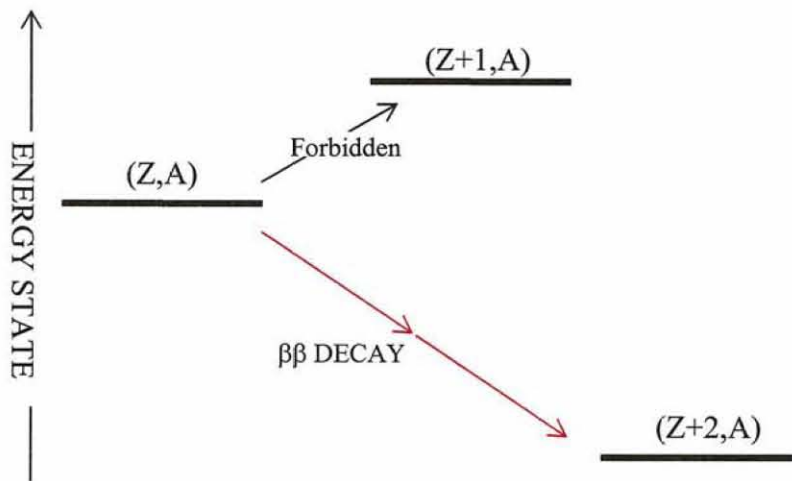
Fig. 1.2.2 Decay scheme for double beta decay. When normal beta decay is energetically forbidden, it leaves double beta decay allowable.
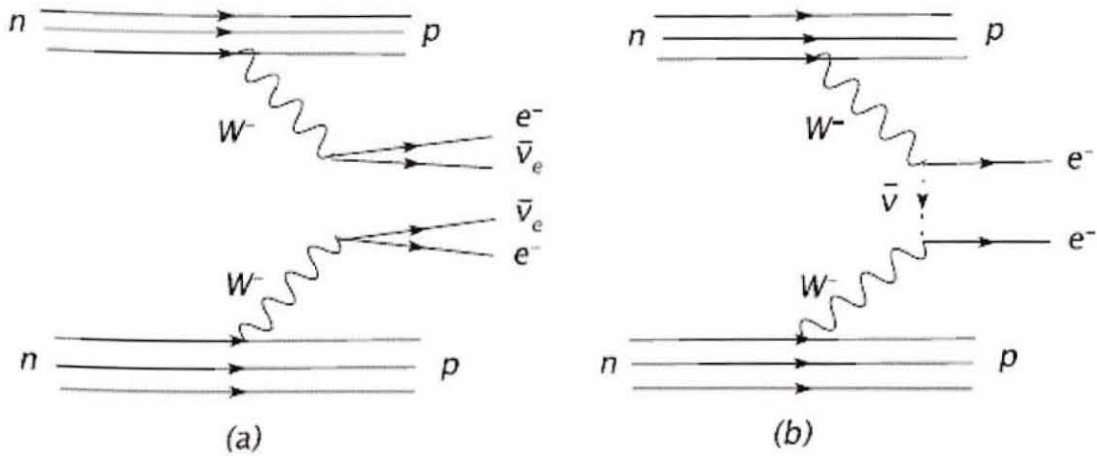
Fig. 1.2.3 Diagrams for double beta decay processes.
     a. Two-neutrino double beta decay.
     b. neutrinoless double beta decay.
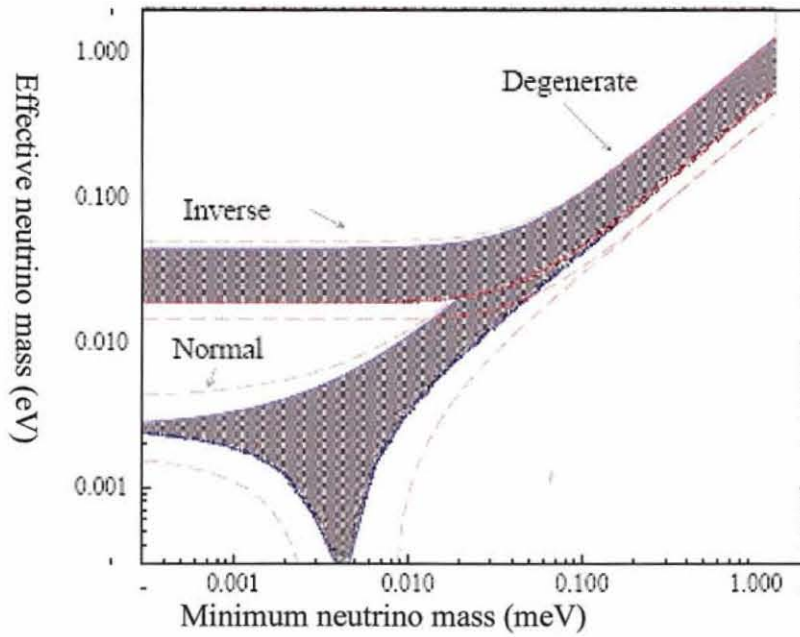
Fig. 1.2.4 The effective Majorana as a function of the lightest neutrino mass [43]. The different mass pattern is indicated in the figure. The shape region corresponds to the best values of oscillation parameters. The dashed lines indicate the expanded range corresponding to the 1-σ errors of the oscillation parameters.

1.3 MOON project

MOON (Molybdenum Observatory Of Neutrinos) project is a double beta decay experiment with a few tons of ^{100}Mo (100-Molybdenum) [5], [15]. MOON detector uses ^{100}Mo as the 0v-$\beta\beta$ decay source. Decay scheme of ^{100}Mo is shown in Fig. 1.3.1. The sum energy spectrum of two beta rays is shown in Fig. 4.1.1a. Here, the continuous spectrum is for the 2v-$\beta\beta$ decay mode, while the monochromatic peak is for 0v-$\beta\beta$ decay mode. ^{100}Mo has the large Q-value of 3.034 MeV. There are a few backgrounds from natural radioactive isotopes in the ^{100}Mo Q-value region for 0v-$\beta\beta$ detection. High natural abundance of 9.6 % is the advantage of ^{100}Mo for the enrichment of isotope. It aims at spectroscopic studies of the neutrinoless double beta decay. The MOON project is planed to probe the half-life ~ 1.2×10^{26} year (for 0v-$\beta\beta$ decay), which corresponds to the sensitivity of the effective neutrino mass down to ~ 50 meV region. The MOON detector is a multi-layer module with plastic scintillators and the enriched ^{100}Mo foils. The ^{100}Mo foil is interleaved with the plastic scintillators. The multi layers of plastic scintillator and ^{100}Mo foil are used for the MOON detector to make the detector compact. A plastic scintillator layer works as a calorimeter as well as an active shield, Fig. 1.3.2. Two beta rays from a ^{100}Mo foil are detected by two plastic scintillators which are placed above and below that foil. The other plastic scintillators are used as the active shield with purposes of reducing the radioactive background events. The MOON detector has large PMT-coverage for better photon collection efficiency.

MOON detector measured not only the half-life of 0v-$\beta\beta$ decay, but also the energy balance of 2 β rays. This would give more information of the mechanism of 0v-$\beta\beta$ decay.
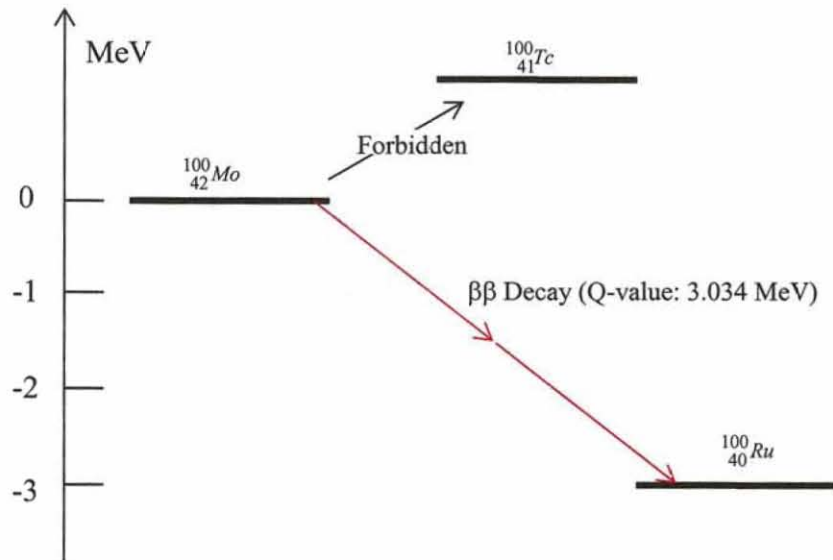
Fig. 1.3.1 ββ decay of ^{100}Mo. β decay from ^{100}Mo to ^{100}Tc is energetically forbidden. It leaves ββ decay allowable energetically.
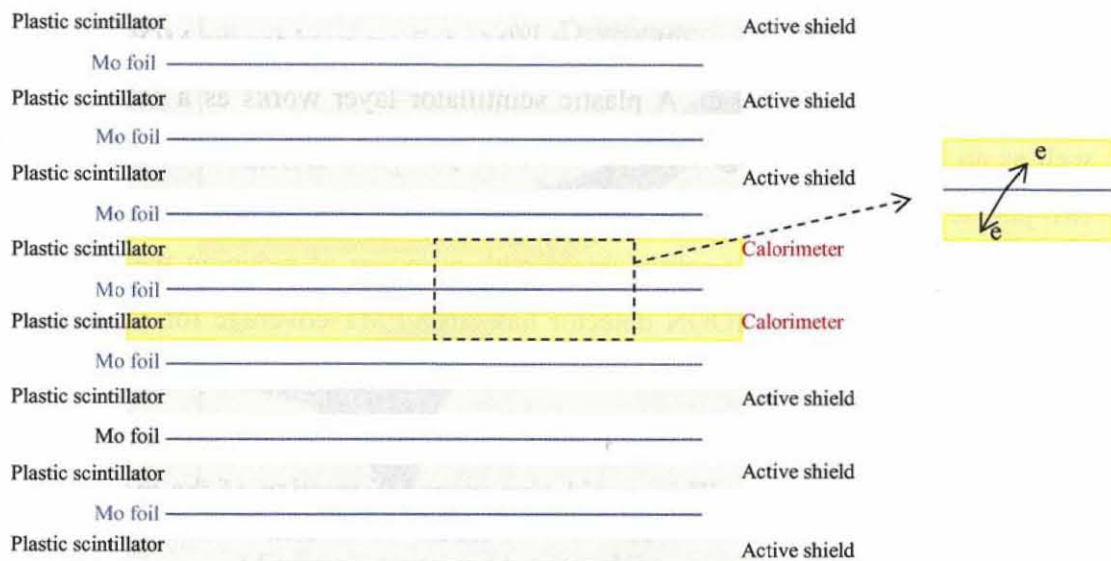
Fig. 1.3.2 The principle of MOON detector with the multi-layers of plastic scintillator. ^{100}Mo foils is interleaved the plastic scintillators. To detect ββ decay, 2 β rays are detected by two plastic scintillators which are considered as a calorimeter of 2 β rays (yellow). The other plastic scintillators are used as the active shields to reduce the background.

❖ Requirements and detection principle of MOON detector

1.3.1 Requirements

➢ **Amount of source for 0ν-ββ decay detection**

The half-life of 0ν-ββ from ^{100}Mo source is expected as $T_{1/2}^{0\nu} = 1.2 \times 10^{26} years$ assuming $<m_\nu> \sim 50$ meV [5], [15]. This means, there are about 30 decays/ton/year. Because 0ν-ββ is the very rare reactions, large amount of the decay source is needed (on order of several hundred kg to 1-ton of source foil). The detector is preferred be compact design.

➢ **Low background environment for the measurement**

The backgrounds come from the natural radioactive isotopes and cosmic rays are serious background for the measurement of 0ν-ββ decay. To reduce the cosmic background, the apparatus has to be installed in underground. A shield for background from radioactive isotopes, which exist outside, should be needed. Moreover, the experiment has to take care about the contamination inside the detector components themselves, such as ^{208}Tl and ^{214}Bi. The required level of purity of ββ source foil is a few microBequerel per kilogram in the two isotopes ^{208}Tl (<2 μBq/kg) and ^{214}Bi (<10 μBq/kg) [6]. The detector should be simple and must use pure materials.

➢ **Energy resolution of detector and thickness of the decay source material**

The ultimate background for 0ν-ββ decay detection is 2ν-ββ decay. The decay rate of 2ν-ββ is higher than that of 0ν-ββ on order of $10^5 \sim 10^7$. In the case of ^{100}Mo, the half-life of 2ν-ββ is $T_{1/2}^{2\nu} = 7.1 \times 10^{18}$ years [3], while that of 0ν-ββ is predicted as $T_{1/2}^{0\nu} = 1.2 \times 10^{26}$ years, assuming the effective neutrino mass of 50 meV. 2ν-ββ (background signal) and 0ν-ββ (signal of interest) are distinguished by their beta-ray energy. However, their energies are broadened by finite energy resolution of the detector and energy loss in the source. The broaden peak of 0ν-ββ decay will be buried in the higher tail of 2ν-ββ decay. To separate these two reactions, the detector should have good energy resolution, and the source foil should be thin to make energy loss of β rays small.

MOON detector will give the solution for the above requirements by using plastic scintillator plates and ^{100}Mo foil. MOON detector is designed with high photon collection efficiency by using photomultiplier tubes (PMT) to cover all sides of the plastic scintillator.

1.3.2 Detection principle of 0v-ββ decay by MOON detector

2-β rays from ββ decay in ^{100}Mo foil will deposit all their energy into the adjacent plastic scintillators which are considered as a calorimeter. The other plastic scintillators work as the active shields to reduce the background events and select true ββ decay events.

The advantage of MOON detector is a plastic scintillator played two important roles. One is as the calorimeter for β ray, and other is as the active shield. It makes the detector compact.

1.4 Requirement of energy resolution for 0v-ββ signals

The 0v-ββ signals show a mono-energetic peak in the summed spectrum. 2v-ββ (background signal) and 0v-ββ (signal of interest) are distinguished by their beta-ray energy, shown in Fig. 1.4.1a. Because of the finite energy resolution of the detector, many 2v-ββ background events are in the 0v-ββ energy region of interest (around 3 MeV).

The example of the energy spectrum of double beta decays with finite energy resolution is estimated by Monte-Carlo simulation. The details of the simulation are referred to Appendix B. Fig. 1.4.1b shows the prediction spectrum at the endpoint region of 2v-ββ tail, where the 0v-ββ signal appears. It is for $N_{2v\text{-}\beta\beta}/N_{0v\text{-}\beta\beta}$ ratio of 10^5, energy resolution of 6.8 % (FWHM) at Q-value of 3.034 MeV. Energy loss in ^{100}Mo foil of 40 mg/cm^2 is taken into account. The detector response is assumed as Gaussian function. No radio isotope background takes into account in this simulation.

As shown in Fig. 1.4.1b, 2v-ββ background events are in the 0v-ββ energy window. Therefore, better energy resolution is better for sensitivity to 0v-ββ.
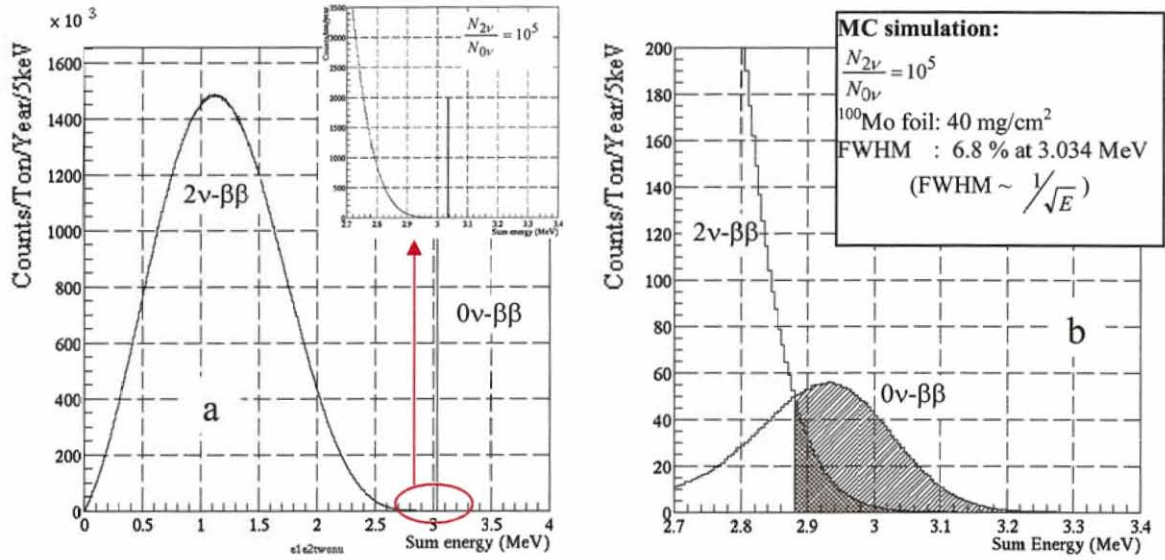
Fig. 1.4.1 The spectrum of 0ν-ββ and the background of 2ν-ββ decay.
a. Ideal condition. The 0ν-ββ peak is drawn as schematically large. The upper figure is plotted in the energy range of 2.7 MeV to endpoint for 2ν-ββ with $N_{2\nu\text{-}\beta\beta}/N_{0\nu\beta\beta}$ ratio of 10^5.
b. Spectrum with consideration of $N_{2\nu\text{-}\beta\beta}/N_{0\nu\beta\beta}$ ratio of 10^5, energy loss in ^{100}Mo foil of 40 mg/cm^2 and finite energy resolution of 6.8 % (FWHM) at 3.034 MeV. Here, 6.8 % resolution is achieved from MOON-1 detector.

1.5 Prototype MOON-1

A prototype MOON-1 detector was developed to study the energy resolution and background rejection capability as well as the feasibility of the large scale project. MOON-1 detector is a multi-layer module which was built from the 6 plastic scintillator plates (53cm×53cm×1cm) and 3 layers of enriched ^{100}Mo foils (94.5 % enrichment). Square PMTs are attached to the four sides of plastic scintillator i.e. about 82 % surface of 4 side is covered). The MOON-1 detector [16] [41] was operated at Ohto underground Laboratory from 2005 to 2006. MOON-1 detector achieved 6.8 % (FWHM) for sum energy at 3-MeV region.

1.6 Energy resolution of plastic scintillation detector

The energy resolution is discussed in this thesis for double beta decay experiment. For that reason, we need to clarify the physical processes, which cause the energy resolution. It is discussed for plastic scintillation detector.

Energy resolution of the plastic scintillator detector for incident particle can be described as a chain of the subsequent processes which happen in the plastic scintillation detector. These processes for incident particle with certain energy can be identified as: (1) energy spread before hitting the plastic scintillator, (2) energy loss

inside the plastic scintillator and UV light generation, (3) UV light absorption and the visible light emission by the wave length shifter, (4) the visible light collection at the photocathode, (5) the photoelectron production at the photocathode, (6) electron multiplication by PMT dynodes and (7) electronic analysis (analog-digital converter, etc.). Fig. 1.6.1 shows these subsequent processes. The total energy resolution of the plastic scintillation detector is an accumulation of the fluctuations in these processes.

```
┌─────────────────────────────────────┐
│  Incident-particle energy           │
│  (electrons, protons, etc.)         │
└─────────────────────────────────────┘
                 │
                 ▼
┌───┬─────────────────────────────────┐
│ 1 │ Energy spread before striking the│
│   │      plastic scintillator        │
└───┴─────────────────────────────────┘
                 │
                 ▼
┌───┬─────────────────────────────────┐
│ 2 │  Energy loss of particle inside  │
│   │  plastic scintillator and UV light│
│   │          generation              │
└───┴─────────────────────────────────┘
                 │
                 ▼
┌───┬─────────────────────────────────┐
│ 3 │ UV light transferring to the visible│
│   │         light by WLS             │
│   │     (wave length shifters)       │
└───┴─────────────────────────────────┘
                 │
                 ▼
┌───┬─────────────────────────────────┐
│ 4 │  Visible light collection at the │
│   │         photocathode             │
└───┴─────────────────────────────────┘
                 │
                 ▼
┌───┬─────────────────────────────────┐
│ 5 │  Photoelectron production at     │
│   │         photocathode             │
└───┴─────────────────────────────────┘
                 │
                 ▼
┌───┬─────────────────────────────────┐
│ 6 │  Multiplication by PMT dynodes   │
└───┴─────────────────────────────────┘
                 │
                 ▼
┌───┬─────────────────────────────────┐
│ 7 │     Electronic analysis          │
│   │  (Electronic process, ADC, etc.) │
└───┴─────────────────────────────────┘
```

Fig. 1.6.1 Schematic diagram of a chain of subsequent processes in the plastic scintillation detector.

- 23 -

1.7 Correlation between signals in PMTs

In this work, we study the energy resolution of the plastic scintillation detector in separated components. The analysis of the separated components is based on the correlation of signals in PMTs. They are the "correlated" and "uncorrelated" components. Its theoretical consideration is discussed in Appendix A. This section will discuss these components, which is used in the work.

Uncorrelated and correlated components

The total energy resolution of the plastic scintillation detector can be separated into the "uncorrelated" and "correlated" components. In the work, we study the correlation of the number of photoelectrons between PMT_{13} and PMT_{24}. Here, PMT_{13} is the summed number of photoelectrons of PMT1 and PMT3; PMT_{24} is the summed number of photoelectrons of PMT2 and PMT4. The arrangement of PMTs is shown in Fig. 2.1.1.

- The correlation studies the variance of PMT_{13} + PMT_{24} (ADD) and that of PMT_{13} − PMT_{24} (SUB). *The uncorrelated component* affects the variance of ADD and variance of SUB. It comes from (1) the statistical fluctuation of number of photoelectrons, (2) the variance of the electron multiplier gain ε, (3) the incoherent electrical noise, etc.

- *The correlated component*, which affects only the variance of ADD, comes from the common fluctuation.

- Fig. 1.7.1 illustrates the correlation of signal between PMT_{13} and PMT_{24}. The circle illustrates the uncorrelated component. The ellipse illustrates the uncorrelated and uncorrelated components.

- An example of the correlation of the number of photoelectrons between PMT_{13} and PMT_{24} for a measurement of 1.0-MeV electron beam is shown in Fig. 1.7.2a. Fig. 1.7.2b is the spectrum of total resolution in 4 PMTs ($PMT_{13}+PMT_{24}$). Fig. 1.7.2c is the spectrum of the subtraction of the number of photoelectrons between PMT_{13} and (PMT_{24} - PMT_{13}), i.e. the uncorrelated component.
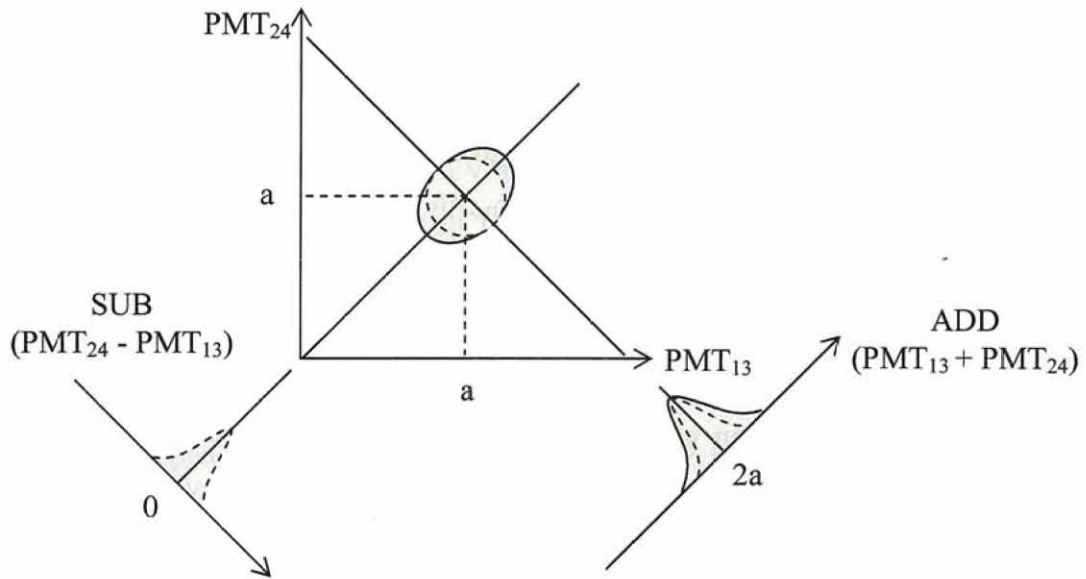
Fig 1.7.1 The illustration of the correlation signals between PMT$_{13}$ and PMT$_{24}$. "SUB" is for (PMT$_{24}$ − PMT$_{13}$). "ADD" is for (PMT$_{13}$ + PMT$_{24}$). "a" is the peak position.

  a. The circle illustrates the uncorrelated component.

  b. The ellipse illustrates the effect of the uncorrelated and uncorrelated components.
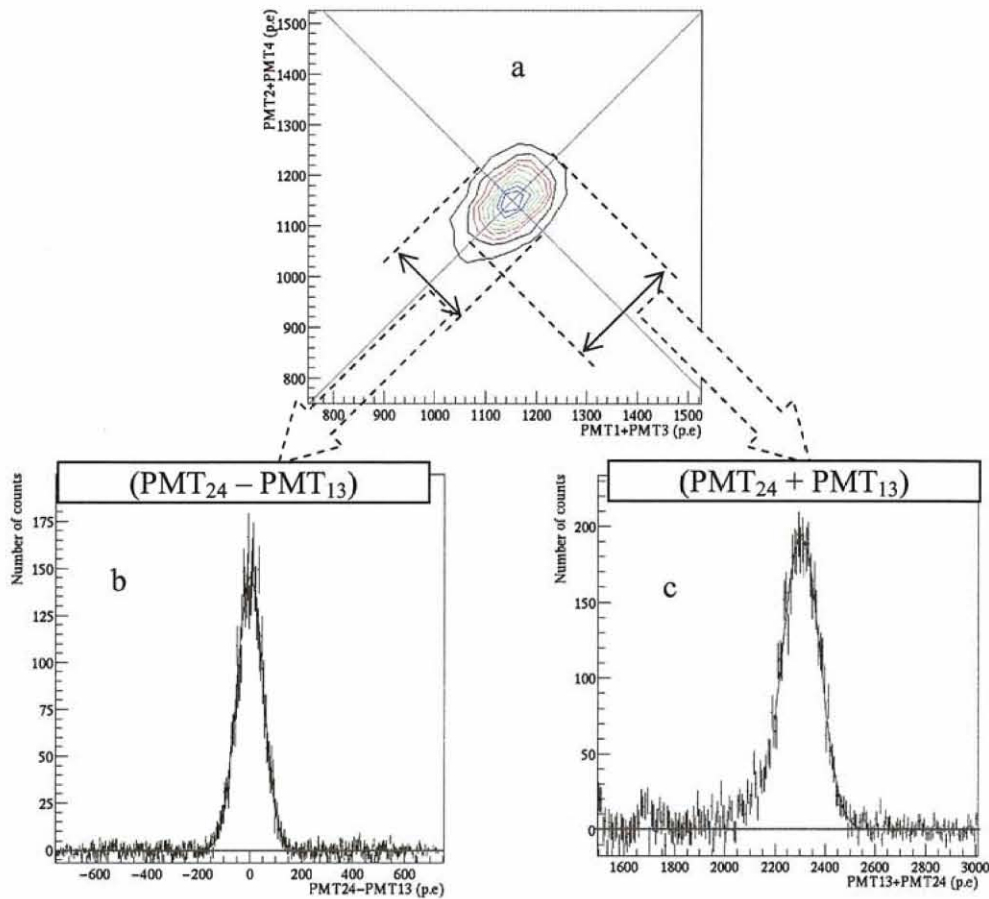
Fig 1.7.2 An example of the correlation of the number of the photoelectrons between PMT$_{13}$ and PMT$_{24}$ for a measurement of 1.0 MeV electron beam.

  a. The correlation of photoelectrons between PMT$_{13}$ and PMT$_{24}$.

  b. The spectrum of the subtraction of PMT$_{13}$ from PMT$_{24}$.

  c. The spectrum of the summed number of photoelectrons of PMT$_{13}$ and PMT$_{24}$.

1.8 Motivation of the thesis

Next generation double beta decay experiments, MOON and SuperNEMO, claim the sensitivity to the 0v-$\beta\beta$ half life up to 10^{26} year. Better energy resolution is one of the key to achieve high sensitivity to 0v-$\beta\beta$ signals. MOON and superNEMO use plastic scintillator to measure the beta-ray energy. Therefore, it is important to study the energy resolution of plastic scintillator.

There have been many works for the improvement of the energy resolution by increasing photon collection efficiency or PMT quantum efficiency to reduce the statistical fluctuation. However, the improvements were less than they expected. They claim it is because of an excess component in the total energy resolution [7],[8],[17]. To improve the energy resolution, it is necessary to study the origin of the excess component.

We study the excess component. To do that, the excess component must be separated from the statistical component. We analyze the energy resolution in components.

To obtain the excess component, we need to confirm the statistical component. In the previous works [7],[8], the statistical component is evaluated by the calculation from the number of photoelectrons. The way to obtain the number of photoelectrons is extrapolated from the single photoelectron measurement. It may contain large systematic error. We introduce another method to obtain the statistical component. This method is based on the correlation measurement of the number of photoelectrons in PMTs. In this work, we discuss the statistical component by both methods.

In the excess component, there are several possible origins. In this work, we study the effect of (1) position dependence of photo collection efficiency, (2) uniformity of plastic materials and (3) different scintillator configurations on the excess component. Energy spread of beams, electrical noise and rate dependence gain shift in PMT are also measured.

Addition to that, we compare that for electron and proton. It also may say us the hint of the origin of the excess component.

With the obtained results about the energy resolution of the plastic scintillator, we discuss the sensitivity of the 0v-$\beta\beta$ signals using the plastic scintillator for next generation double beta decay experiments, MOON and SuperNEMO.

In this thesis, we employ electron beam, proton micro-beam, the 0.975-MeV internal-conversion electron. Electron beams in the range of energies from 0.7 MeV to 1.7 MeV are extracted from the electron spectrometer at CENBG, France [18]. Proton micro-beams with energies of 2.8 MeV and 3.4 MeV are at the Wakasa-wan Energy Research Center (WERC), Japan [19]. The 0.975-MeV internal-conversion electron is from ^{207}Bi radioactive source [20]. It is used for comparison with electro-beam energy.

The following subjects are discussed in this thesis:

- Rate-dependence gain shift of PMTs (section 2.1.2.3).

- Energy spread of electron beam and proton micro-beam (section 2.2.3 for electrons and 2.4.3 for protons).

- Position dependence of the photo collection efficiency (section 2.2.4).

- The compact data taking system. Design logic trigger for data acquisition (DAQ) using Trigger module. Almost experiments in the thesis are carried out outside Osaka e.g. CENBG Lab, France and Fukui, Japan (section 2.5).

- Study the total energy resolution in components for electrons and protons based on the correlation between signals in PMTs (section 3.3 and 3.4).

- Uniformity of plastic scintillator materials (section 3.5).

- Energy resolution with different thicknesses (section 3.6).

- Increase photo collection efficiency (section 3.7).

- Evaluation of energy resolution for sum energy of 2-β rays (section 4.3).

- Sensitivity significance to 0ν-ββ signals using different finite energy resolution (Section 4.5).

- Theoretical consideration for determining the statistical fluctuation based on the correlations of the number of photoelectrons in PMTs (Appendix A).

- Simulation for the sensitivity to 0ν-ββ signals. (Appendix B).

2. EXPERIMENT

In this chapter, we describe (1) the detector arrangement, (2) the set-up for electron-beam, radioactive electron source and proton beam, and (3) data taking system. In the section of detector arrangement, we show the advantages of the set-up design. The photomultiplier tubes (PMT) used in the detector are checked their characteristics such as the output response, rate-dependent of gain shift and the response for the single photoelectron. For electron-beam measurements, we employ mono-energetic electron beams from the electron spectrometer at CENBG (Le Centre d'Études Nucléaires de Bordeaux Gradignan), France [18]. The 0.975-MeV conversion electron from ^{207}Bi source is used for comparison purpose with the electron beam data. For proton measurements, we employ the mono-energetic proton micro-beams at the Wakasa wan Energy Research Center (WERC), Japan [20]. The data taking system and the FPGA trigger system are also described.

2.1 Detector set-up

2.1.1 Plastic scintillation detector

The plastic scintillation detector, shown in Fig. 2.1.1, is BC-408 [21] with the size of (6cm×6cm×1cm), covered by four square PMTs of 6cm×6cm faceplate, typed R6236-01 [22]. Each PMT is optically coupled to each side of the plastic scintillator over an area of (6cm×1cm) by the silicon optical grease BC-630 [23]. The refraction index of the grease is 1.465. The count rate dependence of PMTs is experimentally observed within 1 %, described at section 2.1.2.3. The photon collection of four PMTs in this set-up is expected to be about 78 % in total. This number is assumed with total reflection on the surface and no absorption in the plastic. Photon yield of BC-408 at an electron kinetic energy of 1.0 MeV is around 10^4 photons [21]. Each PMT is covered by 3 layers of the 0.12-mm thick magnetic shielding sheet, typed F1AH0535 [24], so as to reduce the effect of the magnetic field from outside. PMTs are labeled from 1 to 4 (Fig. 2.1.1). Characteristics of the plastic scintillator BC-408 is discussed in Appendix C.
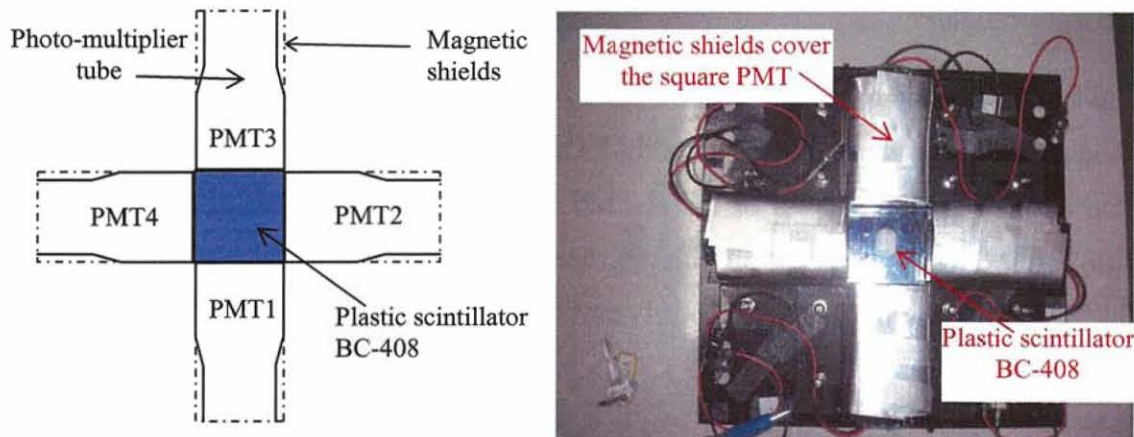
Fig. 2.1.1 Schematic view of the experimental arrangement of the plastic scintillation detector showing 4 PMTs surrounding the scintillator BC-408.

The scintillation detector set-up we used has the advantages as follows:

- High photon collection efficiency.

- Multi PMT system allows one to analyze the correlation between of signals in PMTs.

- Small position dependence of photo collection efficiency for studying the energy resolution in terms of the separated components. In other words, the probability of the scintillation photons come to PMT1+PMT3 and to PMT2+PMT4 is equal (almost no position dependence of photo collection efficiency) when incident particle hit the plastic scintillator. This advantage is used to measure the uncorrelated component to determine the statistical uncertainty of the signal from PMTs.

- The arrangement of PMTs is designed similar to the concept of MOON detector [5], [16] i.e. PMTs are optically connected all 4 sides of a plastic scintillator with small scale.

2.1.2 Photomultiplier tube

2.1.2.1 Properties of square-type PMT R6236-01

The photomultiplier tube (PMT) used in this work is a square-type PMT (R6236-1, manufactured by Hamamatsu Photonic [22]). Properties of the PMT are summarized in Table 2.1.1. The size of square PMT is shown in Fig. 2.1.2a. The area of faceplate and photocathode are (6cm×6cm) and (5.5cm×5.5cm), respectively. The quantum efficiency of the PMTs is shown in Fig. 2.1.2b (provided by Hamamatsu Photonics). The peak sensitivity of wavelength is 420 nm with quantum efficiency of 30 %. This type of PMT is sensitive for the emission spectrum of the plastic scintillator BC-408, which peak emission of the scintillation light is 425 nm.
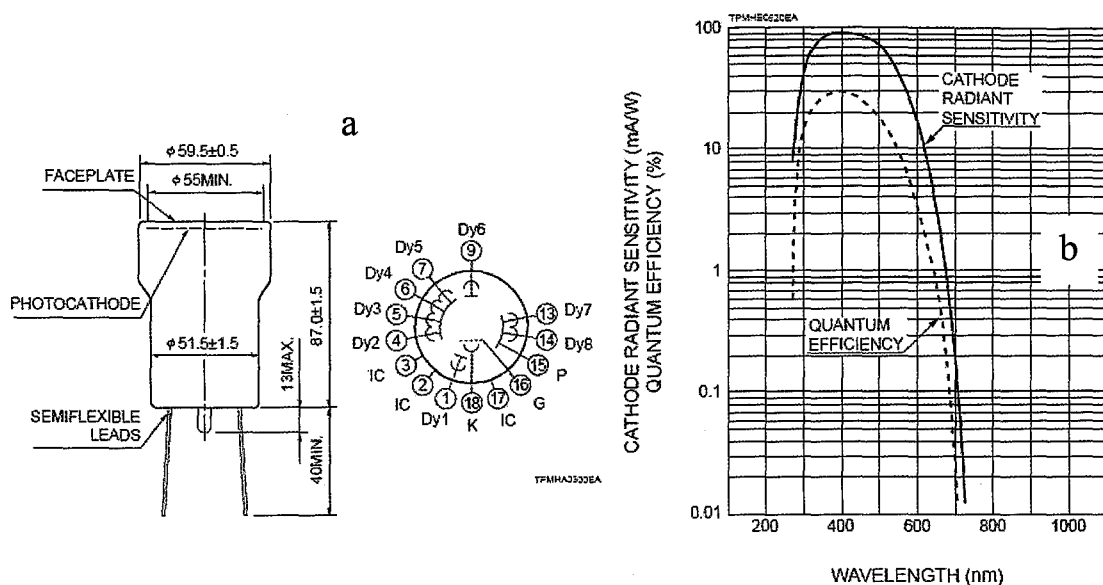
Fig. 2.1.2 Square PMT typed R6236-01 [22]

a. Technical parameters of square PMT

b. The optical properties (Quantum efficiency and cathode radiant sensitivity versus wavelength of photon).

Table 2.1.1 Key specification of the square-type PMT R6236-01 [22]

Square PMT R6236-01	Property
Size	60 mm in diameter
Sensitivity light	300 nm – 650 nm
Peak sensitivity	420 nm
Window	Borosilicate
Cathode type	Bialkali
Gain	2.7E+5
Number o dynodes	8
Typical voltage (negative)	1000 V
Max voltage (negative)	1500 V

2.1.2.2 PMT-output response

The output response of PMT (typed R6236-01) is measured and shown in Fig. 2.1.2. The PMT is illuminated by a LED light of 470 nm in wavelength, typed NSPB500s [25]. The output signal of the PMT is fed to the charge ADC (1000 pC full-scale, 12 bits [26]). The PMT has good logarithmic linearity up to -1500 Volt. The voltage used for the PMTs are chosen from -1100 volts to -1500 volts.
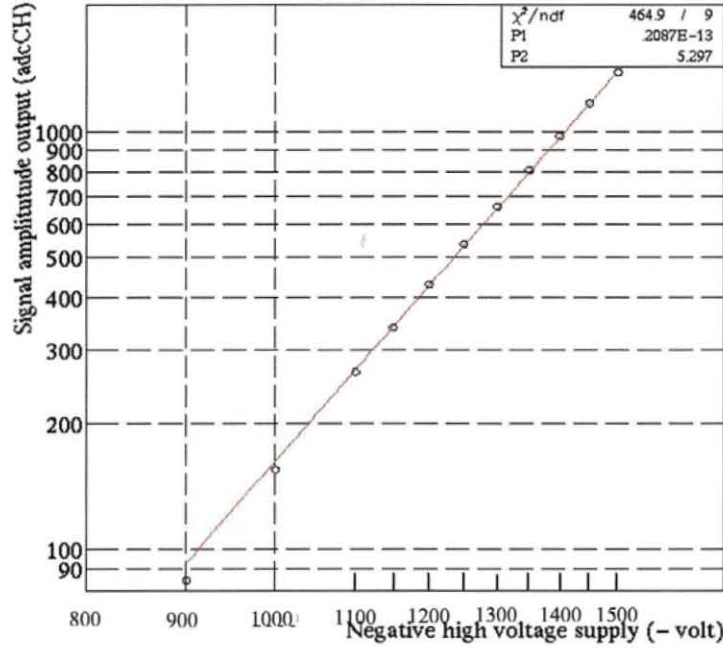
Fig. 2.1.3 The PMT gain as a function of the negative high-voltage supply volt.

2.1.2.3 Rate-dependent gain shift

The gain shift of PMTs can be caused by the change of the count rate of incident particle on the scintillation detector. It affects the measurements of the energy resolution of the plastic scintillator. Therefore, it is necessary to check the rate-dependent gain shift of the PMTs which are used for the measurements. The PMTs used in this work are square PMT, typed R6236-01 [22].

In order to measure the rate-induced gain shift on PMT, two LEDs are employed. It is described briefly as follow:

One LED, which is defined as a reference LED, is pulsed at 20 counts/sec. The gain of PMTs adjusts to produce electric charge corresponding to about 1.0-MeV electrons. This LED is pulsed at fixed rate to make light output of the LED stable if there is no addition light come to the PMT. The other LED, which is defined as a

background LED, is pulsed at the adjustable rate from 20 counts/sec to 1000 count/sec with a charge/pulse approximately of the reference LED's. Those LEDs are the blue-light LED of 470 nm in wavelength (typed NSPB500s, manufactured by NICHIA [25]). The LED reference and the LED background are supplied by two different Pulse Generators. Schematic diagram of the two-LED set-up is shown in Fig. 2.1.4. A charge analog-digital converter (1000 pC full-scale, 12 bits [26]) is used to digitize the PMT-charge output of the reference LED. A 1-count/sec trigger is used to measure the stability of the pedestal signal of the system. Fig. 2.1.5 shows the gain shift plotted against the count rate of the background LED for a PMT type R6236-01. Experimental results show that the rate-dependent gain shift for these PMTs is negligible (within 1 %) with background-LED rate up to 1000 counts/sec. The PMT is stable for the change of count rate in proton experiments. The count rate of the proton micro-beam used the proton experiments is on order of hundreds counts/sec and varied in time. Other square PMTs are checked with similar results i.e. have a small rate-dependent gain shift.
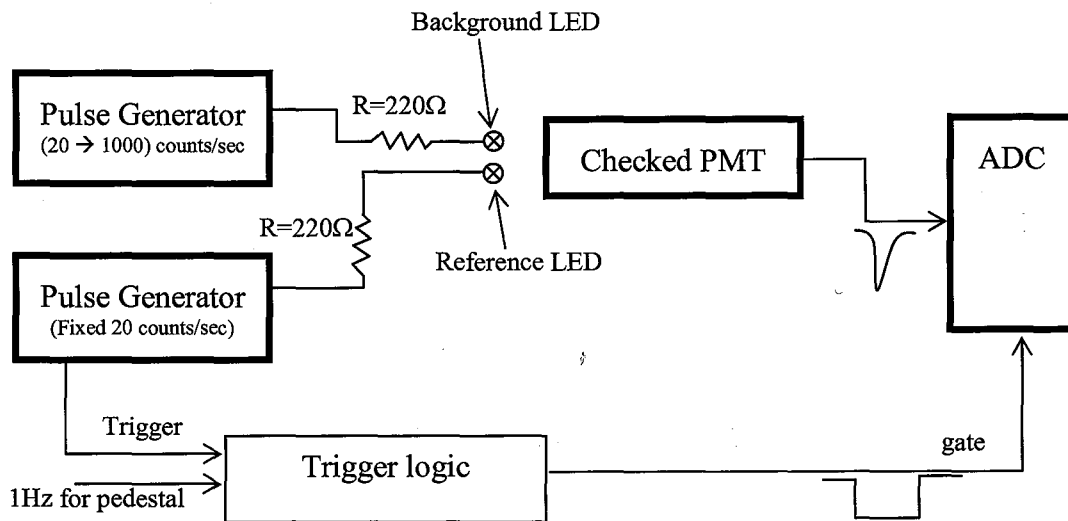
Fig. 2.1.4 Schematic diagram of the two-LED set-up for measuring the PMT gain shift. Count rate of reference is fixed at 20 counts/sec; and count rate of background LED is adjustable from 20 counts/sec to 1000 counts/sec. 1-count/sec pedestal trigger is for monitoring pedestal signal.
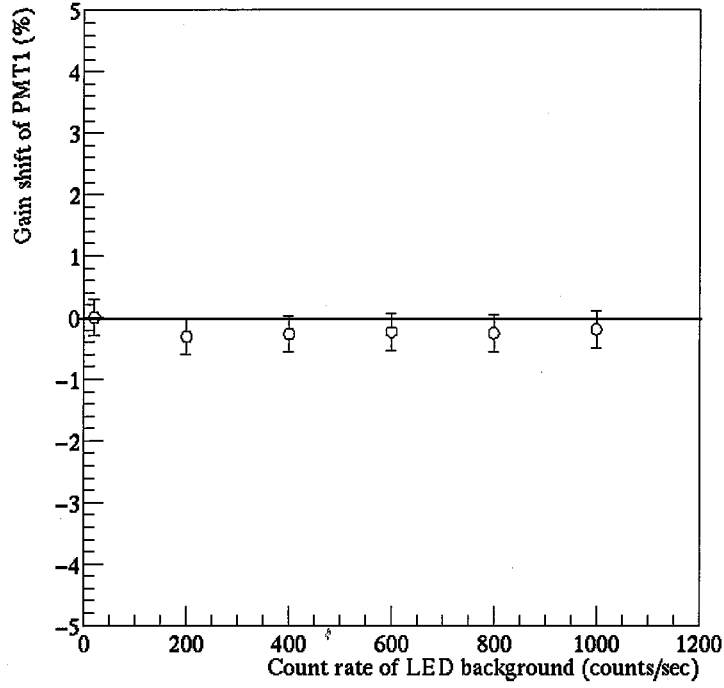
Fig. 2.1.5 The rate-dependent gain shift of the square PMT(type of R6236-01) is negligible with rate of the background LED up to 1000 Hz. Rate-dependent gain shift for the PMT is negligible (within 1 %). It is good for proton measurements.

- Count rate of reference LED is fixed at 20 counts/sec.
- Count rate of background LED is adjustable from 20 to 1000 counts/sec

2.1.2.4 Single-photoelectron measurement

The single photoelectron measurement is an important for evaluating the performance of the PMT as well as the scintillation detector. It is used to evaluate the statistical fluctuation for the energy resolution measurement.

In order to describe a charged-particle spectrum in terms of the number of photoelectrons, the single-photoelectron peak is measured by using the photons from a blue LED (NSPB500S, NICHIA [25]), which illuminates the photocathode of the PMT. The PMTs (typed R6236-01) can obtain the single-photoelectron spectrum. The single photoelectron spectrum of a PMT (type R6236-01) is shown in Fig. 2.1.6 with high voltage supply of -1500 volt. The histogram is fitted in terms of the Poisson distribution for the photoelectron distribution and the Gaussian distribution for the PMT gain fluctuation. The fitting formula is described as:

$$f(x) = P_4 \sum_{n=1}^{} \frac{P_1^n e^{-P_1}}{n!} \times \frac{1}{P_3 \sqrt{2\pi n}} e^{\frac{-(x-nP_2)^2}{2nP_3^2}} \tag{2.1.1}$$

- 33 -

Where: P_i (i = 1 - 4) are fitting parameters with the meaning as follows:

P_1: Average of number of photoelectrons

P_2: ADC channel / photoelectron

P_3: Resolution of single photoelectron

P_4: Normalization parameter

For this PMT, the single photoelectron is obtained at (2.53 ± 0.03) ADC channel, which corresponds to 0.6 pC, at high voltage of -1500 volts. The error is evaluated from statistical error of the measurement. All PMTs employed can see the single photoelectron with high voltage of -1500 volts. The actual voltage used for the measurement is set around -1200 volts. The number of photoelectrons can be calculated from the relationship between ADC channel and high voltage curve which is discussed in section 2.1.2.2. Thus, (2.53 ± 0.03) ADC channel per single photoelectron at -1500 volts corresponds to (0.78 ± 0.01) ADC channel per single photoelectron at -1200 volts. Here, PMT gain is evaluated as 3.26 (2.53/0.78).
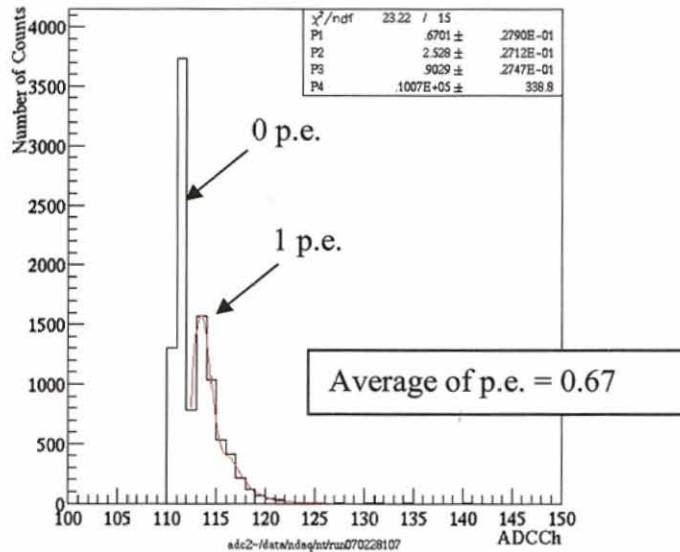
Fig. 2.1.6 The single-photoelectron spectrum obtained by using photons of the blue LED illustrated the photocathode of the photo-multiplier tube (type R6236-01, manufactured by Hamamatsu). The peak in the left corresponds to no photoelectron (0 p.e.). Red curve is the fitting line using Eq. 2.1.1. (n = 1÷10) p.e. peaks are fitted. Average of the number of photoelectron is 0.67.

The single-photoelectron measurement is used in evaluating a spectrum in terms of the number of photoelectrons for incident particle. It is assumed that the number of photoelectrons is proportional to the ADC channels.

2.1.2.5 Variance of electron-multiplier gain

Electron multiplication process in a PMT has statistical fluctuation. Assuming Poisson distribution in the multiplication at each dynode, i.e. gain δ causes fluctuation of $\sqrt{\delta}$, the variance of the electron multiplier gain is reflected in the pulse height resolution of the single photoelectron peak, as follow:

$$(\frac{\sigma}{E})_{1.p.e} = \sqrt{\frac{1}{\delta_1} + \frac{1}{\delta_1\delta_2} + ... + \frac{1}{(\delta_1\delta_2...\delta_n)}}$$

$$(\frac{\sigma}{E})_{1.p.e} = \sqrt{\varepsilon} \qquad\qquad (2.1.2)$$

where σ is the standard deviation on the single-photoelectron peak. It can be obtained by the fitting parameters of the single-photoelectron spectrum.

δ_i is gain of each dynode

ε is the variance of PMT gain.

From the fitting parameters of the single-photoelectron spectrum in Fig. 2.1.6, the variance of PMT gain, ε, is calculated from Equation (2.1.2) is 0.12.

2.1.2.6 Pedestal signal

The pedestal signal is measured in the plastic scintillation detector. The width of pedestal signal is less than 1-ADC channel. It is good for the measurement of the signal of interest.

χ^2/ndf	.0000E+00/ 0
Constant	269.8
Mean	125.2
Sigma	.4410
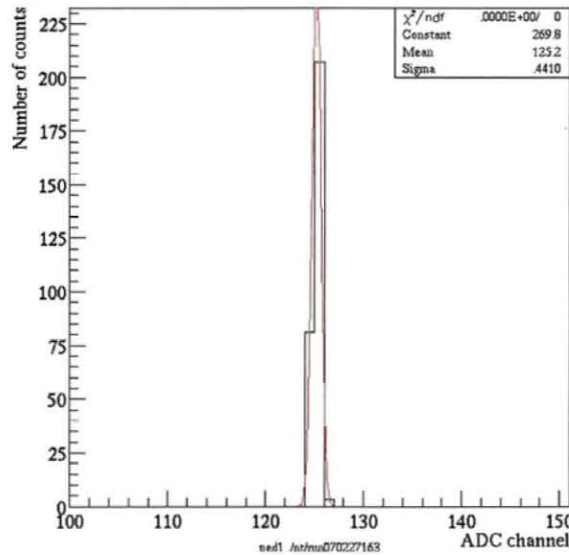
Fig. 2.1.7 Pedestal signal. The fluctuation of pedestal signal is less than 1 ADC channel.

2.2 Set up for electron-beam measurement

In this section, we describe the set-up for the measurement with electron-beam.

2.2.1 Electron spectrometer

Mono-energetic electron beams used in this work are extracted from the electron spectrometer at CENBG (Le Centre d'Études Nucléaires de Bordeaux Gradignan, France [18]). The schematic diagram of the spectrometer is shown in Fig. 2.2.1. The spectrometer analyzes electrons with energies adjustable from 0.4 MeV to 2.0 MeV. An incoming beam of electrons from the electron source is bent with the magnetic fields. The electron output can be obtained by tuning the current on the coil which is used to change the magnitude of the magnetic field. Fig. 2.2.2 shows the relationship between the current and electron energy output [18]. The radioisotope mounted in the spectrometer is a ^{90}Sr (strontium) source. Electrons from its daughter ^{90}Y (yttrium), that provided a continuous energy spectrum up to 2.2 MeV, are used. The output direction of the electron beam is vertical from bottom to top. The size of output slit is 1 mm × 1 mm. Chamber inside the spectrum is kept at vacuum by the vacuum-pump, so as to reduce the interaction of electrons with the molecules inside the spectrometer.
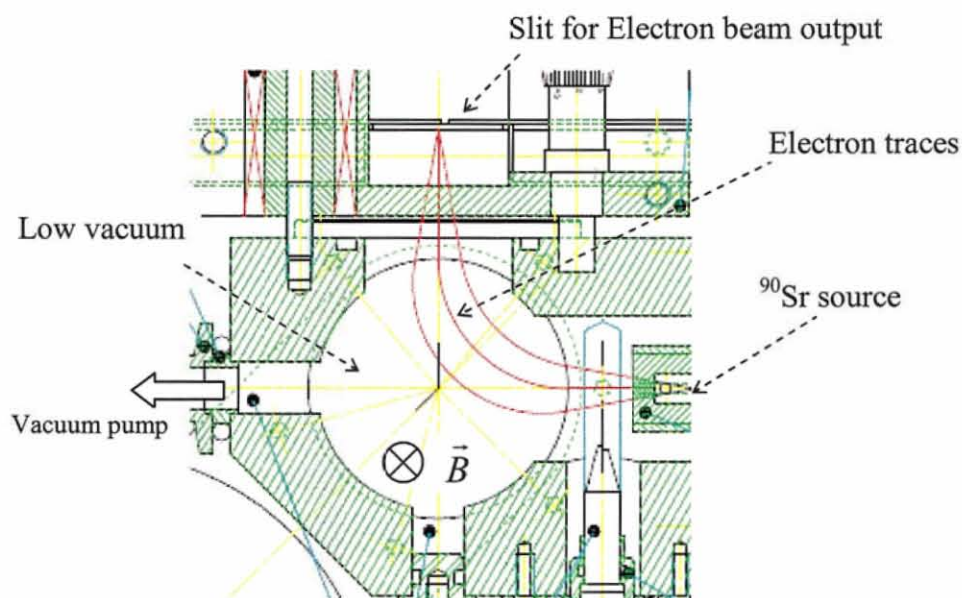
Fig. 2.2.1 Schematic view of the electron spectrometer at CENBG (Le Centre d'Études Nucléaires de Bordeaux Gradignan), France [18]
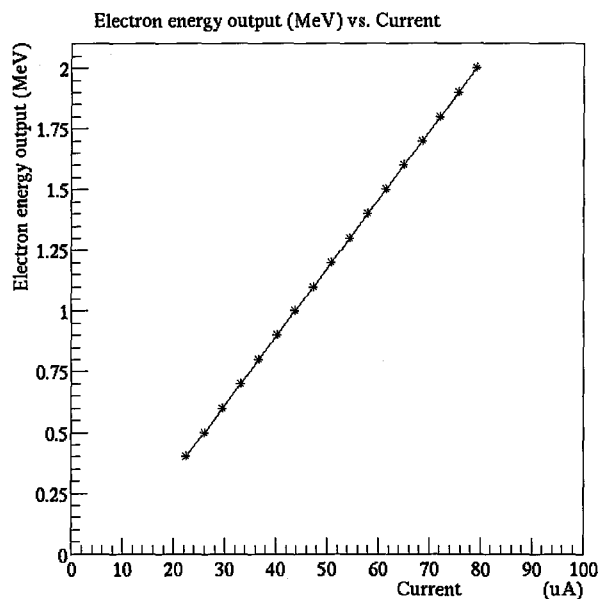
Fig. 2.2.2 Dependence of electron mono-energetic output (MeV) versus current (μA) [18]

2.2.2 Arrangement for electron-beam experiment

A schematic view for the electron measurements is shown in Fig. 2.2.3. The plastic scintillation detector is mounted inside the dark box. A 1-mm thick Pb collimator is placed at the center of the plastic scintillator in order to define the electron-beam size. The electron beam from the spectrometer irradiates the plastic scintillator through a 10-μm thick polycarbonate foil and the Pb collimator under atmospheric conditions with a distance of about 4 cm. Background radiation and electrons are both emitted at the output of the spectrometer. The main background comes from gamma rays produced by beta rays hitting inside the spectrometer (Bremsstrahlung effect). Therefore, to obtain an electron spectrum, two measurements are carried out. The first measurement is for the electron beam containing the background and the second one is for the background only. Subtract the background spectrum from the electron-background spectrum, we obtain the electron spectrum. A 5-mm thick "shutter" made of aluminum is used for stopping the electrons. Iron magnetic-shield plates are installed between the spectrometer and the dark box in order to reduce the effect of the magnetic field from the spectrometer on the PMTs. The experiment is carried out for the electron energies from 0.7 MeV to 1.7 MeV, namely, 0.7, 1.0, 1.3, 1.5, 1.7 MeV. Using a 4-mm diameter Pb collimator, the electron and background count rate are about 3 counts/sec and 7 counts/sec, respectively.
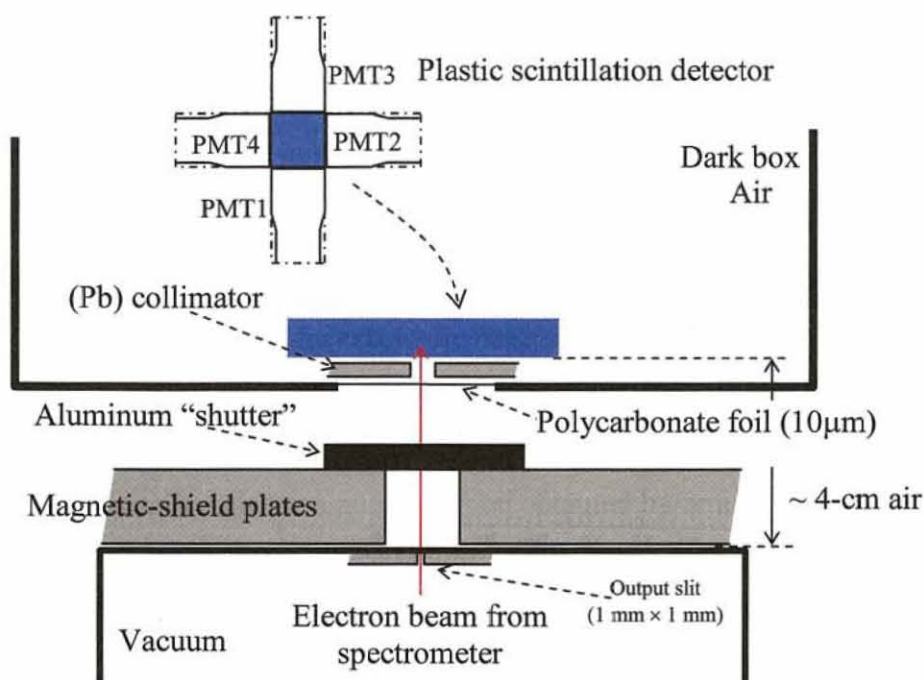
Fig. 2.2.3 Arrangement for electron measurements. To obtain an electron spectrum, two measurements are carried out using a 5-mm thick "shutter" made of aluminum. Magnetic-shield plates made of iron are employed to reduce the effect of the magnetic field from the spectrometer on PMTs. The distance from the slit of the spectrometer to the plastic scintillator is about 4 cm in air. A 10-μm-thickness polycarbonate foil is installed at the entrance of the dark box.

2.2.3 Energy spread of electron beam

The energy spread for the electron beam is measured by using high-resolution Si(Li) detector [18]. The energy resolution of the 1.0-MeV electron beam is about 1.8% at a full width half maximum (FWHM) of the peak at a distance of 4 cm above the slit of the spectrometer. This value mainly comes from the resolution of the Si(Li) detector.

2.2.4 Position of spectrometer

To put the electron beam at the center of the plastic scintillator, the moving-table apparatus is employed.

The electron spectrometer is placed on the moving-table apparatus which is controllable horizontally by a computer. The spatial resolution of the apparatus is 0.53 mm (1 digit). In order to tune the electron beam at the center of the plastic scintillator, we base on the count rate dependence of electron beam on the position of the

spectrometer. The plastic scintillation detector is mounted in the dark box. Fig. 2.2.4 shows the experimental arrangement.
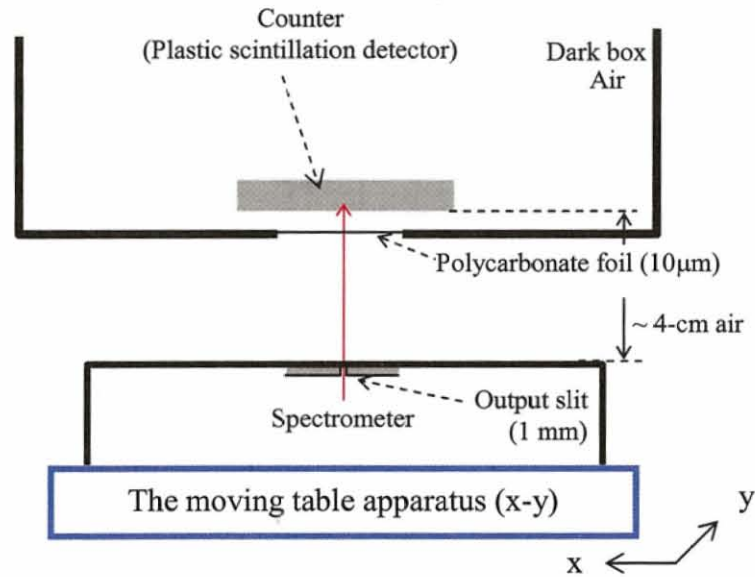
Fig. 2.2.4 The experimental arrangement for measuring the count rate dependence of electron beam on the position of the spectrometer. The spectrometer is put on the moving-table apparatus. It can move horizontally with spatial resolution 0.53 mm (1 digit).

In this experiment, we carry out just once for x-scan, and once for y-scan. To do that, at first, we rely on the previous calibration data. The center value was $(X,Y) =$ (71.02 mm, 84.24 mm) [18]. Note, values for x and y are the absolute scale of the moving-table apparatus. For X-scan, Y-value (Y = 84.24 mm) is fixed, and for Y-scan, X is fixed, (X = 71.02 mm). Fig. 2.2.5a and Fig. 2.2.5b show the count rate on x-scan and y-scan, respectively. Based on these two measurements, the center position of moving table is (X = 69.96, Y = 82.15). The count rate is measured at 58.6 counts/sec. The spectrometer is placed at this position for all electron measurements.
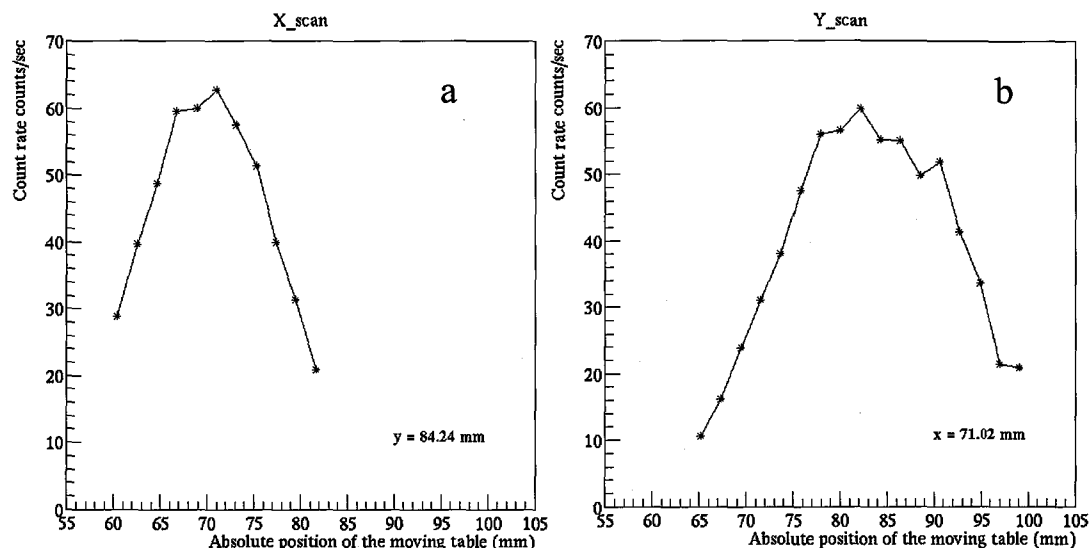
Fig. 2.2.5 Count-rate dependence on the absolute position of the moving-table apparatus

     a. X-scan, Y is fixed at 84.24 mm.

     b. Y-scan, X is fixed at 71.02 mm.

2.2.5 Beam size of electrons

To estimate the beam size of electrons at the distance of 4-cm air above the output slit of the spectrometer, two Pb-collimators of 1-mm thick (2-mm and 4-mm in diameter) are utilized to measure the count rate of electron beam. Assuming the count rate is proportional to the area of the beam cross section, the beam size without collimator is estimated. The experimental set-up for the electron beam-size measurement is shown in Fig. 2.2.6. The Pb collimator is installed below the plastic scintillator to define the beam size. The output slit of the spectrometer emits not only the electrons, but also back ground (gamma rays). To obtain the count rate of the electron beam, two measurements are carried out. The first measurement is for the electron beam containing the background, and the second one is for the background. The count rate of electron beam results from the count rate of background subtracted from that of electron beam containing background. The aluminum "shutter" is used to stop the electrons i.e. the background measurement.
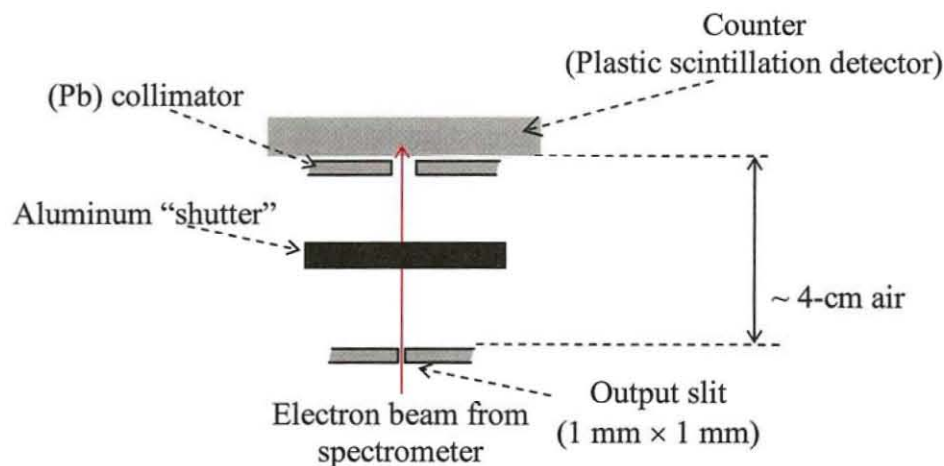
Fig. 2.2.6 Arrangement for the beam-size measurement at distance of 4-cm air about the slit of spectrometer. Two Pb collimators (2-mm ϕ and 4-mm ϕ) are used.

Fig. 2.2.7 and Table 2.2.1 show the count rate of the electrons and background. The count rate of background (black points) is measured as around 7 counts/sec. Its does not depend on the collimator size. Red points are for count rate of electron beam. Comparing the measurements with the collimators, the electron count rate is proportional to the area of hole (~ 0.06 count/mm^2). Using this, the beam size without collimator is estimated as 750 mm^2, corresponding to 15.7 mm in diameter.
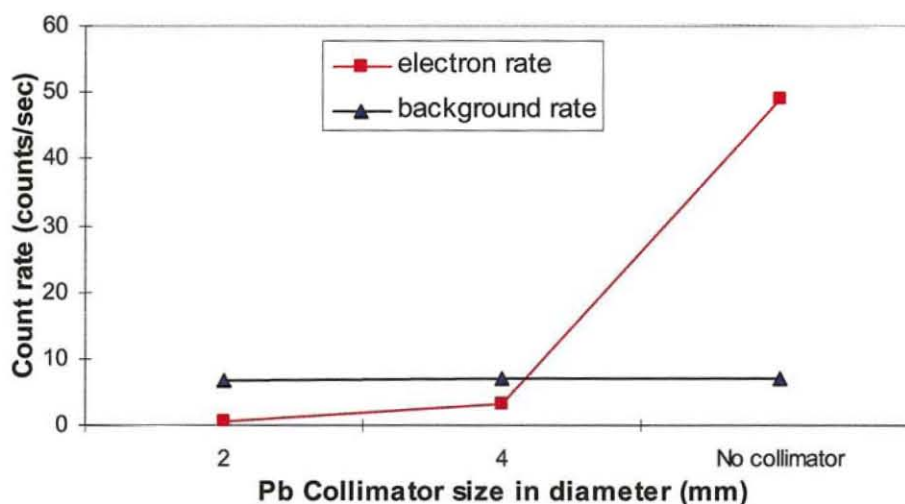
Fig. 2.2.7 Beam size of the spectrometer at the 4-cm air distance is evaluated as 15.7 mm in diameter by measuring the count rate of electron beams. The red line is the count rate of electron beam. The blue line describes the evaluation of the beam size of electrons. Count rate of background (black line) is almost constant.

Table 2.2.1 The count rate of electrons and the corresponding beam size. The beam size without collimator is evaluated by a Pb collimator of 2 mm in diameter. It is 15.7 mm in diameter. The background is almost unchanged.

Pb-collimator (mm in diameter)	2	4	No collimator
electron rate (counts/sec)	0.8	3.19	49.2
background rate (counts/sec)	6.8	6.9	7.1

2.2.6 Count rate of electron beam

Fig. 2.2.8 shows the count rate of electrons (black line) and background (red line) versus the electron energies in condition of using a 1-mm thick Pb collimator with the hole size of 4 mm in diameter. The count rate of background is almost constant.
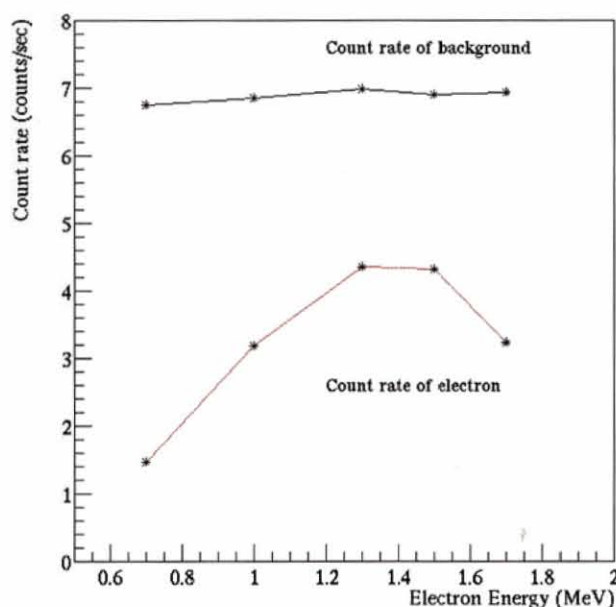
Fig. 2.2.8 Count rate of electron beam versus the electron energy with the Pb collimator (1-mm thick, 4-mm in diameter). Black line for count rate of background and red line for count rate of electrons.

2.2.7 Spectrum of mono-energetic electron beam

An energy spectrum of electron beam is plotted as the total number of photoelectrons in 4 PMTs.

Figure 2.2.9 shows the experimental result for measuring 1.0-MeV electrons, where Fig. 2.2.9a shows both the spectrum of electrons containing background (black

line) and that of background alone (red line). Figure 2.2.9b shows the electron spectrum after background subtraction. The summed number of photoelectrons in 4 PMTs is evaluated as 2300 ± 40 (photoelectrons) at 1.0-MeV electrons. The error is calculated from statistical errors in the peak fitting. The electron spectra at other energies also yield similar results.
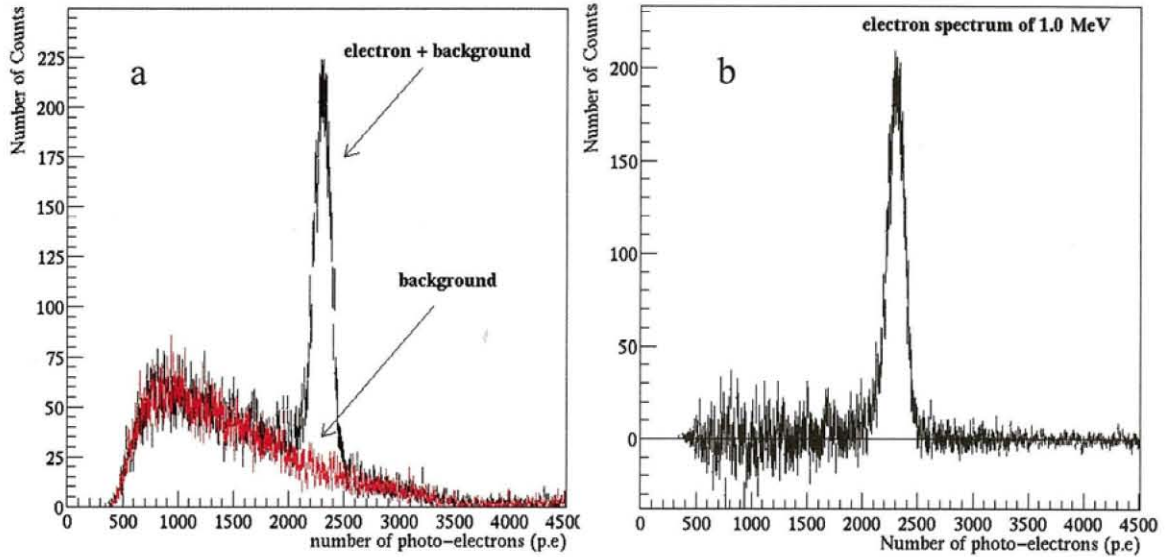
Fig 2.2.9 The spectra are plotted on the photoelectron scale for 1.0 MeV electrons
　　a. Electron-background spectrum (black) and background spectrum (red).
　　b. Electron spectrum obtained after background subtraction.

2.2.8 Selection of collimator size

Electron hit finite area of the plastic scintillator. Position dependence of photo collection efficiency in PMTs may affect measuring the components of the total energy resolution. Uncorrelated component, which is defined as the variance of the difference of signals in PMTs, is sensitive to the position dependence. This component is used to determine the statistical component in total energy resolution. In this work, the uncorrelated component is measured between PMT_{13} and PMT_{24}. Here, PMT_{13} is the summed number of photoelectrons in PMT1 and PMT3. PMT_{24} is the summed number of photoelectrons in PMT2 and PMT4. We carry out a measurement of the uncorrelated component on different electron-beam sizes. They are 2 mm, 4 mm in diameter and no collimator (equivalent to 15.7-mm collimator). We use a 1-mm thick Pb collimator. Electron beam of 1.0 MeV are utilized to measure the uncorrelated component versus the beam size. The obtained results are shown in Fig. 2.2.10 and Table 2.2.2. In the case of the 2-mm and 4-mm diameter beam sizes, their

uncorrelated component yield the same results (5.1 ± 0.2 ; 5.2 ± 0.2 ,% respectively, in FWHM). However, in the case of the 15.7-mm diameter beam size (no collimator), this component is larger (7.0 ± 0.2 , % in FWHM). These results definitely illustrate that the uncorrelated component depends on the beam size (in this set-up) when the beam size is large due to the position dependence.

A 4-mm diameter Pb collimator is chosen for this work, since no position dependence of electron-beam size (4-mm in diameter) is observed in this set-up. Moreover, the electron count rate at 4-mm diameter beam size (3.1 counts/sec) is higher than that at 2-mm diameter beam size (0.8 counts/sec), while the background count rate (7 counts/sec) is unchanged. It is good for the measurements of electrons.
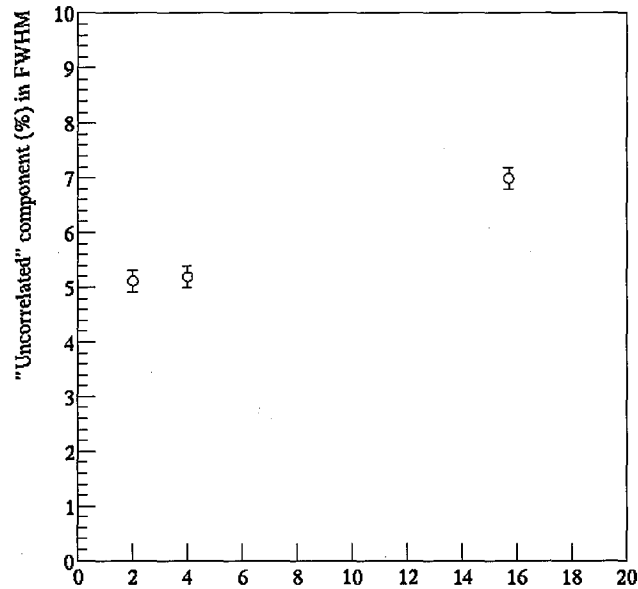
Fig. 2.2.10 Dependence of the uncorrelated component in FWHM versus electron-beam sizes. The 15.7-mm diameter beam size is equivalent a beam without use of the collimator.

Table 2.2.2 Dependence between the uncorrelated component and electron-beam size.

Electron-beam size (mm in diameter)	uncorrelated component $(PMT_{24}\text{-}PMT_{13})$ (%) in FWHM	Count rate of electron beam (counts/sec)
2 (2-mm collimator)	5.1 ± 0.2	0.8
4 (4-mm collimator)	5.2 ± 0.2	3.1
15.7 (no collimator)	7.0 ± 0.2	49.2

2.2.9 Light yield response versus electron energies

The linearity of peak positions (unit: number of photoelectrons) of electron spectra versus electron energies (MeV) is shown in Fig. 2.2.11. The peak position is derived from the Gaussian fitting for the spectrum of the summed number of photoelectrons in 4 PMTs. The results in Fig. 2.2.11 show good linearity. The deviation is within 1% in comparison to the fitting line. Here, the data points are fitted in the linear function. The errors are considered smaller than the drawing points. These results also show that there is no effect of the magnetic field from the spectrometer on the PMT gain.
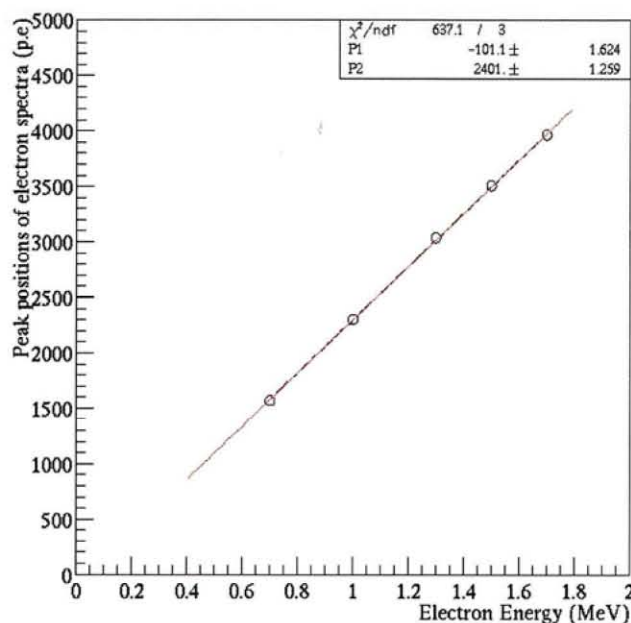
Fig. 2.2.11 Linearity of peak positions of electron spectra (photoelectrons) versus electron energies (MeV). Errors of data are smaller than drawing points. The deviation is less than 1%.

2.3 Set up for 0.975-MeV conversion-electron measurement

The 0.975-MeV conversion electron from [207]Bi is used for comparison purpose with the electron beam data.

The same plastic scintillation detector is employed for this experiment. To measure the 0.975-MeV conversion electron from [207]Bi radioisotope source of 37 kBq [20], two measurements are needed to carry out. First measurement (Fig. 2.3.1a), using the Pb collimator (2-mm in diameter, 1-mm thick) is for the beta and gamma spectrum (β+γ). Second one (Fig. 2.3.1b), using the Pb board of 1-mm thick, is for the

gamma spectrum (γ) only. The [207]Bi source is put at the center of the plastic scintillator with distance of 1-mm air. The beta spectrum is obtained from (β+γ) spectrum subtracting the γ spectrum.
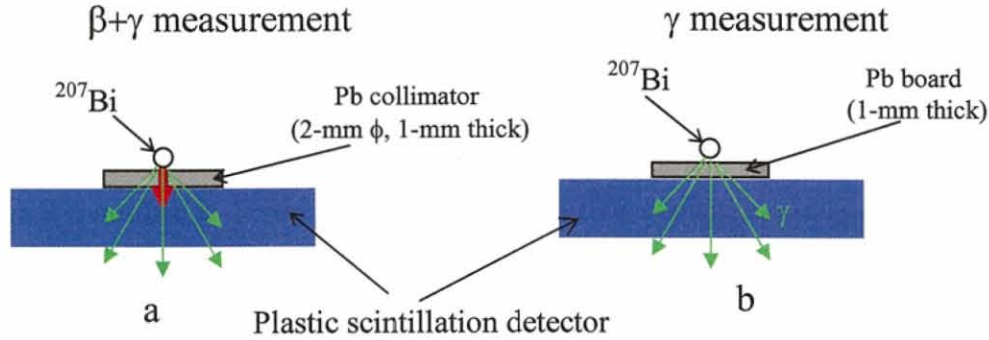
Fig. 2.3.1 The experimental arrangement for the 0.975-MeV conversion electrons from [207]Bi source. Two measurements are needed to carry out to obtain the 0.975-MeV conversion-electron spectrum.

a. Set up for (β+γ) measurement with Pb-collimator (2-mm in diameter, 1-mm thick).

b. Set up for γ measurement with the Pb board (1-mm thick).

2.4 Set up for proton measurement

In this section, we describe the set-up for the proton micro-beam measurement.

2.4.1 Proton micro-beam line

Proton micro-beam facility used in this work is located at the Wakasa-wan Energy Research Center (WERC), Japan [19]. A schematic view of the proton beam line is shown in Fig. 2.4.1. The beam line consists of three slit systems (S1, S2, and S3), an analyzing magnet, an electric scanning system, a magnetic quadrupole doublet (Q doublet) and a target chamber. The image at slit S1 is focused on slit S2. The formation of the micro-beam on the sample is derived from using slit S2 as an object slit, the aperture S3 and the magnetic quadrupole doublet. Aperture S3 limits the angular divergence of the beam. The demagnification factors are different in the horizontal and the vertical planes, where the horizontal and the vertical demagnifications are designed to be 5 and 19, respectively. The slit widths of S2 are adjustable independently in horizontal and vertical directions with a step interval of 2 μm. The magnet is aligned so that the spot size is minimized on the sample.
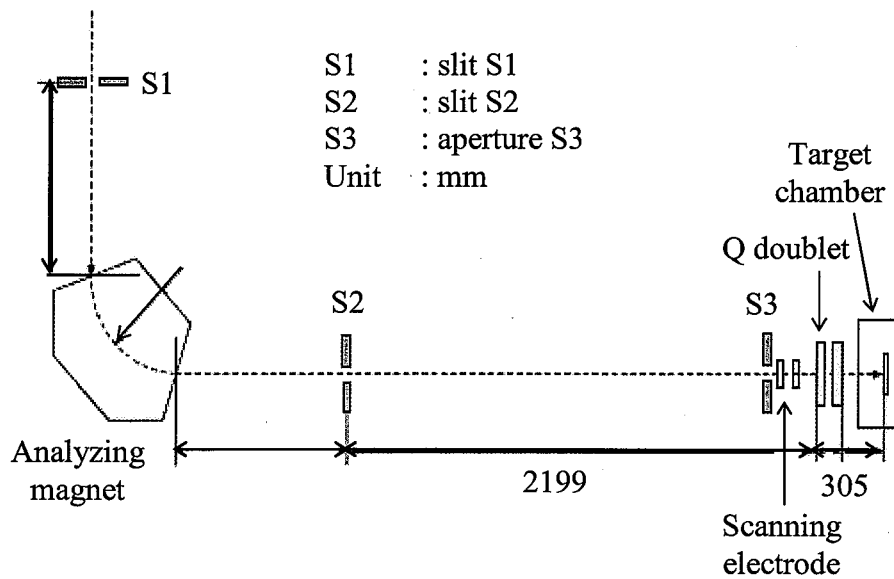
Fig. 2.4.1 Major components of the proton micro-beam line. The image at slit S1 is focused on slit S2. The image of slit S2 is focused on sample. Aperture S3 limits the angular divergence of the beam.

2.4.2 Two-dimension scan of proton micro-beam

The scanning measurement of the proton micro-beam is used for measuring the proton-beam size and the uniformity of plastic scintillator.

The schematic diagram for the proton-beam scanning measurement is shown in Fig. 2.4.2. Scanning voltages generated by a function generator [27] are amplified and supplied to the electrodes placed upstream of the Q doublet. Voltages are measured and recorded together with the signals of a detector. Beam positions on the sample are identified by scanning voltages. The magnetic field of the Q doublet is adjusted so that the spot size is minimized on the plastic scintillator.
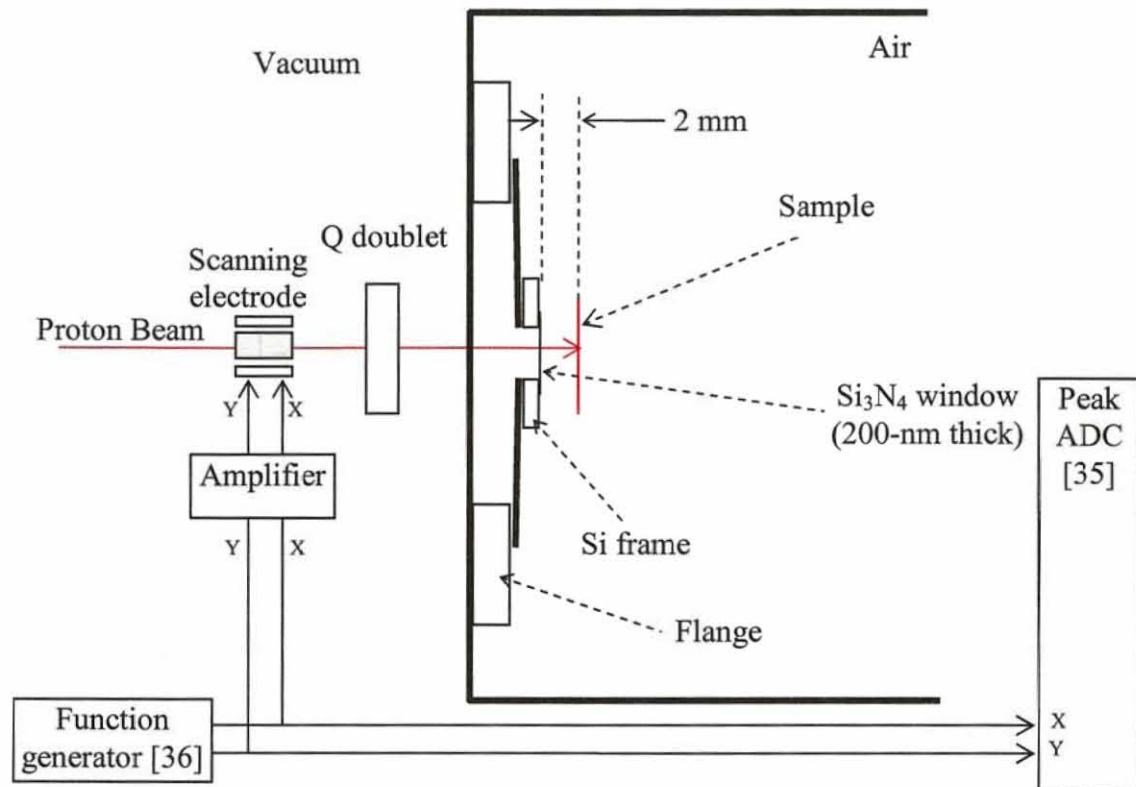
Fig. 2.4.2 The application to the beam scanning measurement on the sample.

2.4.3 Energy spread of protons

The energy spread for protons is measured by using a high-resolution PIPS (Passivated Implanted Planar Silicon) detector, typed PD25-11-300AM manufactured by Canberra [28]. The PIPS detector is mounted behind the S_3N_4 window at a distance of 5-mm air. Fig. 2.4.3 shows a 2.8-MeV proton micro-beam is measured by the PIPS detector. Two peaks correspond to protons penetrating and NOT penetrating the copper mesh, respectively. The energy spread of protons is obtained from the fitting of the high energy peak to the Gaussian function. It is less than 1% (FWHM). The obtained result for the energy spread of 3.4-MeV proton micro-beam is shown less than 1 % in FWHM.
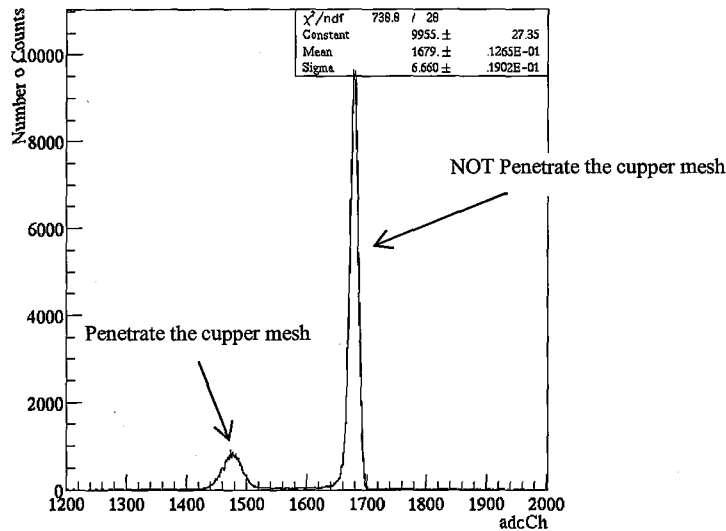
Fig. 2.4.3 A 2.8 MeV proton-micro beam is measured by the high resolution PIPS detector. The low and high peaks correspond to protons penetrating and NOT penetrating, respectively. The energy spread of protons is obtained from the fitting of the high energy peak to Gaussian function. It is confirmed to be less than 1 % in FWHM.

2.4.4 Size of proton micro-beam

Fig. 2.4.4 shows the schematic diagram for the proton beam size measurement. We use the copper mesh [28] and the PIPS detector [29], which are installed at distances of 2 mm air and 5 mm air, respectively, from the Si_3N_4 window. The copper mesh, typed Fine Bar Grids square mesh G400HS, has 400 lines/inch. The interval is 62 μm. The hole width is 54 μm. The bar width is 8 μm. Scanning voltages from the function generator are recorded together with the signal output of the PIPS detector.
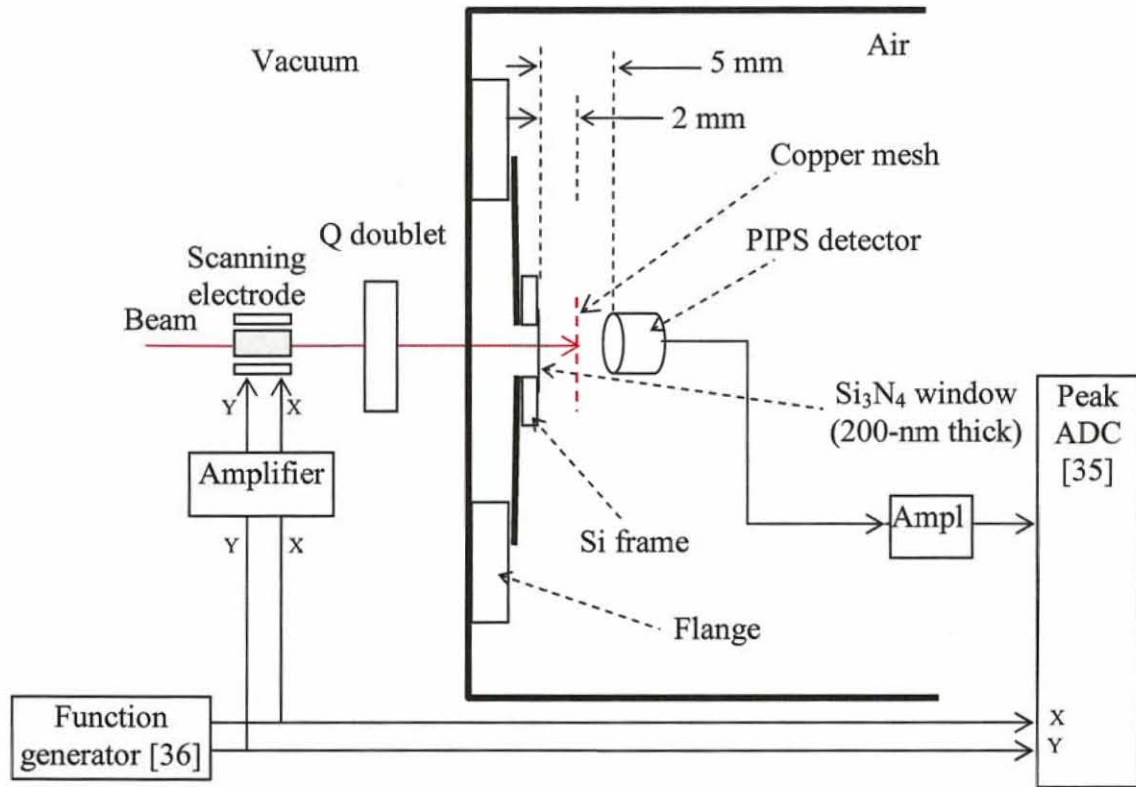
Fig. 2.4.4 Schema of proton beam size measurement.

The data plotted in Fig. 2.4.5 is the scanning voltage channel (unit in ADC channel of the analog-digital converter [30]) when the events, which correspond to the protons penetrated the copper mesh, are selected. Fig. 2.4.5a shows results of the scanned area of 200 μm (horizon) × 200 μm (vertical) of the proton micro beam of 2.8 MeV on the copper mesh. Evaluating of the size of proton micro-beam is measured from 1-dimensional scan. Fig. 2.4.5b and Fig. 2.4.5c show 1-dimensional scan in the horizontal (x) and vertical (y) direction. From the fitting to the Gaussian function for a peak in Fig. 2.4.5b (x-scan) and Fig. 2.4.5c (y-scan), the beam size is determined to be 12 μm (FWHM) in horizontal direction and 12 μm (FWHM) in vertical direction. The size of the proton micro-beam with energy of 3.4 MeV also gets similar results.
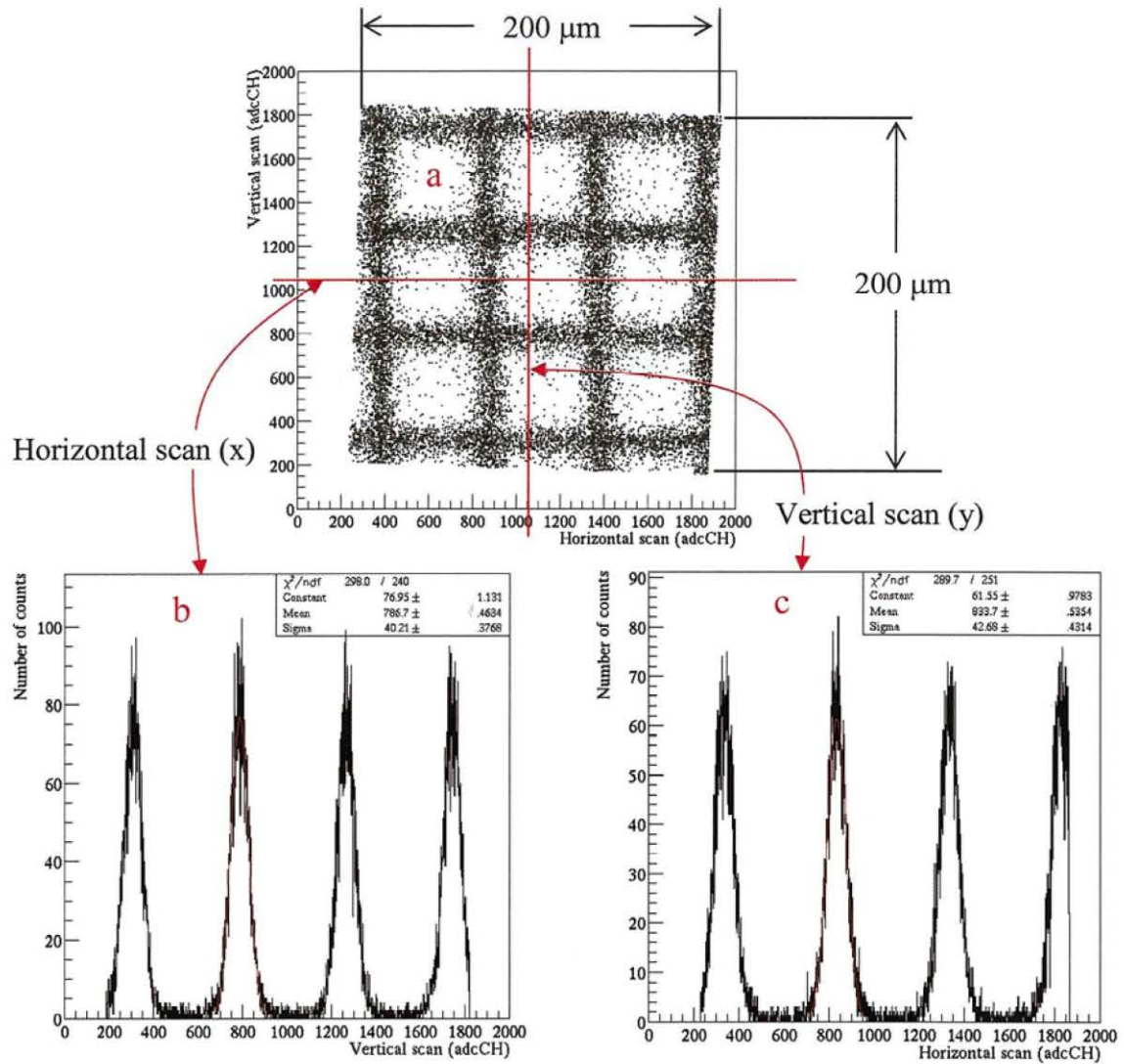
Fig 2.4.5 To evaluate the size of proton micro beam, a scanning on the cupper mesh is carried out. From the fitting to Gaussian function for a peak, the beam size is determined to be 12 μm and 12 μm in FWHM for 2.8-MeV protons in horizontal vertical direction, respectively.

      a. The two dimensional scanned area of 200 (x) × 200 μm(y)

      b. Horizontal scan data (x)

      c. Vertical scan data (y)

2.4.5 Arrangement for proton experiment

For proton measurements, we use the same plastic scintillation detector that is employed for the electron experiment. The scintillation detector is installed inside the target chamber, which is used as the dark box under atmospheric conditions. The experimental arrangement is shown in Fig. 2.4.6. A proton micro-beam is extracted into air through a 200-nm thick Si_3N_4 window and 2 mm of air before irradiating at the center of the plastic scintillator.

Measurements are performed for proton energies of 2.8 and 3.4 MeV with the count rate on order of hundreds counts/sec operated at low intensity. The count rate of the background is negligible compared to that of the protons.

For scanning measurements on the plastic scintillator, scanning voltages (X,Y) of the function generator [27] are measured and recorded together with the signal of PMT outputs. Beam positions on the plastic scintillator are identified by scanning voltages. Scanning measurements are carried out for the two-dimension area of around (1 mm × 1 mm) and the one-dimension line of 1 mm. Measurements are performed at the center of the plastic. It is shown in Fig. 2.4.7.
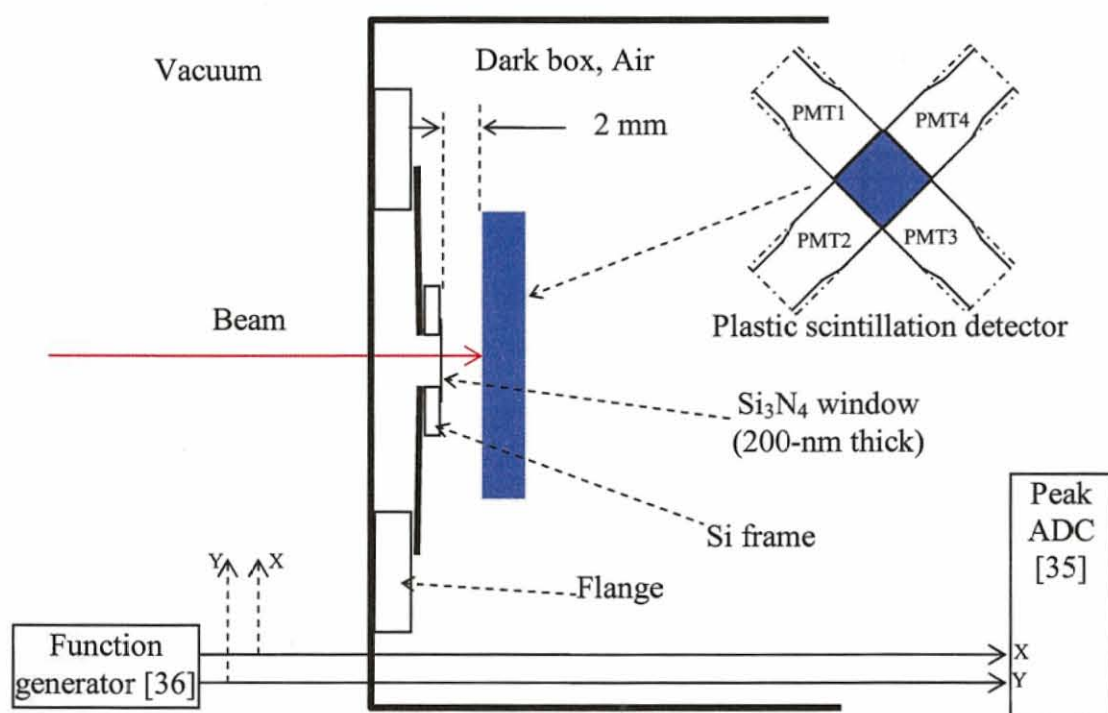
Fig. 2.4.6 Schematic drawing for proton measurements. The scintillation detector is installed inside the dark box under atmospheric conditions. A proton micro-beam is extracted into the air through a 200-nm thick Si_3N_4 window and 2-mm air before irradiating at the center of the plastic scintillator.
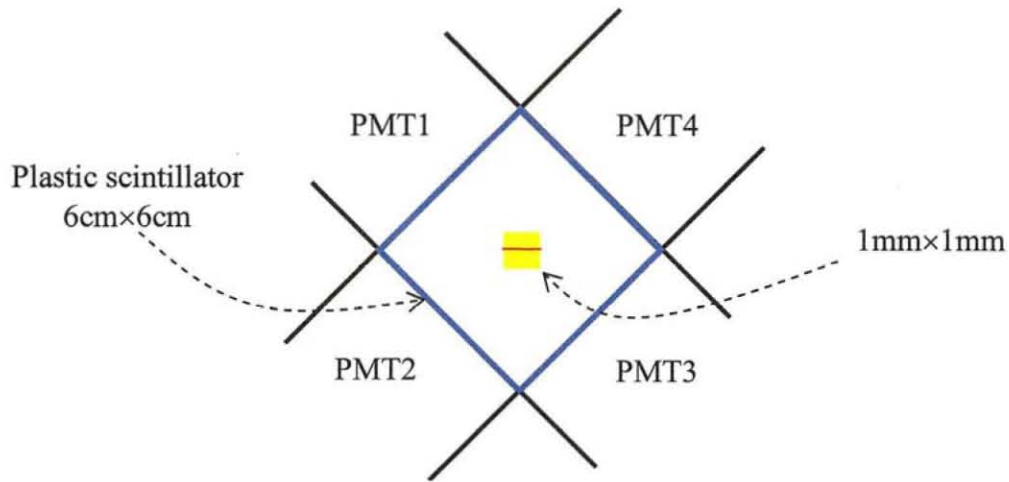
Fig. 2.4.7 Scanning measurements on the plastic scintillator for two-dimension area scan of about (1mm×1mm) (yellow) and one-dimension line scan (red). The plastic scintillator size is (6cm×6cm×1cm).

2.4.6 Count rate of proton micro-beam

In the case of the proton measurements, the beam intensity is controlled so that the count rate is within 1000 counts/sec. Fig. 2.4.8 shows the count rate (counts/sec) of a 2.8 MeV protons plotted versus the measurement time (sec). Measurements in other proton energies also have the similar count rate profile as that of 2.8 MeV.

The gain-shift of PMTs would happen if the count rate changes. Here, the PMTs used in this work have no the rate-dependent gain shift up to 1000 counts/sec. They are measured and shown in section 2.1.2.3.
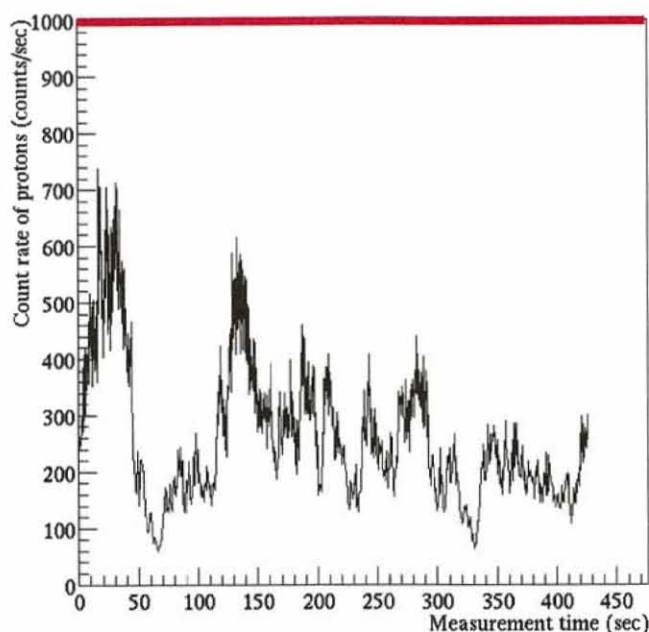
Fig. 2.4.8 The count rate dependence on measurement time (sec) of the proton micro-beam line of 2.8-MeV. It is controlled so as to be within 1000 counts/sec. The PMTs have no the rate-dependent gain shift up to 1000 counts/sec.

2.4.7 Spectrum for mono-energetic protons

Energy spectrum of proton micro-beam is plotted as the summed number of photoelectron in 4 PMTs. The number of photoelectrons is evaluated from the single photoelectron measurement. Fig. 2.4.9 shows the proton spectrum of 2.8-MeV. The count rate of background is small in comparison with that of protons. The spectrum of 3.4-MeV protons is similar to that of the 2.8-MeV protons. Fitting the proton spectrum to Gaussian function, the peak position and the energy resolution (FWHM) are obtained. Notes, the fitted region of the spectrum is chosen from position of 2.35σ (FWHM) at left side (from the peak) to position of 3σ at right side compared to peak position of the fitted spectrum, so as to avoid the tail of spectrum. Here, σ is the standard deviation of the spectrum.
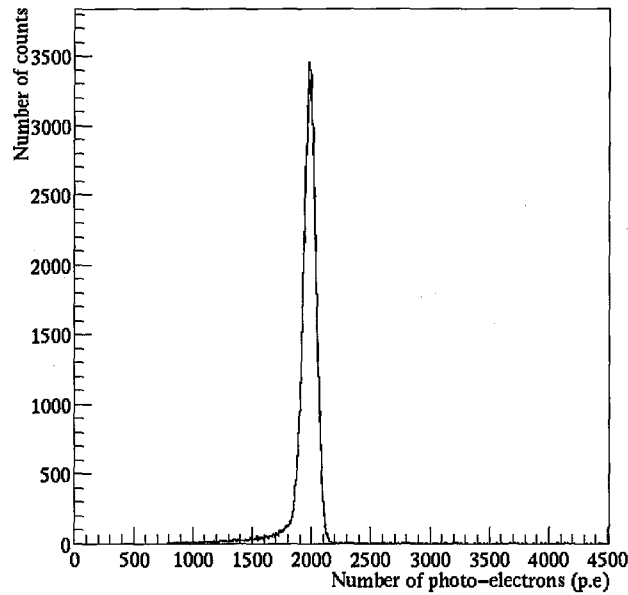
Fig. 2.4.9 Spectrum of 2.8-MeV protons, plotted in the photoelectron scale.

2.5 Data taking system

Data taking system is built for electron and proton and LED measurements. Most experiments are carried out outside Osaka e.g. CENBG Lab, France and Fukui, Japan. It is necessary to make the data taking system compact.

Fig. 2.5.1 shows the schematic diagram of the electronics for data taking system. There are 3 types of trigger signals for (1) the plastic scintillation detector (PL trigger), (2) LED (LED trigger) and (3) the pedestal of detector (PED trigger). PL trigger is from the hit at the plastic scintillator for measuring photoelectrons. Trigger signal from LED driver is for measuring the LED signal. Trigger from 1-Hz clock signal is for measuring pedestal. The green, red, brown lines in Fig. 2.5.1 represent the PL, LED, PED triggers, respectively. The blue line represents for scanning proton micro-beam measurement to record the beam position. It is used only for proton experiments. The trigger logic of the data taking system is described in the broken line. For experiments performed at CENBG Lab, France and at WERC, Japan, the trigger logic is compacted within one logic module. The data taking system runs under Linux computer near the detector system and is controlled over network. It is important to control the system with long distance, especially, for the proton experiment because we can not stay in the experiment area while the accelerator is running.
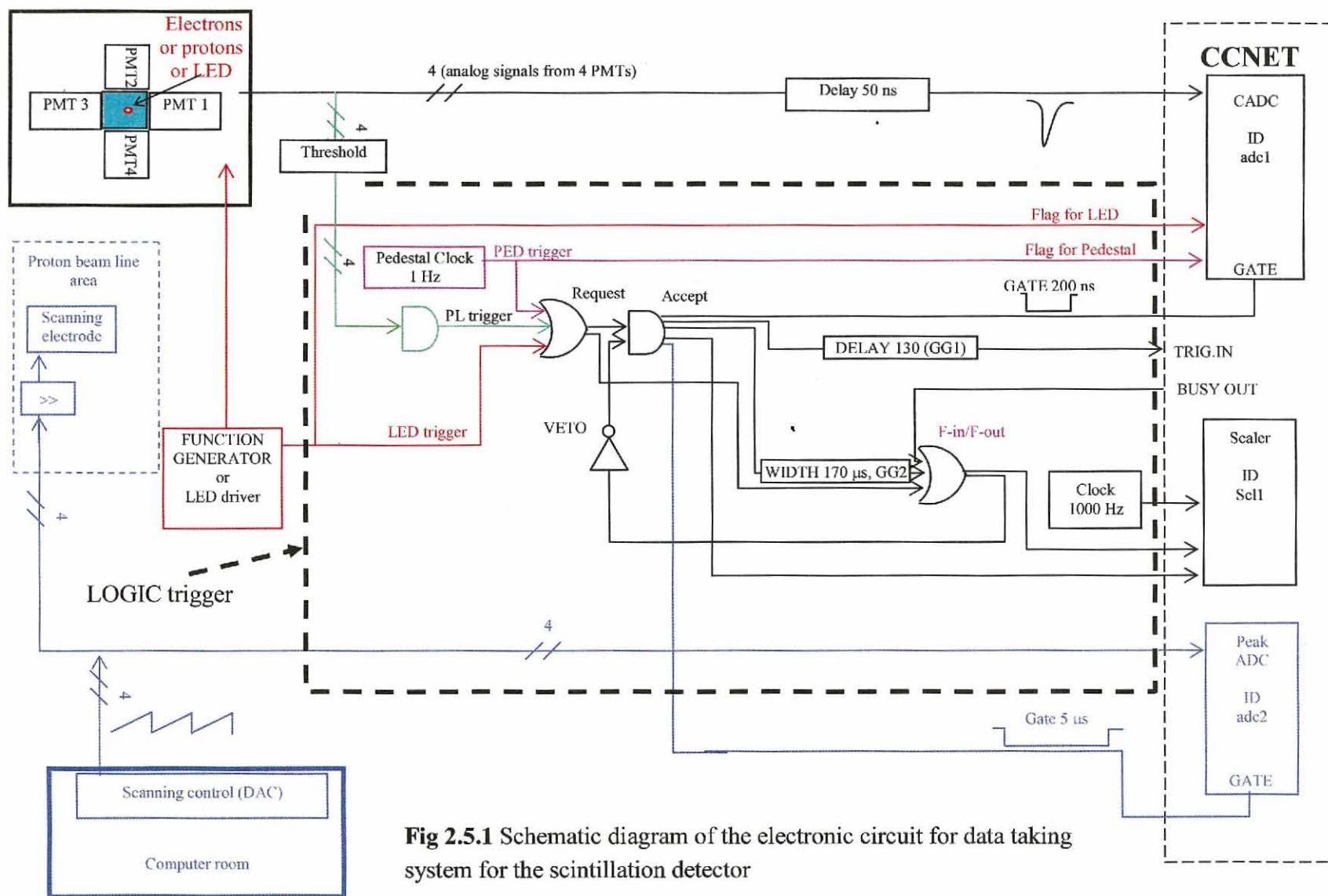
Fig 2.5.1 Schematic diagram of the electronic circuit for data taking system for the scintillation detector

2.5.1 Trigger signal

Three types of the trigger signals are used. They are PL trigger, LED trigger and PED trigger. Table 2.5.1 explains the function of these types of trigger signals.

Table 2.5.1 Three types of the trigger signals

Name	Explanation
- PL trigger	- from the hit at the plastic scintillator for measuring the number of photoelectrons
- LED trigger	- Trigger for LED
- PED trigger	- Trigger for pedestal signals

2.5.1.1 PL trigger

The PL trigger is used for the plastic scintillation detector when incident particle hit the plastic scintillator. The analog signal from the PMT output is divided by the divider module. One is fed to the charge ADC module (1000 pC; 12 bits [26]) with 50 ns delay. The other one makes the PL trigger signal. The PL trigger signal is made by the coincidence of 4 PMTs. Fig. 2.5.2 shows that the PL trigger is made for the scintillation detector. It corresponds to the green lines in Fig. 2.5.1. The discriminator threshold of PMT signals is set so as to reduce the low-energy background rate. It depends on experiment of protons and electrons.
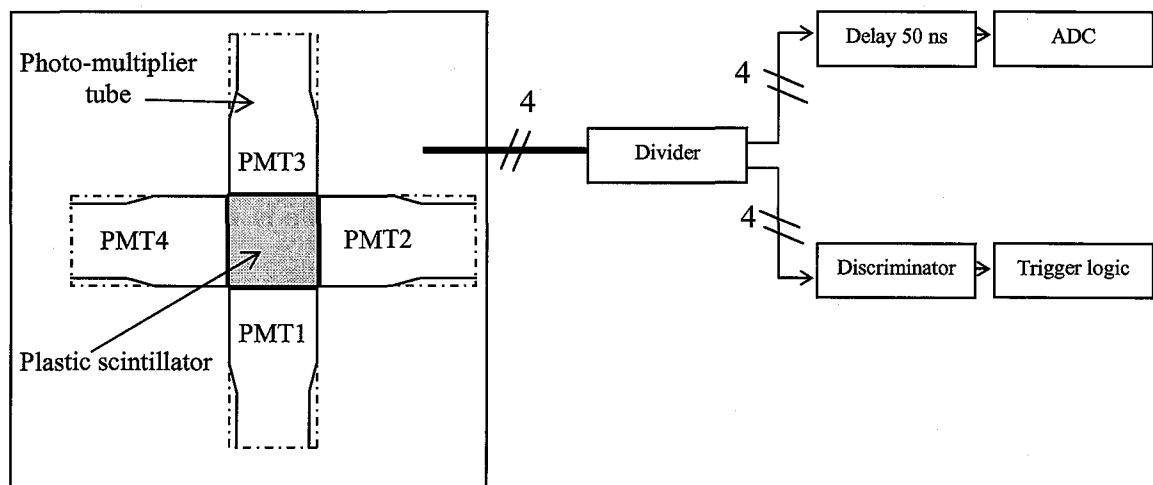
Fig 2.5.2 The principle of the PL trigger signal

2.5.1.2 LED trigger

The LED trigger is used for LED measurements. A pulser (a function Generator, a pulse generator or a LED driver) is employed to drive the LED associated with a trigger. A pulse output from the pulser is fed to the LED for light emission and its trigger signal is made for LED trigger. The red line in Fig. 2.5.1 is for the LED measurement.

2.5.1.3 PED trigger

The PED trigger is used for measuring the pedestal of each PMT. The trigger signal is made by the clock generator with the trigger rate is 1 Hz. The brown line in Fig. 2.5.1 shows the PED trigger for measuring pedestal of each PMT.

2.5.2 FPGA trigger logic

Some experiments in this work need to be carried out outside our Laboratory, namely, at CENBG (Le Centre d'Études Nucléaires de Bordeaux Gradignan, France [18]) for the electron measurements, and at WERC (the Wakasa wan Energy Research Center, Japan [19]) for the proton measurements. We carry the data acquisition system to there from Osaka. Therefore, it is necessary to reduce the electronic modules as much as possible. For that purpose, the trigger logic (broken line in Fig. 2.5.1) is compacted within one FPGA trigger module. FPGA is a programmable logic which is customized for our set-up. The trigger module, which is developed by Osaka University, uses the Altera Cyclone chip EP1C6T144C8 [31] and 250 MHz internal clock generated by internal PLL. Trigger logic on the FPGA is programmable. Quartus II 6.1 web edition [32] (by Altera Corporation) is used to design.

The trigger module [33] is designed with 16-NIM inputs, 8-NIM outputs, 16-LVDS outputs and 8-TTL inputs. In this module, the NIM inputs and NIM outputs are used for trigger logic and the LVDS outputs are used for monitoring. Fig. 2.5.3 shows the trigger module. The logic diagram of the trigger module is shown in Fig. 2.5.4. The I/O assignments of the trigger module are shown as Table 2.5.2. It notes that NIM outputs is adjusted the width and delay. The pulse generator is made for the LED and PED triggers inside the trigger module. The trigger logic is synchronous logic to the 250 MHz clock. Therefore, the output of the logic has 4 ns jitter to the input signal. However, the width of the output pulses has definite width controlled by the internal clock. Section 2.5.4 and section 2.5.5 show the data taking system for electrons and protons experiments, respectively.

Trigger Module V		
NIM_IN	NIM_OUT	LVDS_OUT
00	00	00
01	01	01
02	02	02
03	03	03
04	04	04
05	05	05
06	06	06
07	07	07
08		08
09		09
10		10
11		11
12		12
13		13
14		14
15		15

NIM_OUT(0-7)

NIM_IN(0-15)

LVDS_OUT
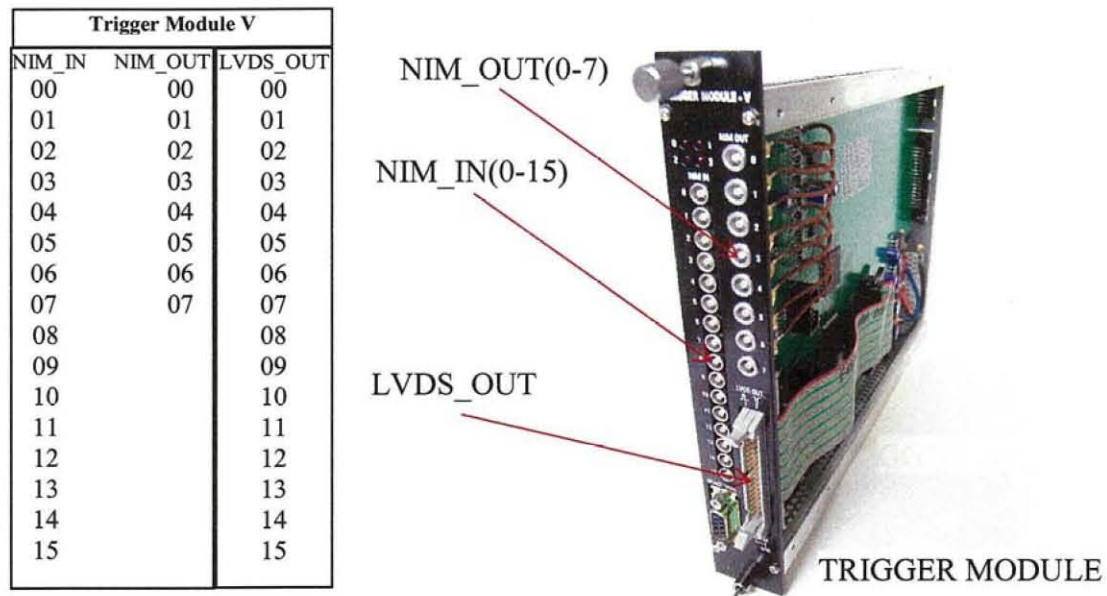
TRIGGER MODULE

Fig 2.5.3 I/O trigger Module V and a picture of the module. There are 16 NIM inputs, 8 NIM outputs and 16 LVDS outputs [42]

Pedestal (1 Hz) Pulse Generator

Flag for PED (Width, delay)

Trig_PED

PL

Request

Request

DELAY 130 μs (GG1)

LED

GG2

F_in/F_out

busyout

Gate ADC (150 ns)

Gate ADC (200 ns)

Trig_LED

Veto

Flag for LED (Width, delay)

Trig for LED driver

LED Pulse Generator

NIM_IN

NIM_OUT

0 1 2 3 4 5 6 7 8 9 10 11 12 13 14 15

0 1 2 3 4 5 6 7
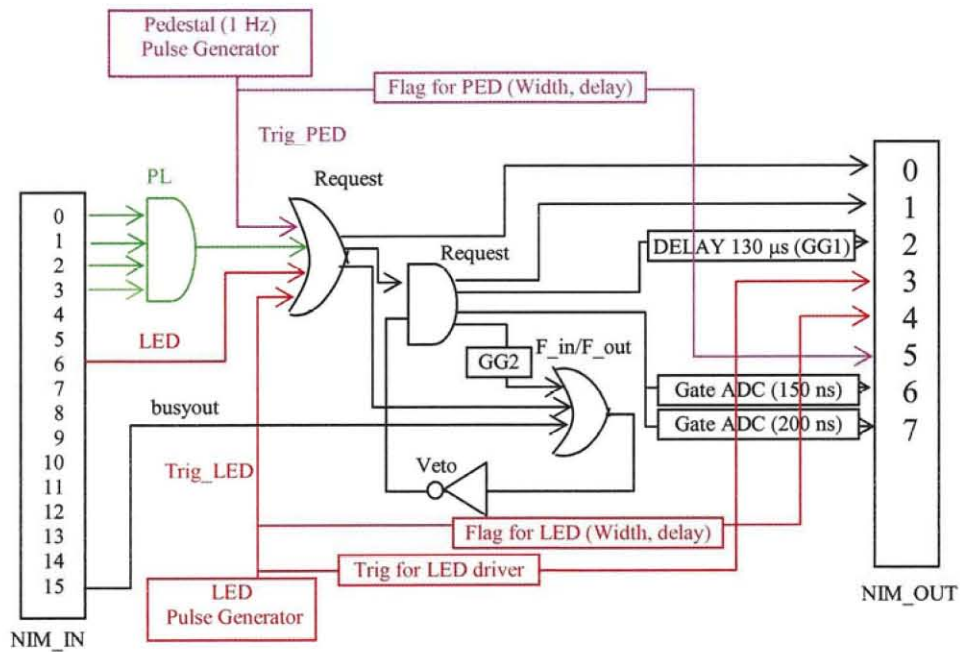
Fig 2.5.4 The logic diagram of the trigger module. Note that, for a specific experiment, NIM inputs can be changed the coincidence AND or OR. NIM outputs can be controlled the width and delay.

Table 2.5.2 Pin assignments of the Trigger Module for the logic

Trigger Module V		
NIM_IN	NIM_OUT	LVDS_OUT (Monitoring)
00 : Input (trig. PMT1) 01 : Input (trig. PMT2) 02 : Input (trig. PMT3) 03 : Input (trig. PMT4) 04 : 05 : 06 : Trig. LED 07 : 08 : 09 : 10 : 11 : 12 : 13 : 14 : 15 :Busyout from CCNET	00 : Request 01 : Accept 02 : GG1 (delay 130 μs) 03 : 04 : Trigger for LED 05 : Trigger for PED 06 : Gate for CADC (150 ns) 07 : Gate for CADC (200ns)	0 : NIM_IN(0); 1 : NIM_IN(1); 2 : NIM_IN(2); 3 : NIM_IN(3); 4 : NIM_IN(4) or NIM_IN(5) or NIM_IN(6) or NIM_IN(7) or NIM_IN(8) or NIM_IN(9); 5 : NIM_IN(10) and NIM_IN(11); 6 : request; 7 : accept; 8 : trig_LED; 9 : trig_PED; 10 : Fin_Fout(0); 11 : NIM_IN(15); -- busyout input 12 : GG1; 13 : GG2; 14 : veto; 15 : time(14); -- for Clock

2.5.3 Test trigger module

The logic inside the trigger module is tested by using a NIM input or a pulse generator (made by the trigger module) to monitor logic outputs such as request, accept, GG1, GG2, etc. Fig. 2.5.5 shows the monitoring of logic signals with the input on order of kHz (request). Note, to be easy to monitor the logic trigger, the "busyout" veto is disabled. GG1 and GG2 are set 130 μs and 170 μs, respectively. The trigger logic "accept" only opens when it satisfies the condition of GG2.
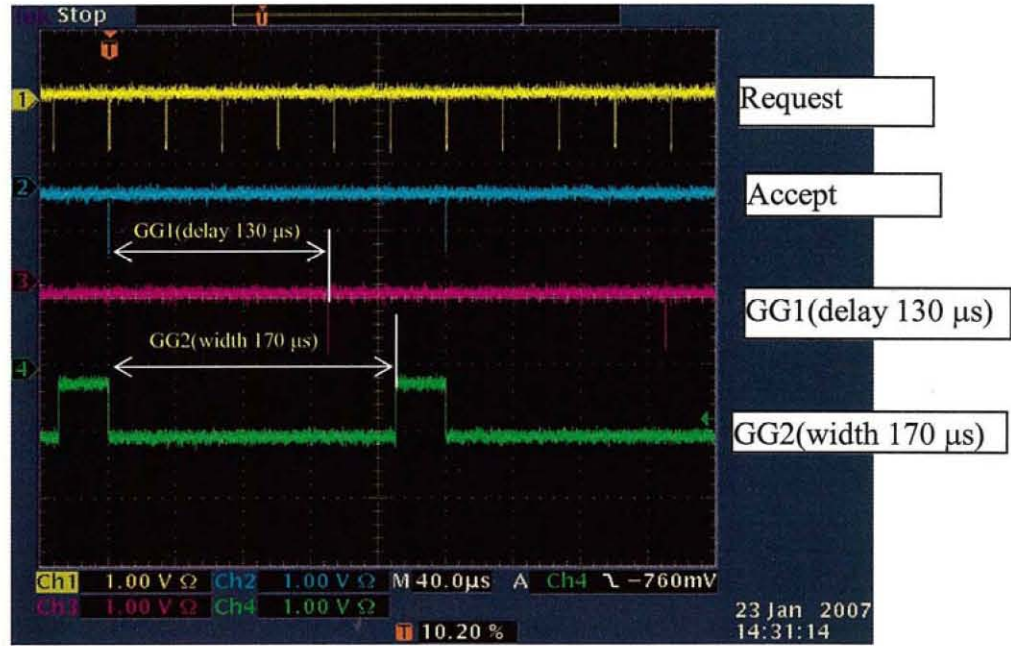
Fig 2.5.5 Test the trigger module through monitoring some logic signals such as request, accept, GG1, GG2, .etc

2.5.4 Data taking system for electron experiment at CENBG, France

The data taking system for the electron experiment at CENBG, France is shown in Fig. 2.5.6. For PL trigger (green line), the analog signal from PMTs is divider by divider module. One is fed to the charge ADC with 50 ns delay by the delay module. The other one come to the discriminator module then to the trigger module. The trigger logic is made inside the trigger module. Two logic outputs (NIM_OUT7 and NIM_OUT2) from the trigger module come to the ADC gate of the ADC module and to Trigger_in of the CAMAC crate controller CC/net (TOYO) [34], respectively. NIM_OUT2 and NIM_OUT7 are fixed with width of 200 ns and of 130 μs, respectively. The LED trigger (red line) used in this work is for monitoring i.e. to monitor gain shift of PMTs as well as the effect of the magnetic field from the electron spectrometer to PMTs. The brown line is for pedestal measurement with the 1-Hz clock, which is made by the trigger module. Table 2.5.3 shows the NIM and CAMAC module for the data taking system which is used for the electron experiment at CENBG, France. The NIM modules are reduced to 6 modules. It is comfortable to carry to France.

Table 2.5.3 NIM and CAMAC modules for the data taking system

	Name	Explanation	Numbers	
NIM	1. Discriminator	6 channels (negative)	1	711 (Phillips)
	2. Trigger module	(16 inputs and 8 outputs) NIM	1	Develop at Lab
	3. Analog delay	2 × 50 ns	2	N-TS 050
	4. LED driver		1	
	5. Divider		1	
Total			**6 modules**	
CAMAC	1. Ccnet controller		1	Toyo
	2. ADC (16 bits)	Charge ADC	1	RPC-022, REPIC
Total			**2 modules**	

Fig 2.5.6 Schematic diagram for the data taking system which is used for the electron experiment at CENBG, France. Green, red and brown lines represent for PL, LED and pedestal trigger, respectively.

Divider Trigger Module Analog delay

Discriminator High Voltage

LED driver Charge ADC CCNET
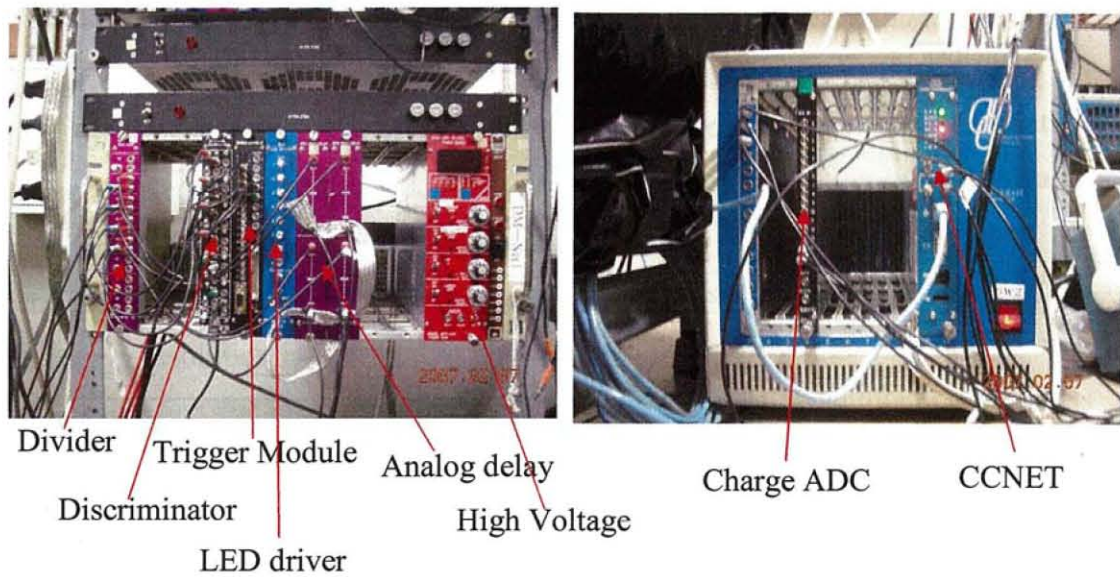
Fig. 2.5.7 Pictures of hardware of the data taking system (NIM+CAMAC). The figure shows NIM and CAMAC modules for the data taking system. The system is tested at Lab (Osaka) before carried to CENBG, France.

2.5.5 Data taking system for proton experiment at WERC, Fukui, Japan

Data taking system for the proton experiment is almost similar to that for electron experiment. Additionally, at proton scanning measurement, the Analog-Digital Converter [30] is employed to measure the scanning voltage in order to determine the position of proton micro beam. The blue line in Fig. 2.5.8 is used for proton-micro beam. The CAMAC-scaler module is utilized to count the request and accept events and time measurement by a clock, which is generated by trigger module. The count rate profile of proton beam is measured.
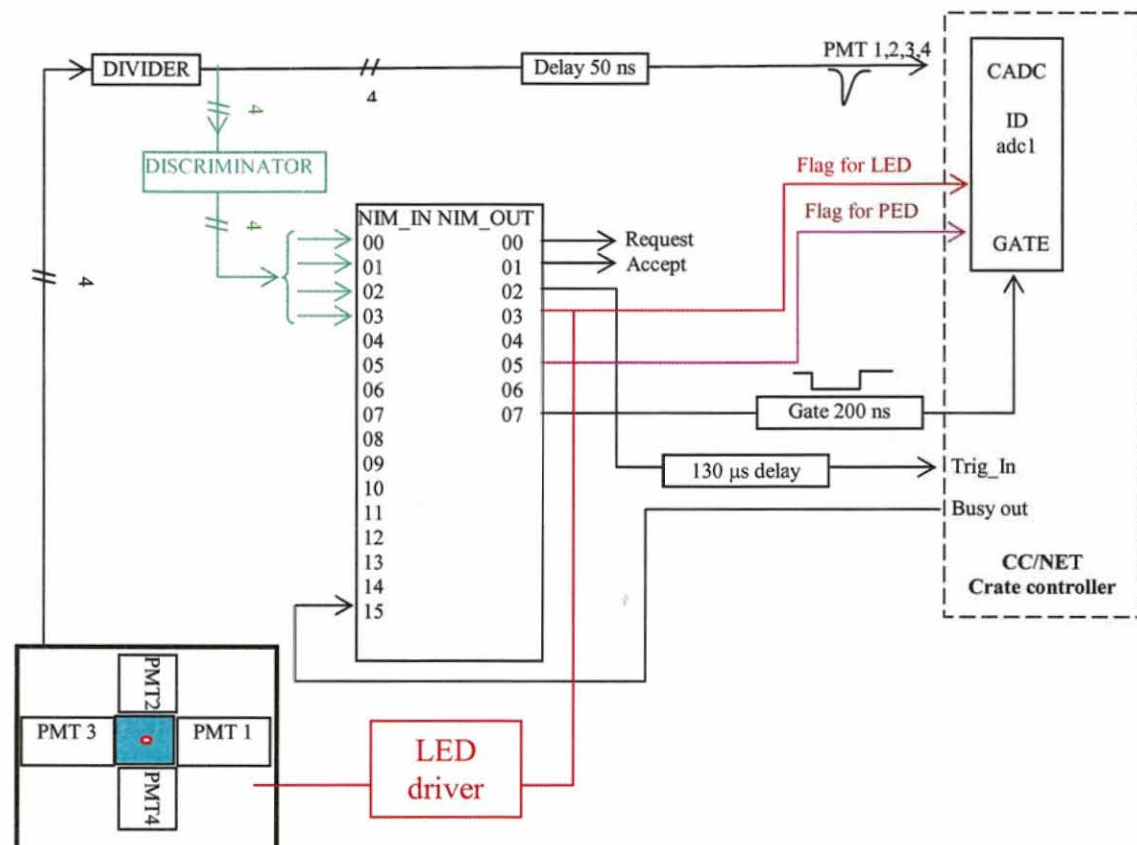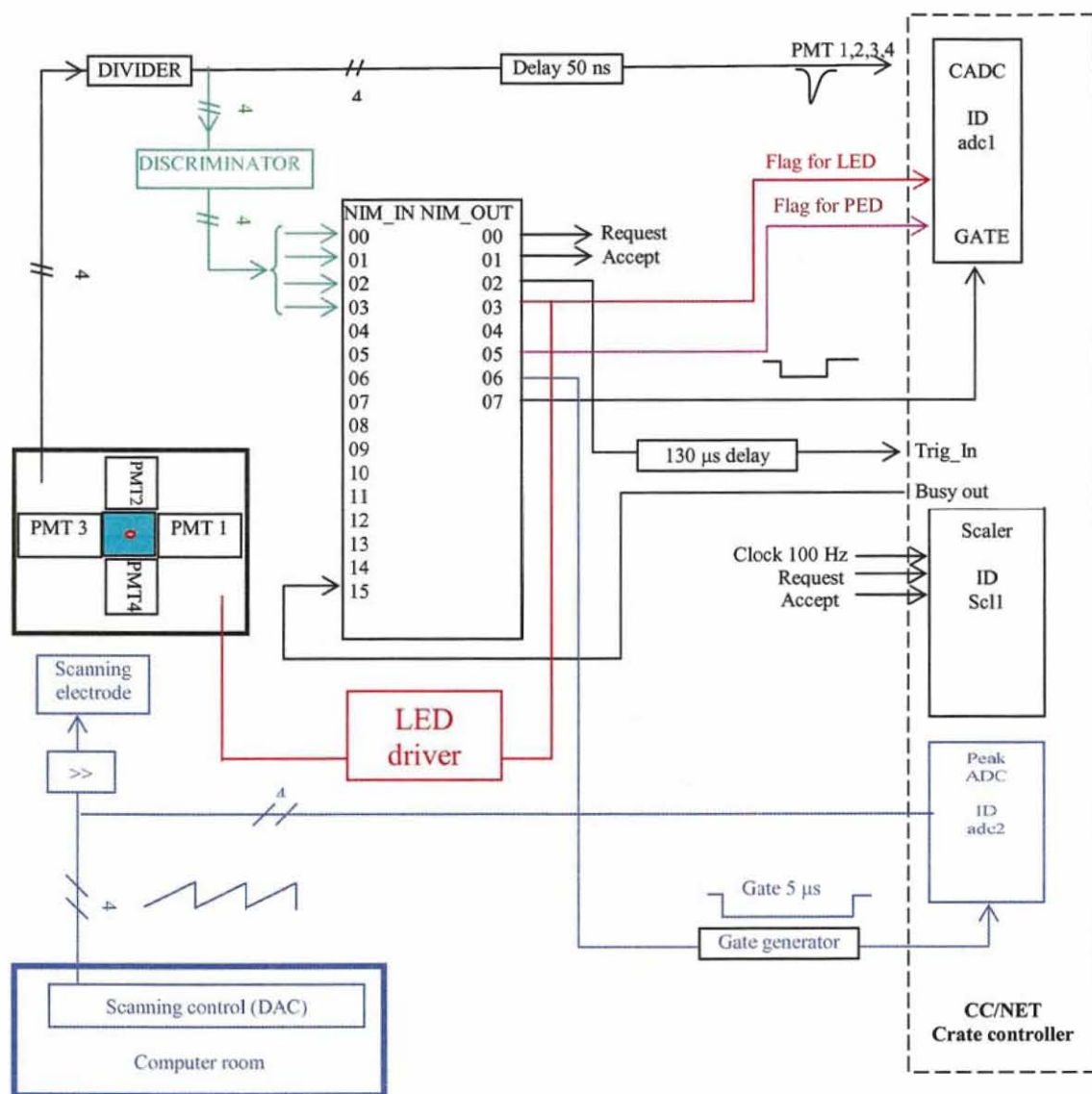
Fig 2.5.8 Schematic diagram for the data taking system which is used for the proton experiment at WERC, Fukui, Japan. Green, red and brown lines represent for PL, LED and pedestal trigger, respectively. Blue line is used for determine the beam position on the sample.

3. ANALYSIS

This chapter will discuss the energy resolution of the plastic scintillation detector for electrons and protons. Analysis of the energy resolution in the separated components is briefly discussed in this chapter. The total energy resolution for electrons and protons is described in section 3.2. From section 3.3 to section 3.4, the total energy resolution is analyzed in the separated components. The scanning proton micro-beam used for measuring the uniformity of the plastic scintillator material is described in section 3.5. The result obtained is used to determine the effect of non-uniformity of the plastic scintillator materials on the excess component. The energy resolution for different scintillator configuration (different thickness of plastic and different photo collection efficiency) is shown in section 3.6 and section 3.7, respectively.

3.1 The 0.975-MeV conversion electron spectrum

3.1.1 The 0.975-MeV conversion electron spectrum

The 975-keV internal conversion electron emitted from ^{207}Bi (Bismuth) radioactive source is employed to estimate the photo collection efficiency and energy calibration of the plastic scintillation detector. The decay scheme of the ^{207}Bi radio isotope is shown in Fig. 3.1.1. The gamma decay mode of 1063 keV is used for 975-keV internal conversion electron. Fig. 3.1.2 shows spectra of (β+γ) and gamma (γ). The 975-keV conversion electron spectrum is obtained from γ spectrum subtracted from (β+γ) spectrum, shown in Fig. 3.1.3.
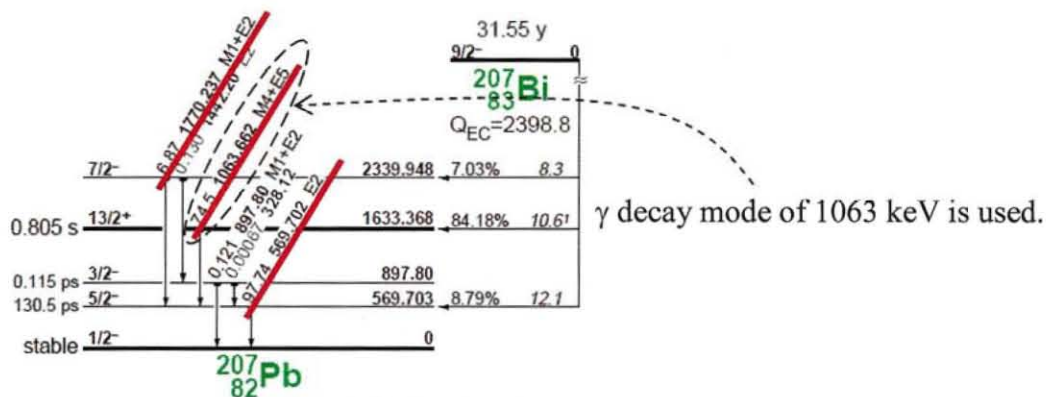
Fig. 3.1.1 Energy levels of ^{207}Bi [35]. The 975 keV (K-shell), 1047 keV (L-shell) and 1060 keV (M-shell) conversion electron are used to evaluate the photo collection and the energy resolution.
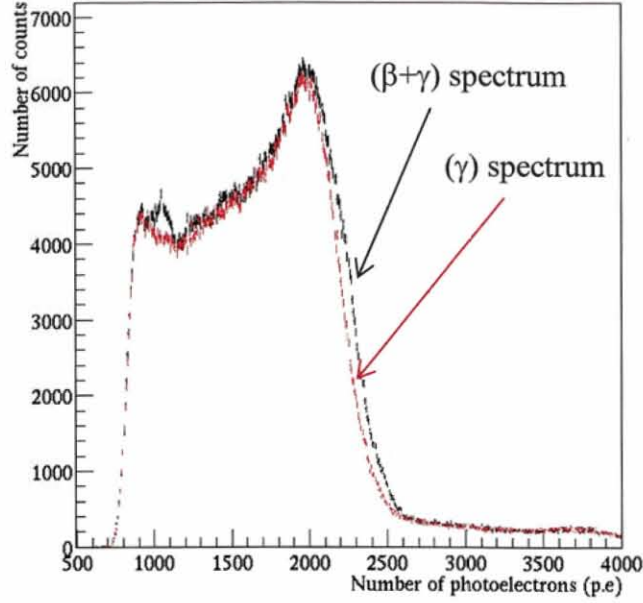
Fig. 3.1.2 The spectra are plotted in the photoelectron scale for a measurement of the 975-keV conversion electron from the ^{207}Bi source. Black line is for (β+γ) spectrum, and red line is for γ spectrum.

3.1.2 Fitting for conversion electron peak

The peak of the spectrum in Fig. 3.1.3 consist of three conversion electron peaks from the K-shell (975 keV), L-shell (1047 keV) and M-shell (1060 keV). The peak is fitted using the triple Gaussian distribution. The Gaussian distribution of each conversion-electron peak can be described as:

$$G_i(x) = \frac{N_i}{\sqrt{2\pi}\sigma_i}.\exp(-\frac{1}{2}\frac{(x\gamma - E_i)^2}{\sigma_i^2}) \tag{3.1.1}$$

Where i = 1; 2; 3 refers to the conversion-electron peak for K-shell (975 keV), L-shell (1047 keV) and M-shell (1060 keV), respectively.

N_i, E_i and σ_i are the area, mean and standard deviation of Gaussian distribution, respectively. γ is gain factor (MeV/ADC channel)

The triple Gaussian function is written as:

$$F(x) = \sum_i^3 G_i(x) \tag{3.1.2}$$

In order to make fitting for the conversion electrons from the ^{207}Bi checking source, we consider two assumptions as follows:

- Relative intensity for each electron-conversion peak, is defined as the area of its corresponding Gaussian distribution. It is written as

- 66 -

$$N_i = N_0 a_i \tag{3.1.3}$$

where, N_0 is Normalization factor; a_i is the branching to the conversion electron.

• Energy resolution of the ith conversion electron peak, R_i, is inversely proportional to the square root of its energy E_i. The standard deviation σ_i can be written as

$$\sigma_i = \sigma_0 \sqrt{\frac{E_0}{E_i}} \tag{3.1.4}$$

Where, E_i is the ith conversion-electron energy. E_0 is 0.975 MeV. σ_0 is standard deviation for 0.975-MeV electron.

Finally, with conditions above, the triple-Gaussian function is obtained as follows:

$$F(x) = \sum_1^3 G_i(x) = N_0 \sum_i^3 \frac{a_i \sqrt{E_i}}{\sigma_0} \exp[-\frac{1}{2}(\frac{x\gamma - E_i}{\sigma_0})^2] \tag{3.1.5}$$

N_0 is normalization parameter.

γ is the gain factor (MeV/ADC channel).

σ_0 is standard deviation for 0.975 MeV (K-shell).

Table 3.1.1 shows the relative conversion-electron intensity for the K, L and M shells versus the conversion electron energies. The peak in Fig. 3.1.3 is fitted with equation (3.1.5). The blue lines correspond to conversion electrons of K, L and M shells.

The photoelectron response and the energy resolution are obtained from these parameters. The energy resolution is calculated as (8.1 ± 0.3) % in FWHM at the 975 keV region.

Table 3.1.1 The relative conversion-electron intensity for K, L and M shells versus the electron-conversion energies [35]. Conversion-electron intensity for K-shell is normalized to 100.

i	Conversion Electron energy E_i (keV)	Relative conversion-electron intensity
1 (K)	975	100
2 (L)	1047	19.8
3 (M)	1060	7.9
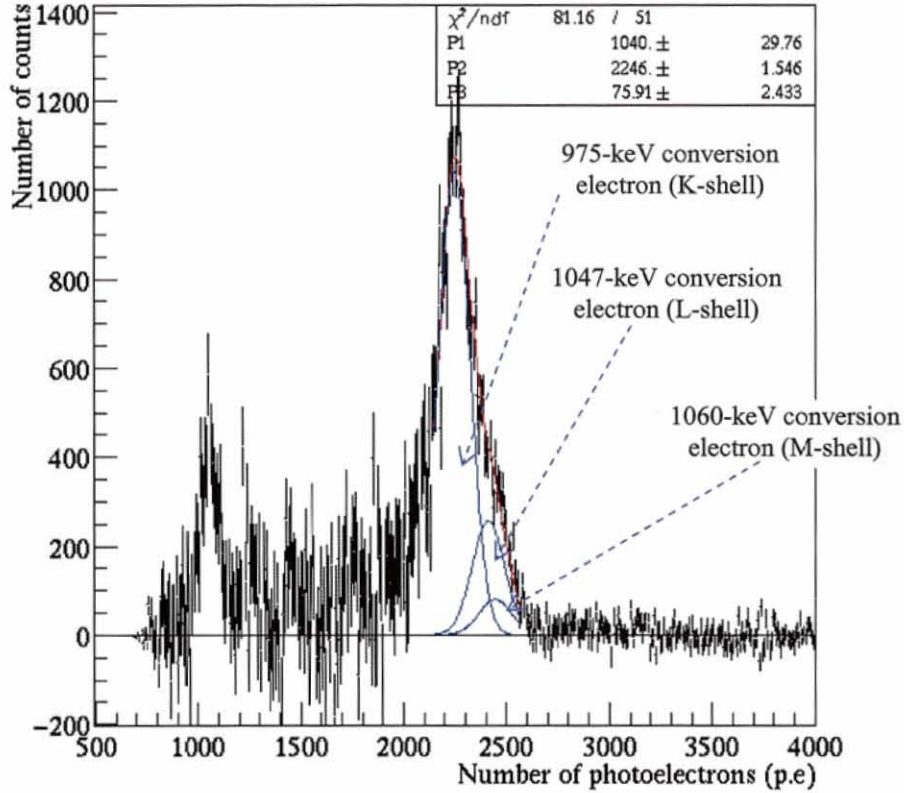
Fig. 3.1.3 Spectrum of the conversion electrons for the 975 keV (K-shell), 1047 keV (L-shell) and 1060 keV (M-shell) versus the number of photoelectrons. The peak is fitted by using the triple Gaussian function to identify the three conversion electrons from ^{207}Bi checking source.

3.2 Total energy resolution for electrons and protons

In this section, we discuss the light-yield response and the total energy resolution for electron and protons. Here, the light yield response is described in photoelectron scale.

3.2.1 Mono-energetic energies of electrons and protons

The electron-beam energies are in the range of energies from 0.7 MeV to 1.7 MeV, namely, 0.7; 1.0; 1.3; 1.5; 1.7 MeV. The proton micro-beams with energies of 2.8 MeV and 3.4 MeV are employed. The energy spread for electron beams and proton beams is measured by the Si(Li) and PIPS detectors, respectively. It is confirmed within 1 % in FWHM, as described in section 2.2.3 for electrons and section 2.4.3 for protons. The 0.975 MeV conversion electron from the ^{207}Bi isotope source is used for comparison purposes with the electron-beam energies.

3.2.2 Light yield response for electrons and protons

For the first step in evaluating the photon response of PMTs in terms of photoelectrons for particle radiation, we use a blue-light LED of 470 nm in wavelength (NSPB500s, manufactured by NICHIA [25]) to measure the single photoelectron spectrum for each PMT, as described in section 2.1.2.4. It is assumed that photoelectrons are directly proportional to the ADC channels measured at the PMTs.
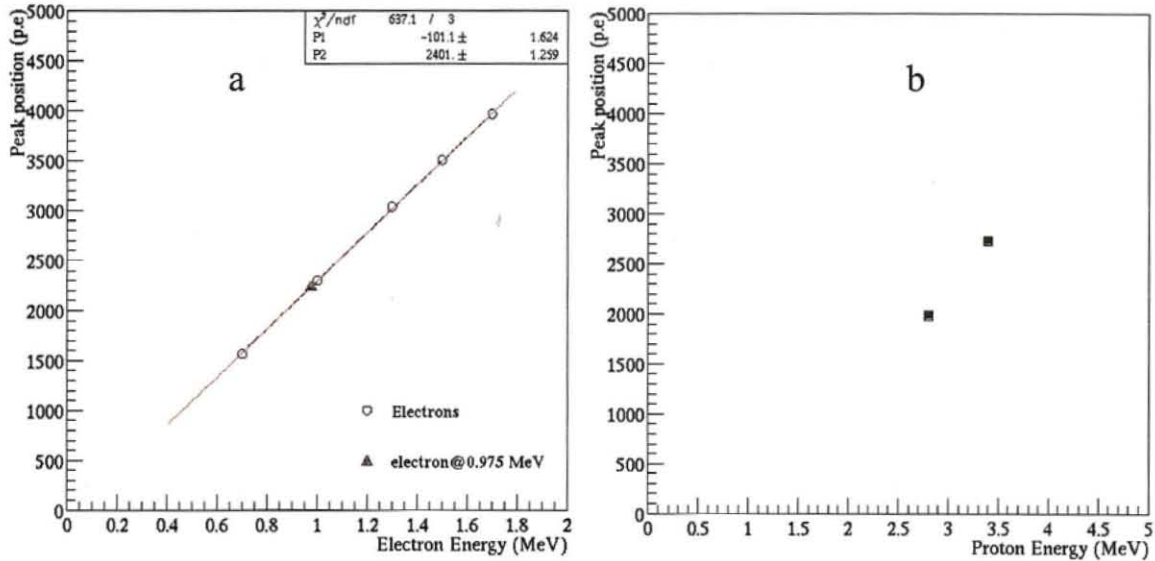
Fig. 3.2.1 Peak position (photoelectrons) is plotted against the energy (MeV) for electrons and protons.

a. Linearity of peak positions of electrons versus electron energies. The 0.975-MeV conversion-electron energy from the [207]Bi source is used for the comparison purpose to electron-beam data.

b. Peak position of protons is plotted against the proton-energy scale.

Fig. 3.2.1a shows the peak positions (unit: photoelectrons) of the electron (open circle) spectra and the 0.975-MeV conversion electron (triangle) plotted against electron energies (MeV). Fig. 3.2.1b shows the peak position of protons versus the proton energy. Here, each peak position, which is corresponds to its energy, is derived from the mean of the Gaussian fitting of the summed number of photoelectrons in 4 PMTs. The fitting line in Fig. 3.2.1a is done for electron-beam data. The light yield of the 0.975-MeV conversion-electron measurement shows good agreement with that of the electron beam from spectrometer. The experimental result in Fig. 3.2.1a shows that the deviation of the electron-beam output of the spectrometer is within 1% in

comparison with the linearity fitting line. The errors are considered smaller than the drawing points. The quenching factor for proton energies of 2.8 MeV and of 3.4 MeV compared to electrons is measured as 31% and 35%, respectively. It shows the quenching factor of protons has energy dependence. Here, the quenching factor is defined as the ratio of the signal amplitudes induced by an ion and an electron of the same energy.

3.2.3 Total energy resolution for electrons and protons

The total energy resolution is obtained from the summed number of photoelectrons in 4 PMTs. Fig. 3.2.2 shows experimental results of the total energy resolution in FWHM plotted in electron energy scale for both electrons and protons. The proton data is plotted on the equivalent electron energy scale. In other words, the data points of electrons and protons are plotted in the photoelectron scale. Open circle and closed square points refer to the total energy resolution for electrons and protons, respectively. The triangle point is for the 0.975-MeV conversion electron. We can see that the total resolution for the 0.975-MeV conversion electron shows good agreement with the electron-beam data.

The obtained results show that the total energy resolution for electrons and protons is different. Total energy resolution is found small for protons and large for electrons. It can be explained the total energy resolution consisted of not only the statistical fluctuation, which should be common to electron and protons, but also from an "excess" fluctuation.
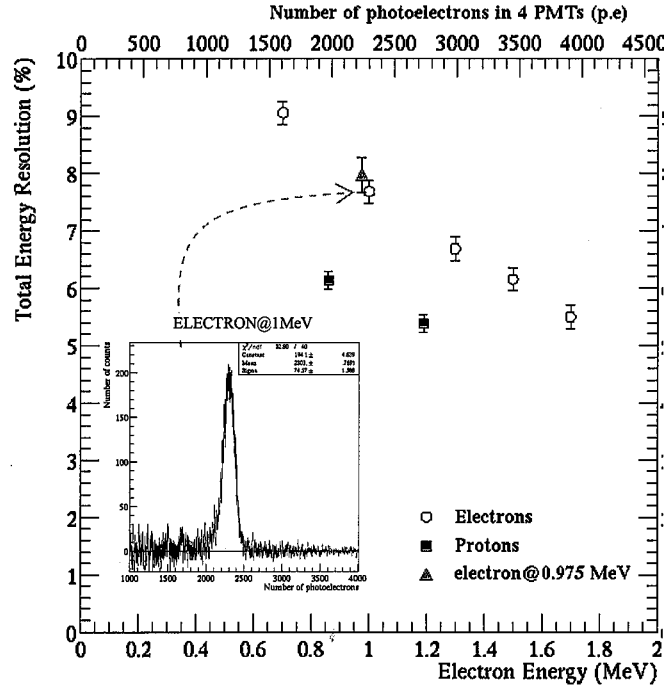
Fig. 3.2.2 Total energy resolution (in FWHM) for electrons and protons are plotted on the electron-energy scale. It is calculated from the summed number of photoelectrons in 4 PMTs. The upper horizontal scale is the corresponding number of photoelectrons.

3.3 Energy resolution in separated components

In this section, we discuss the total energy resolution in separated components.

The total energy resolution of the scintillation detector for incident particle can be described by a chain of subsequent processes. These processes for incident particle with a certain energy can be identified as: (1) energy spread before striking the plastic scintillator, (2) energy loss inside the plastic scintillator and UV light generation, (3) UV light absorption and the visible light emission by the wave length shifter, (4) the visible light collection at the photocathode, (5) the photoelectron production at the photocathode, (6) electron multiplication by PMT dynodes and (7) electronic analysis (analog-digital converter, etc.).

• Energy spread measurements are carried for electrons and protons to be confirmed small. It is discussed in section 2.2.3 and section 2.4.3 for electron beams and proton beams, respectively. Therefore, process (1) does not affect so much to the energy resolution.

• The electrical noise, corresponding to process (7), is confirmed small by the pedestal measurement and the correlation between the PMT signals in LED measurement. The deviation of pedestal signal is within 1 ADC channel, as described

in section 2.1.2.6. It is much smaller than that of the signal of interest. The correlation PMT signals in the blue-LED measurement show the coherent electrical noise is less than 1%, as described in Appendix D.

The effect of processes can be reduced into two separated components. One is the statistical component. It is described from processes (3) to (6). This component relates to the statistical fluctuation of the number of photoelectrons (process 3 to 5) and the electron multiplier variance of the PMT (6). The other relates to the intrinsic property of the plastic scintillator, corresponding to process (2). This process has different fluctuation from statistical component.

Thus, the total energy resolution, R_{tot}, can be separated into two components. It can be written as

$$R_{tot}^2 = R_{sta}^2 + R_{int}^2 \tag{3.3.1}$$

Where, R_{sta} is the statistical component (Processes 3 – 6).

R_{int} is the intrinsic energy resolution (Process 2).

3.4 Analysis of statistical component and intrinsic energy resolution for electrons and protons

Total energy resolution is analyzed into two components. Here, the statistical component in total energy resolution is analyzed with the use of two different methods. It is studied for electron and proton.

3.4.1 Statistical component

We study the statistical component in two methods.

- One is evaluated by the calculation from the statistical fluctuation of photoelectrons and the variance of the electron multiplier gain in PMTs. It is described as $R_{sta}(\%) = \frac{2.35 \times 100}{N^{1/2}} \times (1 + \varepsilon)^{1/2}$, where, N is the number of photoelectrons; ε is the variance of the single photoelectron signal. ε is obtained as 0.12, as described in section 2.1.2.4.

- Other method is based on the correlation measurement of PMT signal. Theoretical consideration is discussed in Appendix A. In this work, the statistical component is obtained from the uncorrelated component of the number of photoelectrons between PMT_{13} and PMT_{24}. Here, the uncorrelated

component is obtained from the variance of the difference of the number of photoelectrons between PMT_{13} and PMT_{24}.

Fig. 3.4.1 shows the uncorrelated component in FWHM, which is plotted in photoelectron scale. It is studied for (1) electron beams (open circle) extracted from the spectrometer; (2) the 0.975-MeV conversion electrons (triangle) from the [207]Bi source and (3) proton beams (closed square). The upper horizontal scale indicates the corresponding electron energies. The solid curve is evaluated from the first method. The result shows that the uncorrelated component for the electron beams, the collimated electron source and the proton beams shows good agreement with the solid curve. It is important to note that the uncorrelated component between PMT_{13} and PMT_{24} for electron and proton describes the statistical fluctuation of the number of photoelectrons and small contribution of electron multiplication process in the PMTs.
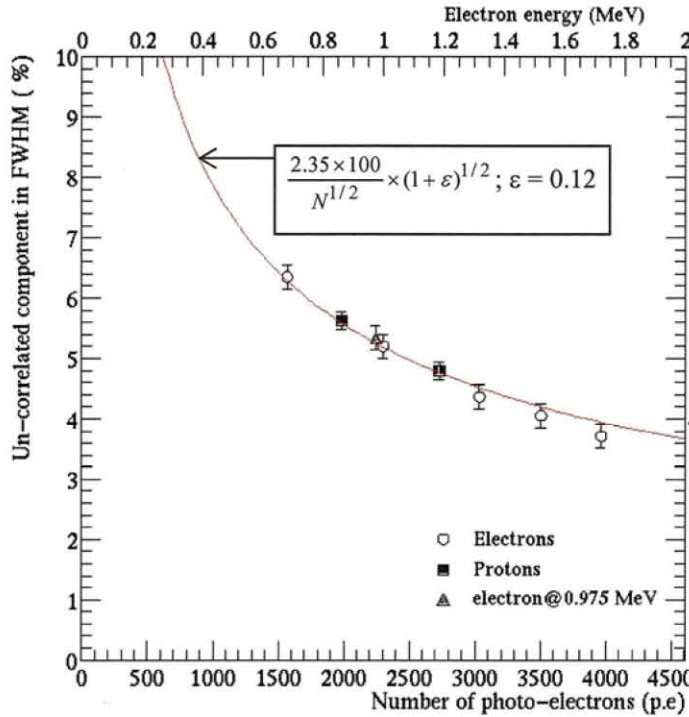
Fig. 3.4.1 Uncorrelated component (in FWHM) for electrons (open circle) and protons (closed square) is plotted against the number of photoelectrons, respectively. The 0.975-MeV conversion electron (triangle point) is for comparison purpose to electron data. It shows good agreement. The solid curve is plotted as $R_{stat} = \frac{2.35 \times 100}{N^{1/2}} \times (1+\varepsilon)^{1/2}$ (in FWHM, %); "N" is the number of photoelectrons. Variance of PMT gain, ε, is 0.12.

3.4.2 Intrinsic energy resolution

The total energy resolution and the statistical component for electrons and protons are already discussed in section 3.3 and section 3.4. The intrinsic energy

resolution (R_{int}) for electrons and protons can be obtained by equation (3.3.1) i.e. it is calculated as $R_{int} = \sqrt{R_{tot}^2 - R_{sta}^2}$. The intrinsic energy resolution for electrons and protons are plotted and compared in the electron energy scale. The obtained results are shown in Fig. 3.4.2 and Table 3.4.1. Here, open circle and closed square points stand for electrons and protons, respectively. The triangle point is for the 0.975-MeV conversion electron.

For electrons, the intrinsic energy resolution is found to have the energy dependence. The 0.975-MeV conversion electron (triangle) shows good agreement with the electron-beam data.

In the case of protons, the intrinsic energy resolution is newly found to be smaller than that for electrons. The result tells us that the intrinsic energy resolution depends on particle types, i.e., electrons and protons. In matter, the stopping process of electron is quite different from that of proton. The difference might be related to different stopping process of both particles in matter.
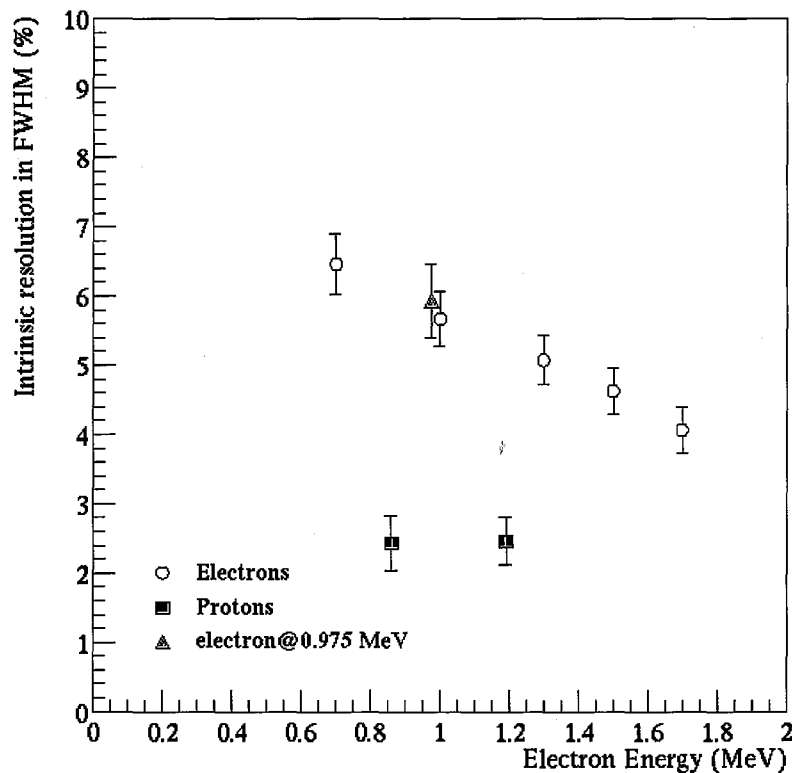

Fig. 3.4.2 The intrinsic energy resolution (FWHM) of plastic scintillator BC-408 for electrons (circle points) and protons (square points) is plotted against the electron-energy scale. Triangle point is for the 0.975-MeV conversion electron from [207]Bi source. It shows good agreement with the electron-beam data. Intrinsic energy resolution for proton shows smaller than that of electron.

Table 3.4.1 Data of the energy resolution in term of separated components for electrons and protons. The proton energies of 2.8 MeV and 3.4 MeV are described in the electron energy scale with the quenching factor 31 % and 35 %, respectively.

Electron energy scale (MeV)	Total resolution (% in FWHM)	Uncorrelated component (% in FWHM)	Intrinsic resolution (% in FWHM)	Source
0.7	9.06 ± 0.2	6.35 ± 0.20	6.46 ± 0.44	Electron beam
0.86	6.13 ± 0.15	5.63 ± 0.15	2.43 ± 0.40	2.8 MeV Proton beam
0.975	7.98 ± 0.30	5.34 ± 0.20	5.92 ± 0.54	From [207]Bi source
1	7.69 ± 0.20	5.19 ± 0.20	5.67 ± 0.39	Electron beam
1.19	5.38 ± 0.15	4.79 ± 0.15	2.46 ± 0.34	3.4 MeV Proton beam
1.3	6.69 ± 0.20	4.36 ± 0.20	5.08 ± 0.35	Electron beam
1.5	6.15 ± 0.20	4.06 ± 0.20	4.62 ± 0.34	Electron beam
1.7	5.50 ± 0.20	3.71 ± 0.20	4.06 ± 0.33	Electron beam

3.5 Uniformity of plastic scintillator materials BC-408

The inhomogeneity of the plastic scintillator material may also cause fluctuation look like the intrinsic resolution. Therefore, the uniformity of the plastic materials is measured. A 2.8-MeV proton micro-beam is employed for the area scan (2D-scan) of about 1 mm × 1 mm and the line scan (1D-scan) on the plastic scintillator BC-408. The set-up of the measurement is described in section 2.4.5.

The spatial cell is defined as a region of 50 μm horizontally (x) × 50 μm vertically (y), where proton events in this region are collected. Enough number of events in each cell for Gaussian fitting is accumulated. The beam size of the protons is measured as 12 μm horizontally (x) and 12 μm vertically (y), as described in section 2.4.4. Fig. 3.5.1 shows peak positions (unit: photoelectron) plotted against the two-dimensional (2D) scanned area (x-y, unit: μm). Each data point is derived from the peak position of the Gaussian fitting for the summed number of photoelectrons in 4 PMTs, corresponding to each cell. The distribution of peak positions is shown in Fig. 3.5.2. Here, each point of the data set is plotted in the deviation of the peak position. The upper horizontal scale indicates the corresponding peak positions. The deviation of peak positions in Fig. 3.5.2 is obtained within 0.2%. Results shows that the plastic scintillator BC-408 employed for this work has a good uniformity of plastic scintillator materials within 0.2%.
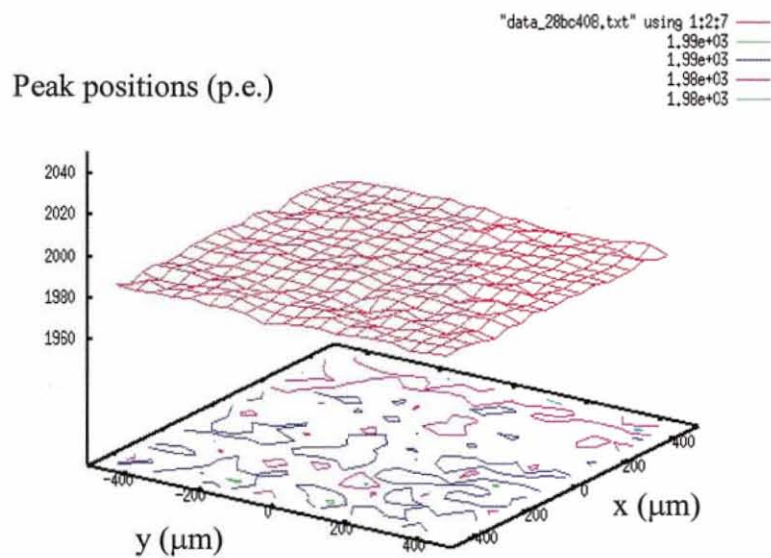
Peak positions (p.e.)

Fig. 3.5.1 Peak positions (unit: photoelectrons) plotted against the two-dimensional (2D) scanned area (x-y, unit: μm).
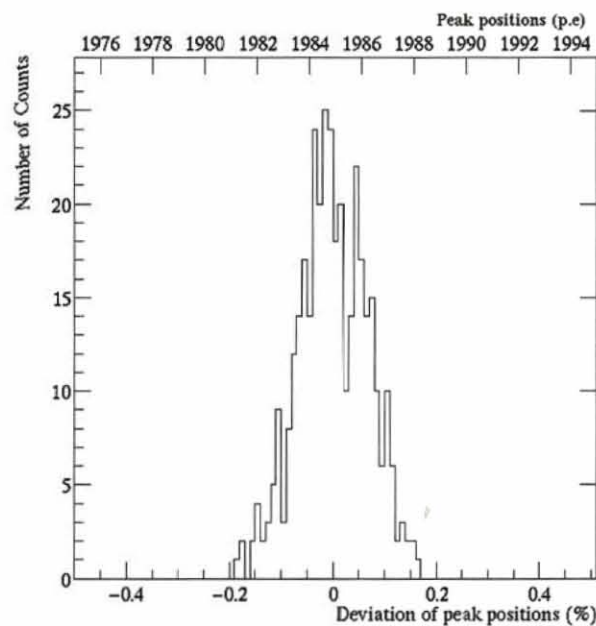

Fig. 3.5.2 Distribution of peak positions of a 2.8-MeV proton micro-beam with 361 cells (19×19) points. The deviation is within 0.2% in FWHM. The upper horizontal scale refers to peak positions (photoelectrons).
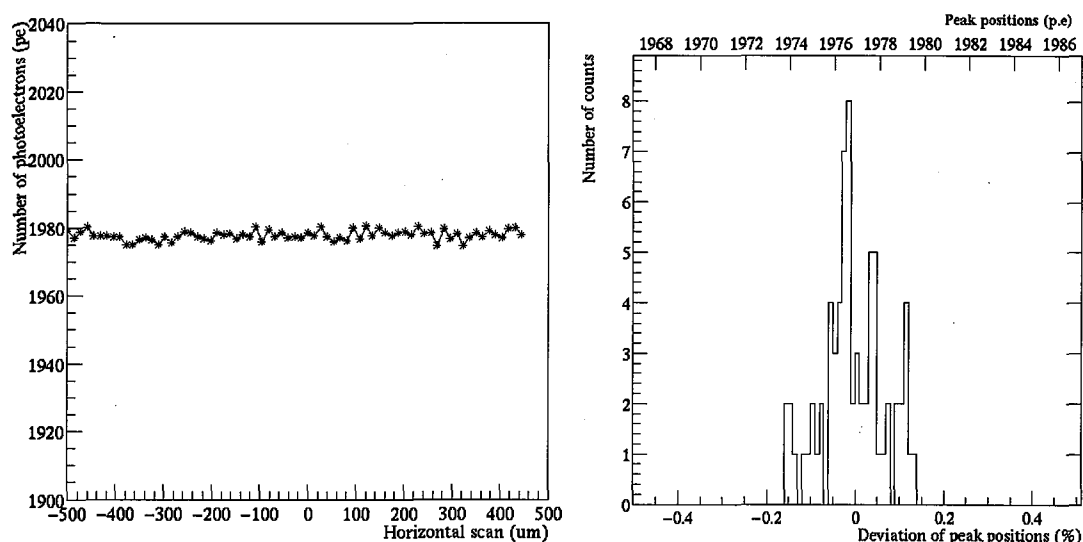
Fig. 3.5.3 Results of 1 dimension scan of the 2.8-MeV proton micro beam.

   a. Peak positions (photoelectrons) versus the horizontal scan analyzed with spatial cell down to 13.5 μm (near the beam size of protons).

   b. Distribution of peak position of the 2.8-MeV proton micro beam for 1 dimension scan. The upper horizontal scale refers to peak positions (photoelectrons).

   In the case of 1-D scan, the uniformity is measured in the cell size of 13.5 μm. we get more statistical events to analyze the uniformity of plastic scintillator materials with spatial cell down to 13.5 μm (the proton beam size is 12 μm). The experimental result of 1-D line scan is shown in Fig. 3.5.3, where Fig. 3.5.3.a is the peak positions (photoelectrons) are plotted against the horizontal position. Fig. 3.5.3b is the corresponding distribution of peak positions. The deviation is within 0.2 %.

   This result shows that the intrinsic resolution would not be caused by the effect of the 10-μm scale inhomogeneity of the plastic-scintillator materials.

3.6 Energy resolution with different thickness of BC-408

   A part of electron energy may escape as γ/X-ray from the plastic scintillator. It may cause the excess component in the energy resolution. This effect depends on the thickness of the plastic scintillator. Changing thickness of the plastic scintillator, we measure energy resolution. In this work, two samples of the plastic scintillators BC-408, (6cm×6cm×1cm) and (6cm×6cm×2cm), are used. The 0.975-MeV conversion electron from the [207]Bi source is employed for measuring the energy resolution. Fig. 3.6.1 and Table 3.6.1 shows the obtained results for the two thicknesses of the plastic scintillator. The uncorrelated component and the intrinsic energy resolution are

compared. Results in Table 3.6.1 show that, within the error bar, these two components show no difference for two different thicknesses of the plastic scintillator BC-408. The number of photoelectrons for 2-cm thick BC-408 is slightly larger than that for the 1-cm thick BC-408. It is (5 ± 2) %. The intrinsic energy resolution yields the same results in these thicknesses.
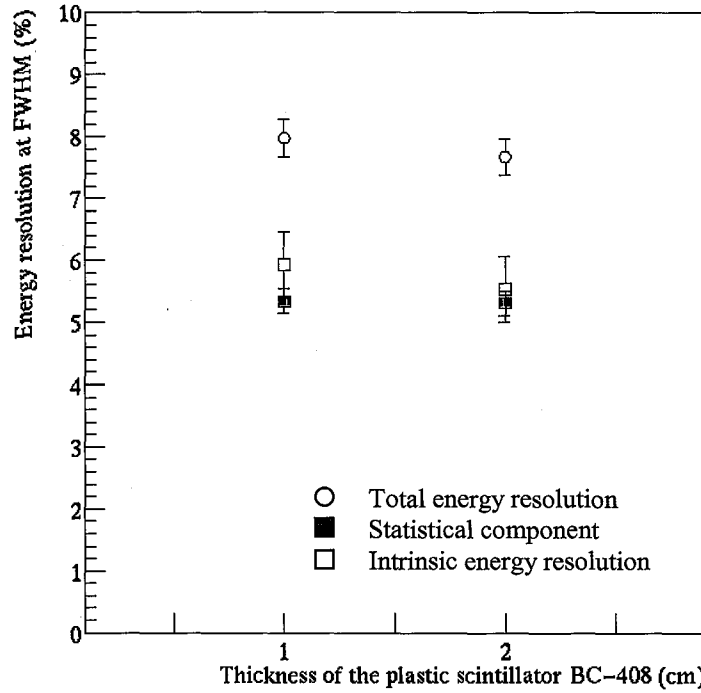
Fig. 3.6.1 A comparison of the energy resolution with different thickness (1-cm thick and 2-cm thick) for the 0.975-MeV electrons. The components of the energy resolution for electrons yield the same results. Total energy resolution (circle point); the statistical component (closed square); intrinsic energy resolution (open square).

Table 3.6.1 A comparison of the energy resolution with different thickness (1-cm thick and 2-cm thick) for the 0.975-MeV electrons

	In FWHM (%)	
	1-cm thick	2-cm thick
Number of photoelectron	2240 ± 40	2360 ± 40
Total energy resolution, R_{tot}	7.98 ± 0.30	7.67 ± 0.30
Statistical component, R_{sta}	5.34 ± 0.20	5.31 ± 0.20
Intrinsic energy resolution, R_{int}	5.92 ± 0.54	5.53 ± 0.54

3.7 Increase photo collection efficiency

Photo collection efficiency affects the resolution only in statistical component. If the excess component is because of the intrinsic property of the plastic scintillator,

it should not depend on the photo collection efficiency. We study the effect of photo collection efficiency on the excess component.

We carry out a measurement in increasing photo collection efficiency, by using the Enhanced Specular Reflector (ESR) [36] covering the remaining sides of the plastic scintillator. The size of BC-408 is (6cm×6cm×1cm). The reflector used in this experiment is the 65-μm ESR foil made of the polymer film with reflectance > 98 % and non-metallic [36]. The reflector is used to cover the sides up and down of the plastic scintillator, shown in Fig. 3.7.1. The experimental arrangement for this detector is the same as the previous set-up i.e. 4 square PMTs covering 4 sides of the plastic scintillator. The 0.975-MeV conversion electron from the ^{207}Bi source is used. The source is put at the center of the plastic scintillator. The statistical component and the intrinsic energy resolution of the plastic scintillator with the reflector are measured and compared to that of the plastic scintillator without the reflector. Here, the statistical component is obtained from the uncorrelated component between PMT$_{13}$ and PMT$_{24}$.

Plastic scintillator BC-408
(6×6×1) cm^3

65-μm thick enhanced specular reflector
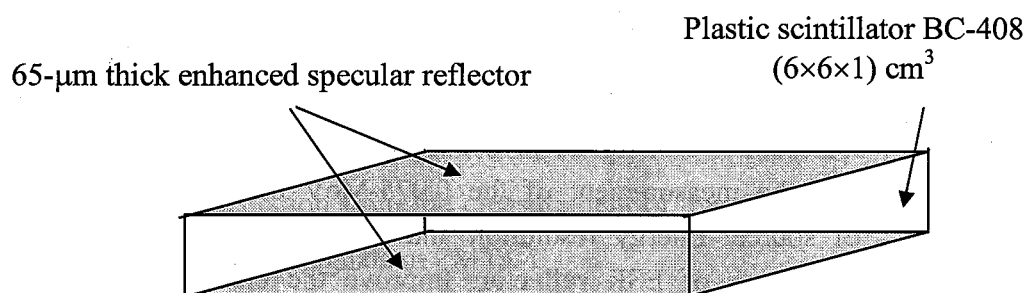
Fig. 3.7.1 The plastic scintillator BC-408 with the enhanced specular reflector (ESR) made of the polymer film is covered to the faces up and down. The experimental arrangement is similar to previous one with 4 square PMTs covering 4 sides. The ESR has reflectance >98% and non-metallic [45].

The results obtained are shown at Fig. 3.7.2 and Table 3.7.1.

The peak positions without and with ESR reflector for the 975-keV conversion peak are obtained as (2240 ± 40) p.e. and (2790 ± 50) p.e., respectively. It means, there are about 24 % more photoelectrons collected at PMTs with the ESR reflector.

Fig. 3.7.2 shows energy resolution of BC-408 for without and with ESR reflector at 0.795-MeV conversion electron. The total energy resolution (open circle) of the scintillator detector is improved. This improvement of the energy resolution results from increasing the number of photoelectrons. It causes the improvement of

statistical component. The intrinsic resolution for these two cases shows within error bar.

Energy resolution at FWHM (%)

10
9
8
7
6
5
4
3
2
1
0

O   Total energy resolution
■   Statistical component
□   Intrinsic energy resolution

BC-408 without ESR reflector   BC-408 with ESR reflector
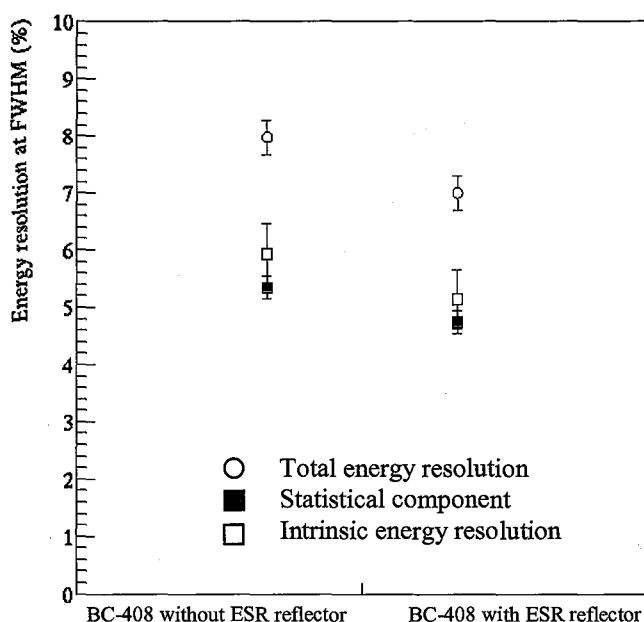
Fig. 3.7.2 The measurement of the 0.975-MeV of internal conversion electron from ^{207}Bi source is used. Energy resolution of the plastic scintillator BC-408 without and with 65-μm thick ESR reflector. Energy resolution is improved by increasing the photo collection. It shows good agreement with the LED data.

Table 3.7.1 Data of the measurement of the 0.975-MeV of internal conversion electron from ^{207}Bi source. Energy resolution and number of photoelectrons for without and with the uses of ESR reflector. Improve the energy resolution by increasing photo collection efficiency with the 65-μm thick ESR reflector.

Plastic scintillator BC-408	Energy resolution in FWHM (%)	
	1-cm thick without reflector	1-cm thick with reflector
Total energy resolution, R_{tot}	7.98 ± 0.30	6.99 ± 0.30
Uncorrelated component	5.34 ± 0.20	4.74 ± 0.20
Intrinsic energy resolution, R_{int}	5.92 ± 0.54	5.14 ± 0.51
Number of photoelectrons	2240 ± 40	2790 ± 50
Statistical component obtained from the calculation: $R_{stat} = \dfrac{2.35 \times 100}{N^{1/2}} \times (1+\varepsilon)^{1/2}$; $\varepsilon = 0.12$	5.2 ± 0.1	4.7 ± 0.1

4. DISCUSSION

We study the energy resolution of the plastic scintillation detector. The statistical component of the energy resolution is analyzed. We show there is an "excess" component in total resolution in addition to the statistical component. Several possibilities of the origin of the "excess" component are studied. None of them can explain the excess component. We conclude the excess component come from the intrinsic property of the plastic scintillator. Based on those analyses, the energy resolution for the sum energy of 2 beta rays at the region of interest (3.034 MeV) is estimated. Taking into account the intrinsic component, we discuss the limitation of the detection sensitivity to the 0ν-$\beta\beta$ signals using plastic scintillation detector.

4.1 Energy resolution in components for electrons and protons

4.1.1 Statistical component

To discuss the statistical component of total energy resolution, we rely on the number of photoelectrons. The statistical component is measured by two methods, namely, 1. the calculation from the measurement of the number of photoelectrons; 2. the correlation between signals in PMTs.

In the first method, the statistical component is calculated from the number of photoelectrons, which is obtained using the single photoelectron measurement. The statistical fluctuation of the number of photoelectrons (N) is calculated as $2.35 \times 100 \big/ \sqrt{N}$ (%). Including the variance of the electron multiplication gain in PMT, the statistical component is shown as $R_{sta}(\%) = \dfrac{2.35 \times 100}{N^{1/2}} \times (1 + \varepsilon)^{1/2}$, where, ε is the variance of the single photoelectron signal. This is the method have been used in the previous works.

In addition to that, we introduce another method to obtain the statistical component. This method is based on the correlation measurement of the number of photoelectrons in PMTs. The statistical component is obtained from the uncorrelated component of the number of photoelectrons between PMT_{13} and PMT_{24}.

The results of these two methods show good agreement. It is described in section 3.4.1. The statistical component in the set-up is $5.2/\sqrt{E_{electron}(MeV)}$ % (FWHM).

The measured total energy resolution shows larger than the statistical component. We conclude there is the excess component in addition to the statistical component.

4.1.2 Excess component

We study the excess component. Possible origin of the excess component is considered, namely, position dependence of the photo collection efficiency, uniformity of plastic materials, different photo collection efficiency and different thicknesses of plastic scintillator. Addition to that, energy spread of beams and the electrical noise are also measured.

We discuss the possible contribution on the excess component in terms of the experimental aspect as following paragraph.

4.1.2.1 Position dependence of photo collection efficiency

Photo collection efficiency depends on the hit position in the plastic scintillator. Position dependence may cause anti-correlation in the PMT signals, which affect the measurement of the uncorrelated component i.e. the statistical component. From proton-scanning measurement, there is no position dependence in 2-D scan data with about 1mm × 1mm area. Uncorrelated component is also measured for various sizes of electron collimators, as described in section 2.2.8. There is no difference up to 4 mm in diameter within the error. Therefore, there is no effect of position dependence in the measurement of statistical component. We use collimated beam for the measurement to reduce this effect.

4.1.2.2 Uniformity of plastic-scintillator materials

Non-uniformity of the plastic-scintillator materials may affect energy resolution as the excess component. The uniformity of plastic materials is experimentally observed by scanning proton micro-beam of 2.8 MeV, as described in section 3.5. The beam size of protons is measured as 12 μm in horizontal (x) and 12 μm in vertical (y). Data of two dimension (2D) scan show the deviation of peak positions within 0.2% (FWHM) with a spatial cell of 50 μm × 50 μm in the scanned area of about 1mm ×1 mm. The result of the 1-D scan also describes good uniformity for the plastic scintillator materials. The "excess" component would not result from the effect of the 10-μm scale inhomogeneity of the plastic-scintillator materials.

4.1.2.3 Thicknesses of the plastic scintillator

A part of electron energy may escape as γ/X-ray from the plastic scintillator. It may cause the excess component in the energy resolution. This effect depends on the thickness of the plastic scintillator. Changing thickness of the plastic scintillator, we measure energy resolution. In this work, we use 1-cm thick plastic scintillator (6cm×6cm×1cm). We compare the excess component with 2-cm thick plastic scintillator (6cm×6cm×2cm). The 0.975-MeV conversion electron is employed to measure the "excess" component, as described in section 3.6. The result shows in Table 4.1.1. The excess component is found no difference in both cases. Therefore, the excess component does not come from the escaping energy from the plastic scintillator.

4.1.2.4 Photo collection efficiency

Photo collection efficiency affects the resolution only in statistical component. If the excess component is because of the intrinsic property of the plastic scintillator, it should not depend on the photo collection efficiency. We study the effect of photo collection efficiency on the excess component. ESR reflector (Enhanced Specular Reflector) is used to increase the photo collection efficiency, as described in section 3.7. It increases the photo collection efficiency 24 %. The result is shown in Table 4.1.1. The total energy resolution is shown better for the plastic with the ESR reflector than the plastic without the use of the reflector. The improvement results from the statistical component. The excess component also changes. However, 24 % difference of photo yield is not good enough to discuss the difference of the excess component because of their error.

Table 4.1.1 The energy resolution for different thickness and with the ESR reflector.

	1-cm thick	2-cm thick	1-mm thick with ESR reflector
Number of photoelectrons	2240 ± 40	2360 ± 40	2790 ± 50
Total resolution	7.98 ± 0.30	7.67 ± 0.30	6.99 ± 0.30
Uncorrelated or statistical component.	5.34 ± 0.20	5.31 ± 0.20	4.74 ± 0.20
"Excess" component	5.92 ± 0.54	5.53 ± 0.54	5.14 ± 0.51

4.1.2.5 Energy spread of electron and proton beam

The energy spread may contribute into the excess component. We measure the energy spread of electron beam and proton micro-beam by Si(Li) and PIPS detector, respectively. The energy spread for the 1-MeV electron beam is about 1.8 %. It is mainly because of the Si(Li) detector resolution. The energy spread for proton micro-beam of 2.8 MeV and 3.4 MeV are measured within 1 %. They are small compared to the obtained excess component. Therefore, the energy spread of the beam cannot explain the excess component.

4.1.2.6 Electrical noise

The electrical noise may affect to the energy resolution. We measure the pedestal signal. The random noise and the ADC conversion error may make the pedestal wider. However, experimental data show that the deviation of the pedestal signal is measured within 1 ADC channel. It is much smaller than that of the signal interest.

The coherent electrical noise affects the energy resolution in the excess component. We use the 475-nm LED flash to measure the coherent electrical noise. The result shows that the excess component in the LED measurement is less than 1 %, including the fluctuation of photo emission of the LED. That means the contribution of the coherent electrical noise in the "excess" component of interest for electrons and protons is less than 1%.

4.2 Intrinsic energy resolution

We studied possible origin of the excess component, as described in section 4.3. None of them can explain the excess component. The fluctuation of the photo collection process does not affect the excess component. Therefore, we conclude that the "excess" component is the intrinsic property of the plastic scintillator i.e. intrinsic energy resolution.

The intrinsic energy resolution is studied for electrons and protons. The obtained results are shown in Fig. 4.2.1c. Here, Fig. 4.2.1a and Fig. 4.2.1b show total energy resolution and the statistical component, respectively. The result for the 0.975-MeV conversion electron shows good agreement with the electron-beam data.

The intrinsic energy resolution in Fig. 4.2.1c shows that, for electrons, the intrinsic resolution shows energy dependence. For protons, it is found to be smaller than that for electrons. It may tell us the hint of the origin of the intrinsic energy

resolution of the plastic scintillator. In matter, the stopping process of electron is quite different from that of proton. It might cause the difference in the intrinsic energy resolution. However, this explanation is not yet found. It should be studied further.
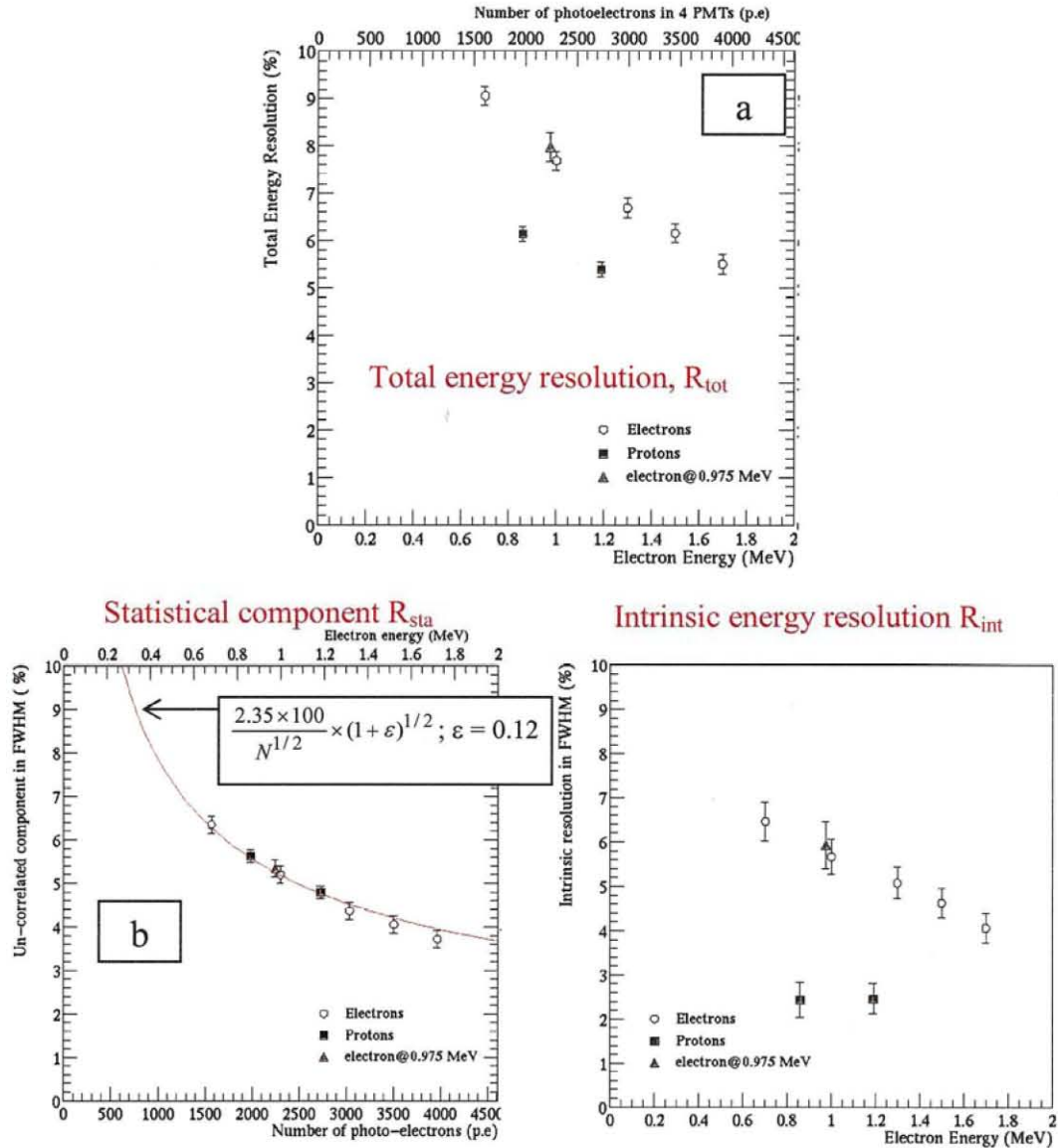

Fig. 4.2.1 Energy resolution for electrons and protons is plotted in electron energy scale. The 0.975-MeV conversion electron is used in comparison with electron beam data. It shows good agreement with electron-beam data.

a. Total energy resolution for electrons and protons.

b. Statistical component for electrons and protons. Here, two methods are mentioned in Figure. They all show consistent. Here, data points of electrons and protons are the uncorrelated component. The red curve is plotted as the equation $R_{sta} = \dfrac{2.35 \times 100}{N^{1/2}} \times (1 + \varepsilon)^{1/2}$, where, N is the number of photoelectrons and $\varepsilon = 0.12$.

c. The intrinsic energy resolution for electrons is lager than that for protons.

4.3 Comparison of energy resolution between small and large plastic scintillator

In previous work [16], with large plastic scintillator (53cm×53cm×1cm), the energy resolution is measured as 11.8 % at 1 MeV. The number of photoelectrons is obtained about 1900 photoelectrons. It corresponds to statistical component of 5.7 %, including the variance of electron multiplication gain, $\varepsilon = 0.12$.

In this work, for small plastic scintillator (6cm×6cm×1cm), the energy resolution is measured as 7.5 % at 1 MeV with the number of photoelectrons obtained as 2300 photoelectrons, corresponding to the statistical component of 5.2 %.

The propagation process of the scintillation photon depends on the shape and the size of the plastic scintillator. It does not affect the correlated fluctuation. It only changes the number of photo electrons and affects the statistical component.

The intrinsic energy resolution is found in small plastic scintillator as 5.6 % at 1 MeV. The intrinsic resolution is believed to relate the stopping process of particle in the material. It should not depend on the size. In other words, there would be no difference in the intrinsic resolution. Taking into account the statistical and intrinsic components for large plastic scintillator, we expect 8.0 % (FWHM) energy resolution at 1.0 MeV. Therefore, with large plastic scintillator, there would be an additional component.

One difference in those two measurements is beam size. In this work, we carefully measure the resolution as position dependence of photo collection efficiency is small. In large plastic scintillator, we use electron by Compton scattering as electron source. It might be the cause to explain the difference.

Another difference is the amount of PMTs used in measurement. In the large plastic scintillator, 32 PMTs are employed to cover 4 sides of the plastic scintillator. The electrical noise takes more importance role in large plastic scintillator.

However, it needs more work in the future to study for large plastic scintillator, so as to improve the energy resolution. It is important for next generation detector.

4.4 Evaluation of energy resolution for 2β-ray sum energy

We evaluate the energy resolution of plastic scintillation detector for 2β-ray sum energy in the 0ν-ββ energy region of interest (3 MeV). Fig. 4.4.1 shows the energy resolution (FWHM) plotted against the electron energies (MeV). Here, open circle and triangle points stand for electron beam data and the 0.975-MeV conversion electron, respectively. The energy resolution has energy dependence of $\sim \frac{1}{\sqrt{E}}$ in the region from 0.7 MeV to 1.7 MeV. One uses the equation of $R(\%) = \frac{R_0}{\sqrt{E(MeV)}}$ to express the energy resolution R as a function of energies E, where R_0 is obtained from the measurement. From fitting line in Fig. 4.4.1a, we obtain $R_0 = 7.5$ %.

The energy resolution for 2β-ray sum energy is evaluated. Denoting the kinetic energy of each beta ray as E_1 and E_2, the Energy spread of those electrons is

$$\Delta E_1 = R_0 \sqrt{E_1} \qquad \text{and} \qquad \Delta E_2 = R_0 \sqrt{E_2} \qquad (4.4.1)$$

The energy spread of 2β- ray sum energy (E) of the plastic scintillator, ΔE, is

$$\Delta E \equiv \Delta(E_1 + E_2) = \sqrt{\Delta E_1^2 + \Delta E_2^2} = R_0 \sqrt{E_1 + E_2} \qquad (4.4.2)$$

The energy resolution for 2β-ray sum energy of will be $\frac{R_0}{\sqrt{E}}$, where, $E = E_1 + E_2$.

From our measurement, the energy resolution for 2β-ray sum energy is described as $\frac{7.5}{\sqrt{E(MeV)}}$ for double beta experiment. Therefore, at 3.034 MeV region it is 4.3 ± 0.1 (%) at FWHM. Using the ESR reflector to cover the faces up and down of the plastic scintillator i.e. to enhance photo collection efficiency, the energy resolution for 2β-ray sum energy can be improved at $\frac{6.9}{\sqrt{E(MeV)}}$. It corresponds to 4% (FWHM) at 3.034-MeV region.

The intrinsic energy resolution found in the plastic scintillator for electrons has energy dependence. Refer to the previous work [16], the total energy resolution is to follow the 1/sqrt(E) energy dependence. Our data shows that the total energy resolution also follows that equation. Moreover, the statistical term is described as 1/sqrt(E) energy dependence. Since the intrinsic one is derived from the statistical term subtracting from the total energy resolution. Then, it may describe as 1/sqrt(E) energy dependence. Therefore, the intrinsic resolution is fitted as the

equation $R_{int} = P_1/\sqrt{E}$, $P_1 = (5.6 + 0.2)$ %, where E refers to electron energies in MeV. It is shown in Fig. 4.4.1b.

If the detector takes all scintillation photon (~10000 scintillation photon/MeV), the energy resolution for 2β-ray sum energy is limited to 3.4 % (FWHM) at 3.034-MeV region.
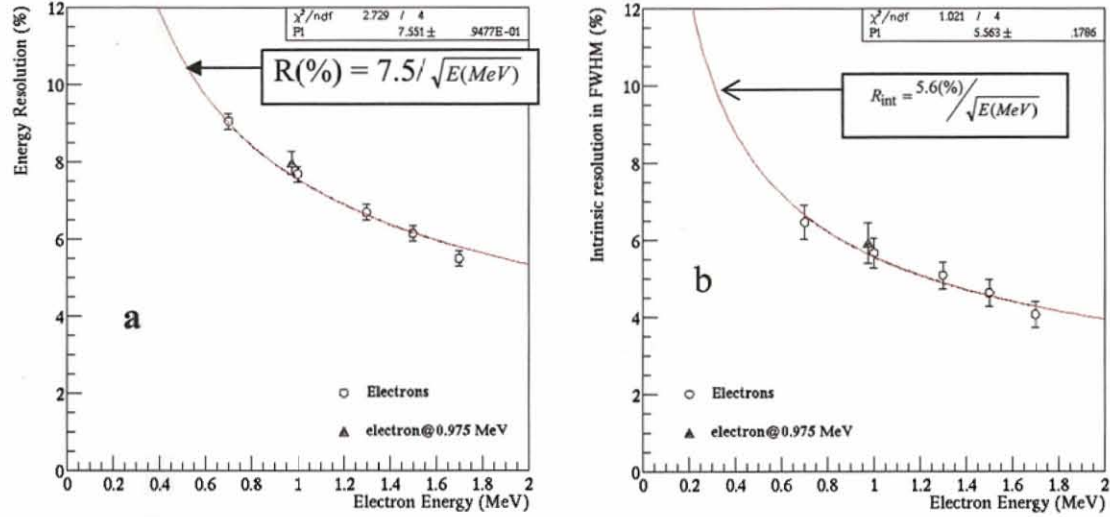

Fig 4.4.1 Energy resolution of plastic scintillation detector as a function of the electron energy.
   a. Total energy resolution
   b. Intrinsic energy resolution.

4.5 Detection sensitivity to half life of 0ν-ββ decays (Monte-Carlo simulation)

The intrinsic energy resolution is found in the plastic scintillation detector. We estimate how this intrinsic component affects the detection sensitivity of 0ν-ββ signals by Monte-Carlo simulation. The details of the simulation are explained at Appendix B.

The energy resolution, R, of 4 %, 6.8 % and 3.4 % (FWHM) in 3.034-MeV region is discussed. Here, R = 4 % is achieved for small-size plastic scintillator (6cm×6cm×1cm) in this work. 6.8 % is for large-size plastic scintillator (53cm×53cm×1cm) [16]. R = 3.4 % is the energy resolution of the detector limited by the intrinsic energy resolution.

Fig. 4.5.1 shows the predicted spectrum of 0ν-ββ (signal of interest) and 2ν-ββ (background signal). It is obtained for $N_{2\nu\text{-}\beta\beta}/N_{0\nu\text{-}\beta\beta}$ ratio of 10^6, finite energy

resolution of 4.0 % in FWHM at Q-value (3.034 MeV). The energy loss in ^{100}Mo foil of 40 mg/cm^2 is taken into account.

No background by radio activity takes into account. Only 2ν-ββ events are counted on as background events. Here, half life of 2ν-ββ decay of 7.1×10^{18} years is used.

The signal region is defined at the energy region of $^{0\nu\beta\beta}/_{2\nu\beta\beta}$ ratio ≥ 1:1 (shaded area in Fig. 4.5.1). The statistical significance of 0ν-ββ event in the signal region is evaluated as:

$$n[\sigma] = \frac{N_{0\nu}}{\sqrt{N_{0\nu} + N_{2\nu}}}$$

Where, $N_{0\nu}$ and $N_{2\nu}$ are the integrated number of events for 0ν-ββ and 2ν-ββ, respectively.

Fig. 4.5.2 shows the obtained statistical sensitivity, n[σ], as a function of 0ν-ββ half life using 1-ton ^{100}Mo foil (40 mg/cm^2) and 10-year measurement.

Requiring about 6-σ statistical significance, the energy resolution is plotted as a function of the 0ν-ββ half life, which is shown in Fig. 4.5.3. The energy resolution of 4 % (small plastic scintillator) can meet the sensitivity of the 0ν-ββ half life up to ~ 1.2×10^{26} years. It is close to the limitation the detector (green line). However, with 6.8 % resolution (large plastic scintillator), the detector is only sensitive to 3.7×10^{25} years.

There is a large difference between 4 % and 6.8 % energy resolution to the sensitivity of 0ν-ββ half life. It is necessary to improve the energy resolution for large-size plastic scintillator.

In this work, the plastic scintillation detector with the energy resolution of 4% (FWHM) at 3.034-MeV energy region can meet the 0ν-ββ half life up to ~ 1.2×10^{26} years. The obtained results also show that the energy resolution of 4 % is close to the limitation of the detector (3.4 %). The plastic scintillator can be used for the next generation double beta decay experiment, MOON and SuperNEMO.
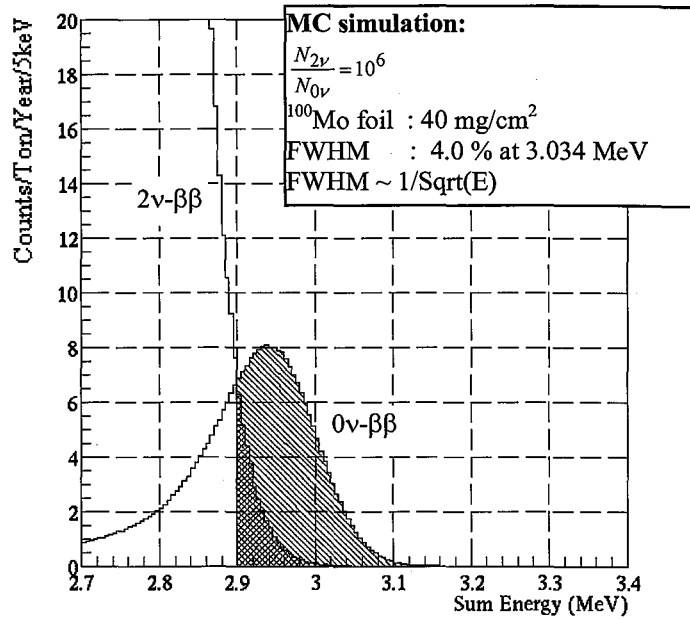
MC simulation:

$\dfrac{N_{2\nu}}{N_{0\nu}} = 10^6$

^{100}Mo foil : 40 mg/cm^2

FWHM : 4.0 % at 3.034 MeV

FWHM ~ 1/Sqrt(E)

Counts/Ton/Year/5keV

2ν-ββ

0ν-ββ

Sum Energy (MeV)

Fig. 4.5.1 The spectrum of 0ν-ββ (signal of interest) and the 2ν-ββ (background signal) with assumptions as following:

$N_{2\nu\text{-}\beta\beta}/N_{0\nu\beta\beta}$ ratio is 10^6, the energy loss in ^{100}Mo foil (40 mg/cm^2 thick), and finite energy resolution of 4 % (FWHM) at 3.034 MeV.
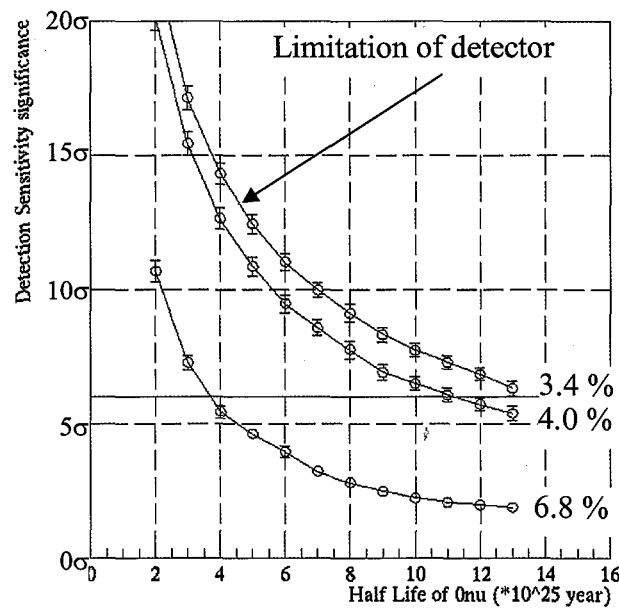
Detection Sensitivity significance

Limitation of detector

3.4 %

4.0 %

6.8 %

Half Life of 0nu (*10^25 year)

Fig. 4.5.2 Detection sensitivity, n[σ], is plotted against the to the 0ν-ββ half life with different finite energy resolution using 1 ton ^{100}Mo foil (40 mg/cm^2 thick) and 10-year measurement. The blue line shows the sensitivity statistical significance of 6σ.
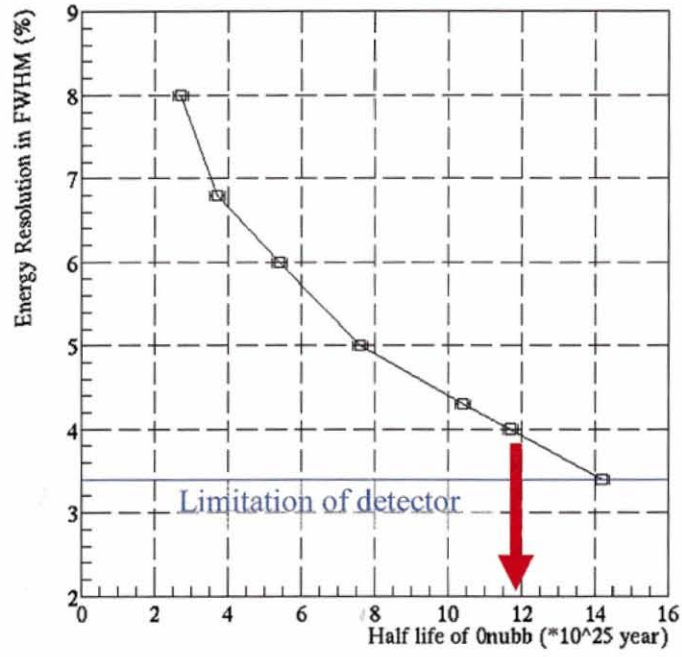
Fig 4.5.3 Energy resolution of the plastic scintillation detector is as a function of 0ν-ββ half life. With energy resolution of 4 %, the detector can meet the sensitivity of 0ν-ββ half life up to ~ 1.2×10^{26} years, corresponding to the effective neutrino mass ~ 50 meV. The blue line shows the limitation of the detector.

5. SUMMARY AND REMARKS

In next generation neutrinoless double beta decay experiments, MOON and SuperNEMO claim the sensitivity $0v$-$\beta\beta$ half life up to 10^{26} years. Good energy resolution is the key to achieve the high sensitivity to $0v$-$\beta\beta$ signals. To achieve that goal, it is necessary to study the energy resolution.

In this work, we use small plastic scintillator (6cm×6cm×1cm) with 4 PMTs covering 4 sides of plastic scintillator. This arrangement obtains high photo collection efficiency and the correlation between signals in PMTs. It is used to study the energy resolution in components.

We employ the mono-energetic electron beams in the range of energies from 0.7 MeV to 1.7 MeV extracted from the electron spectrometer. The 0.975-MeV conversion electron from ^{207}Bi radioactive source is also used. Proton micro-beams with energies of 2.8 MeV and 3.4 MeV are used for comparison with electron data. Several additional experiments are also performed to discuss the energy resolution.

The obtained results can be described as following:

1. Statistical component
Statistical component in total energy resolution is discussed in two methods.

- One is evaluated by the calculation from statistical fluctuation of the number of photoelectrons and the variance of the electron multiplier gain in PMT. The number of photoelectrons obtained in this set-up is 2300 photoelectrons for 1-MeV electrons. The variance of the electron multiplier gain in the PMT is 0.12.

- The other is based on the correlation measurement of PMT signals. The statistical component is obtained from the uncorrelated component of the number of photoelectrons between PMT_{13} and PMT_{24}.

Both results show good agreement, as described in section 3.4.1. The statistical component in the set-up is $\dfrac{5.2}{\sqrt{E_{electron}(MeV)}}$ (% in FWHM).

2. The excess component
The excess component is derived from subtracting the statistical component from the total energy resolution. Several contributions on the excess component in terms of the experimental aspect are studied as following:

- The electrical noise is confirmed small by the measurements of the pedestal and the correlation between signals of LED flash. The effect of electrical noise is less than 1%.

- The energy spread for electrons and protons is confirmed small within 1 % (FWHM) by Si(Li) and PIPS detectors, respectively. It does not much affect the excess component.

- The position dependence of the photo collection efficiency shows no difference for the beam collimator up to 4 mm in diameter, as described in section 2.2.8. We use collimated beam for the measurement to reduce this effect.

- The escaping energy from plastic scintillator does not affect the energy resolution of the plastic scintillator in the measurements of different thicknesses (1-cm thick and 2-cm thick). It is described in section 3.6.

- The measurement for different photo collection efficiency show that the excess component is within the error, as described in section 3.7.

❖ Those contributions do not affect the excess component. The excess component is suggested to be the intrinsic property of the plastic scintillator i.e. the intrinsic energy resolution.

❖ To study the origin of the intrinsic energy resolution, several possibilities are considered as:

- The uniformity of the plastic scintillator materials by scanning 2.8-MeV proton micro beam is very good as less than 0.2 % in the 10-μm scale, as described in section 3.5. It is far from the intrinsic energy resolution.

- None of those studies can explain the intrinsic energy resolution. We compare that for electron and proton. The results show the large intrinsic energy resolution for electrons and a small one for protons. In matter, the stopping process of electron is quite different from that of proton. The difference might be related to different stopping process of both particles in matter. It may tell us the hint of the origin of the intrinsic energy resolution of the plastic scintillator. However, this explanation is not yet found. It should be studied further.

3. The energy resolution of sum 2-β ray energy for plastic scintillation detector

The energy resolution of the plastic scintillation detector is limited by the intrinsic energy resolution. With small size of the detector (6cm×6cm×1cm), the energy resolution is close to the limitation of the plastic scintillation detector. The

energy resolution for the sum energy of 2 β rays at 3.034-MeV energy region is evaluated as (4.3 ± 0.1) % in FWHM. Increasing the photo collection efficiency by using the ERS reflector, it can be achieved up to 4.0 %. It is close to the limitation of the detector.

4. Estimate the statistical significance for 0v-$\beta\beta$ decays

The next generation double beta decay experiments, MOON and SuperNEMO, would use about several hundred kg to 1-ton of source material for their detector. Using the obtained results of the energy resolution for the plastic scintillator detector, we estimate the sensitivity of the detector using the plastic scintillator for ^{100}Mo foil of 40 mg/cm^2. It is described in appendix B. The energy resolution of the plastic scintillation detector is limited by the intrinsic energy resolution, which we found in this work. It is hard to measure the neutrino mass region beyond inverted hierarchy case. However, it is possible to obtain around 6σ statistical significance in 10- ton·year measurement for inverted mass hierarchy case, which corresponds to the 0v-$\beta\beta$ half life $\sim 10^{26}$ years. In short, the plastic scintillator can be used for the next generation double beta decay experiment, MOON and SuperNEMO.

REFERENCES

[1] H. Ejiri, *J. Phys. Soc. Japan*, 74, 2101, 2000

[2] S. R. Elliott and P. Vogel, "Double beta decay," *Annu. Rev. Nucl. Part. Sci.* 52, 115-151, 2002.

[3] R. Arnod et al., "First results of the search for Neutrinoless Double-beta decay with the NEMO 3 detector," *Phys. Rev. Lett.* 95, 182302, 2005.

[4] H. Ejiri, J. Engel, R. Hazama, P. Krastev, N. Kudomi, R.G.H. Robertson, "Spectroscopy of double-beta and inverse-beta decays from Mo-100 for neutrinos," *Phys. Rev. Lett.* 85, 2917-2920, 2000.

[5] M. Nomachi et al., "MOON (Mo Observatory Of Neutrinos) for double beta decay," *Nucl. Phys. Proc.* Suppl. 138, 221-223, 2005.

[6] SupperNEMO (Neutrino Ettore Majorana Observatory) collaboration, 2007.

[7] M. Moszynski et al, "Intrinsic energy resolution of NaI(Tl)", Nucl. Instr and Meth 484, 259 – 269, 2001.

[8] C. Kuntner et al., "Intrinsic energy resolution and light output of the $Lu_{0.7}Y_{0.3}AP$:Ce scintillator", Nucl. Instr. And Meth 493, 131 – 136, 2002.

[9] Supper-Kamiokande Coll., Y.Fukuda et al., Phys.Rev.Lett. 86 5651, 2002.

[10] S.N. Ahmed et al., Phys.Rev.Lett. 92 181301, 2004

[11] KamLAND Coll., K. Eguchi et al., Phys.Rev.Lett. 90 021802, 2003.

[12] Particle data group, http://pdg.lbl.gov

[13] Y. Ashie et. al, "Evidence for an Oscillatory signature in atmospheric neutrino oscillations", Phys. Rev. Lett. 93, 101801, 2004

[14] B. Aharmim et. al, Phys. Rev. C72, 055502, 2005

[15] H. Ejiri, et al., Phys. Rev. Lett. 85 2917, 2000

[16] H. Nakamura, "Development of prototype detector MOON-1 for double beta decay from ^{100}100", Doctoral thesis, Osaka University, 2006.

[17] H Nakamura, "Study of Statistical and Non-Statistical Components of Energy Resolution for High-sensitive Beta Camera," Nuclear Science Symposium, 2006.

[18] CENBG, 2007, personal communication.

[19] K. Yasuda et al., "Ion microbeam facility at the Wakasa Wan Energy Research Center, " *Nucl. Instr. and Meth.,* B210, 27-32, 2003.

[20] Bi-207 source BIRB1082, Entsys Technologies Co., LTD., http://www.entsys-tech.com

[21] BC-408 specification, Saint-Gobain Ceramics & Plastic, Inc., http://www.detectors.saint-gobain.com.

[22] Photo-multiplier tube R6236-01 specifications, Hamamatsu Corporation, http://jp.hamamatsu.com.

[23] Silicone optical grease BC-630 specification, Saint-Gobain Ceramics & Plastic, Inc., http://www.detectors.saint-gobain.com.

[24] F1AH0535 magnetic shielding sheet specification, Hitachi Metals, Ltd., http://www.hitachi-metals.co.jp

[25] NSHU590A and NSPB500s specifications, NICHIA Corporation, http://www.nichia.com

[26] RPC-022 specifications, REPIC Corporation, http://www.repic.co.jp/products/repic/camac/rpc 022.html

[27] 4 Channel 100 kS/s DAC module, model WE7282, Yokogawa Electric Corporation, https://www.yokogawa.com/

[28] Gilder grid G400SH mesh, Nisshin EM Co., Ltd, http://www.tedpella.com/grids_html/gilder.htm

[29] PIPS detector, Model number PD25-11-300AM, Canberra Industries, Inc., http://www.canberra.com/

[30] 16 Channel peak ADC, CAMAC model 7164, Phillips Scientific, http:/phillipsscientific.com/

[31] FPGA chip EP1C6T144C8 specification, Altera Corporation, http://www.altera.com/

[32] Quartus II software, Altera Corporation, http://www.altera.com/

[33] Trigger module, Laboratory development.

[34] CC/NET specification, TOYO Corporation, http://www.toyo.co.jp/daq/ccnet/

[35] E. Browne, R.B. Firestone, "Table of radioactive Isotopes" book, University of California, 1986.

[36] ESR (Enhanced Specular Reflector) film specification, http://www.3m.com

[37] M. Nomachi, "Intrinsic deviation of scintillation process", Personal discussion, 2006.

[38] M. Nomachi and K. Ogama, "Energy spectrum of electron in double beta decay", Personal discussion, 2004.

[39] Masaru DOI et al., "The energy spectrum and the angular correlation in the $\beta\beta$ decay", Prog. Theor. Phys., 70, (1983), 1353.

[40] M.J. Berger et al., "Stopping-Power and Range Tables for electrons, Protons and Helium Ions", National Institute of Standards and Technology (NIST), http://physics.nist.gov/

[41] T. Ogama, "Energy resolution of MOON-1 detector for 0ν-$\beta\beta$ decay experiment", Master thesis, Osaka University, 2006.

[42] UV-VIS spectrometer USB4000, Ocean Optic Inc., http://www.OceanOptics.com

[43] AFG3102 Arbitrary/Function Generator 2 Channel specification, Tektronix, Inc., http://www.tek.com/

APPENDIX

APPENDIX A:

Theoretical consideration of statistical fluctuation

In this section, the theoretical consideration of the method based on the generating functions will be discussed how the fluctuation of the number of photons emitted by a scintillator affects the variance of the number of photoelectrons at photomultiplier tubes (PMTs) [37]. The discussion is for a single PMT and two PMTs.

A.1 Single PMT

An emitted photon causes a photoelectron in the PMT in probability of p. When the number of photon emitted in the scintillator is M, the provability of having N photoelectron on the PMT is

$$P(M,N) = \frac{M!}{N!(M-N)!} p^N (1-p)^{M-N} \tag{A.1}$$

Assuming the distribution of the number of photon is g_M, the distribution of the number of photoelectrons is shown as follows:

$$h_N = \sum_{M=N}^{\infty} \frac{M!}{N!(M-N)!} p^N (1-p)^{M-N} g_M \tag{A.2}$$

The generating function of this distribution is described as follows, with the introduction of the auxiliary variable (t):

$$H(t) = \sum_{N=0}^{\infty} h_N t^N$$

$$= \sum_{N=0}^{\infty} \sum_{M=N}^{\infty} \frac{M!}{N!(M-N)!} t^N p^N (1-p)^{M-N} g_M$$

$$= \sum_{M=0}^{\infty} \sum_{N=0}^{M} \frac{M!}{N!(M-N)!} t^N p^N (1-p)^{M-N} g_M$$

$$= \sum_{M=0}^{\infty} (tp+1-p)^M g_M$$

Or, $H(t) = G(tp+1-p)$ (A.3)

Where, G is the generating function of the number of photo distribution. Using

$$H'(t) = pG'(tp+1-p) \qquad\qquad H'(1) = pG'(1)$$
$$H''(t) = p^2 G''(tp+1-p) \qquad\qquad H''(1) = p^2 G''(1)$$

The average <N> and the variance (σ_N^2) of the number of photoelectrons can be represented as follows:

$$< N >= H'(1) = p < M >$$ (A.4)

$$\sigma_N^2 = H''(1) + H'(1) - [H'(1)]^2$$
$$= p^2 \sigma_M^2 + p(1-p) < M >$$ (A.5)

Replacing the emitted photon fluctuation $\sigma_M^2 = \sigma_0^2 + < M >$ into the equation 1.7.5 (the variance σ_0^2 is zero if the distribution of M is Poisson distribution).

$$\sigma_N^2 = p^2 \sigma_0^2 + p < M >= p^2 \sigma_0^2 + < N >$$ (A.6)

If there is no additional variance or small probability of p, the variance of the number of photo electron is

$$\sigma_N^2 =< N >$$ (A.7)

where σ_0^2 is the additional variance in the distribution of the number of photon.

A.2 Two PMTs

In the case of two PMTs, an emitted photon causes a photoelectron in the PMT_1 or PMT_2 in probability of p_1 and p_2, respectively. When the number of photons emitted in the scintillator is M, the provability of having N_1 on the PMT_1 and N_2 photoelectron on the PMT_2 is given by:

$$P(M, N_1, N_2)$$
$$= \frac{M!}{N_1! N_2! (M - N_1 - N_2)!} p_1^{N_1} p_2^{N_2} (1 - p_1 - p_2)^{M - N_1 - N_2}$$ (A.8)

Now we will consider the summation $(N_1 + N_2)$ and difference $(N_1 - N_2)$ of the number of photoelectrons.

* The probability of the summed number of photoelectrons is

$$P_{ADD}(M, N) = \sum_{N_1 = 0}^{N} P(M, N_1, N - N_1)$$

$$= \sum_{N_1 = 0}^{N} \frac{M!}{N_1! (N - N_1)! (M - N)!} p_1^{N_1} p_2^{N - N_1} (1 - p_1 - p_2)^{M - N}$$

$$= \sum_{N_1 = 0}^{N} \frac{N!}{N_1! (N - N_1)!} \frac{M!}{N! (M - N)!} p_1^{N_1} p_2^{N - N_1} (1 - p_1 - p_2)^{M - N}$$

Or, $P_{ADD}(M, N) = \frac{M!}{N! (M - N)!} (p_1 + p_2)^N (1 - p_1 - p_2)^{M - N}$ (A.9)

Here, $N = N_1 + N_2$ is the summed number of photoelectrons.

Comparing Eq. A.9 to A.1, the distribution is the same as the case of single PMT. The average number of photoelectrons is

$$< N >= (p_1 + p_2) < M > \tag{A.10}$$

The variance of summed photoelectrons is

$$\sigma_N^2 = (p_1 + p_2)^2 \sigma_M^2 + (p_1 + p_2)(1 - p_1 - p_2) < M >$$
$$= (p_1 + p_2)^2 \sigma_0^2 + (p_1 + p_2) < M >$$

Or, $\quad \sigma_N^2 = (p_1 + p_2)^2 \sigma_0^2 + < N > \tag{A.11}$

* Describing the difference of the number of photoelectron as follows:

$$D = N_1 - N_2 \tag{A.12}$$

The probability of D is

$P_{SUB}(M,D)$

$$= \sum_{N_2=0}^{M} \sum_{N_1=0}^{M-N_2} \frac{M!}{N_1! N_2! (M - N_1 - N_2)!} p_1^{N_1} p_2^{N_2} (1 - p_1 - p_2)^{M - N_1 - N_2} \delta(D - N_1 + N_2) \tag{A.13}$$

Assuming the distribution of the number of photon is g_M, the distribution of D is

$h_{SUB}(D)$

$$= \sum_{M=|D|}^{\infty} \sum_{N_1=0}^{M} \sum_{N_2=0}^{M-N_1} \frac{M!}{N_1! N_2! (M - N_1 - N_2)!} p_1^{N_1} p_2^{N_2} (1 - p_1 - p_2)^{M - N_1 - N_2} \delta(D - N_1 + N_2) g_M \tag{A.14}$$

The generating function of this distribution is described as follows:

$H_{SUB}(t)$

$$= \sum_{D=-\infty}^{\infty} \sum_{M=|D|}^{\infty} \sum_{N_1=0}^{M} \sum_{N_2=0}^{M-N_1} \frac{M!}{N_1! N_2! (M - N_1 - N_2)!} t^D p_1^{N_1} p_2^{N_2} (1 - p_1 - p_2)^{M - N_1 - N_2} \delta(D - N_1 + N_2) g_M$$

Changing the order of the summations,

$$\sum_{D=-\infty}^{\infty} \sum_{M=|D|}^{\infty} = \sum_{M=0}^{\infty} \sum_{D=-M}^{M}$$

$$\sum_{D=-M}^{M} \sum_{N_1=0}^{M} \sum_{N_2=0}^{M-N_1} = \sum_{N_1=0}^{M} \sum_{N_2=0}^{M-N_1} \sum_{D=-M}^{M}$$

The generating function is

$H_{SUB}(t)$

$$= \sum_{M=0}^{\infty} \sum_{N_1=0}^{M} \sum_{N_2=0}^{M-N_1} \left(\sum_{D=-M}^{M} \delta(D-N_1+N_2)t^D \right) \frac{M!}{N_1!N_2!(M-N_1-N_2)!} p_1^{N_1} p_2^{N_2} (1-p_1-p_2)^{M-N_1-N_2} g_M$$

$$= \sum_{M=0}^{\infty} \sum_{N_1=0}^{M} \sum_{N_2=0}^{M-N_1} \frac{M!}{N_1!N_2!(M-N_1-N_2)!} t^{N_1-N_2} p_1^{N_1} p_2^{N_2} (1-p_1-p_2)^{M-N_1-N_2} g_M$$

$$= \sum_{M=0}^{\infty} \sum_{N_1=0}^{M} \frac{M!}{N_1!(M-N_1)!} p_1^{N_1} t^{N_1} \left(\sum_{N_2=0}^{M-N_1} \frac{(M-N_1)!}{N_2!(M-N_1-N_2)!} t^{-N_2} p_2^{N_2} (1-p_1-p_2)^{M-N_1-N_2} \right) g_M$$

$$= \sum_{M=0}^{\infty} \sum_{N_1=0}^{M} \frac{M!}{N_1!(M-N_1)!} p_1^{N_1} t^{N_1} \left(\frac{p_2}{t} +1-p_1-p_2 \right)^{M-N_1} g_M$$

$$= \sum_{M=0}^{\infty} \left(p_1 t + \frac{p_2}{t} +1-p_1-p_2 \right)^{M} g_M$$

Or, $H_{SUB}(t) = G(p_1 t + \frac{p_2}{t} +1-p_1-p_2)$ (A.15)

Differentiating the generating function,

$$H'(t) = \left(p_1 - \frac{p_2}{t^2} \right) G'\left(p_1 t + \frac{p_2}{t} +1-p_1-p_2 \right)$$

$$H''(t) = \frac{2p_2}{t^3} G'\left(p_1 t + \frac{p_2}{t} +1-p_1-p_2 \right) + \left(p_1 - \frac{p_2}{t^2} \right)^2 G''\left(p_1 t + \frac{p_2}{t} +1-p_1-p_2 \right)$$

$$H'(1) = (p_1 - p_2)G'(1)$$

$$H''(1) = 2p_2 G'(1) + (p_1 - p_2)^2 G''(1)$$

The average of the difference is obtained as follows:

$$< D >= H'_{DIF}(1)$$
$$= (p_1 - p_2) < M >$$ (A.16)

It is obvious that the average is zero if p_1 is the same as p_2.

The variance of difference is shown as follows:

$$\sigma_D^2 = H''_{DIF}(1) + H'_{DIF}(1) - [H'_{DIF}(1)]^2$$
$$= < N > + (p_1 - p_2)^2 \sigma_M^2 - (p_1 - p_2)^2 < M >^i$$

$$\sigma_D^2 = < N > + (p_1 - p_2)^2 \sigma_0^2$$

It can be found that if the probabilities p_1 and p_2 are the same, the variance of D is statistical fluctuation of photoelectrons i.e.

$$\sigma_N^2 = < N >$$ (A.17)

* Calculation of the difference of variances of N and D:

$$\sigma_N^2 = <N> + (p_1 + p_2)^2 \sigma_0^2$$
$$\sigma_D^2 = <N> + (p_1 - p_2)^2 \sigma_0^2$$
$$\sigma_N^2 - \sigma_D^2 = 4 p_1 p_2 \sigma_0^2$$
$$\frac{\sqrt{\sigma_N^2 - \sigma_D^2}}{<N>} = \frac{2\sqrt{p_1 p_2}}{p_1 + p_2} \frac{\sigma_0}{<M>}$$

(A.18)

In case p_1 is the same as p_2,

$$\sigma_N^2 = <N> + (2 p \sigma_0)^2$$
$$\sigma_D^2 = <N>$$
$$\sigma_N^2 - \sigma_D^2 = (2 p \sigma_0)^2$$

$$\boxed{\frac{\sqrt{\sigma_N^2 - \sigma_D^2}}{<N>} = \frac{\sigma_0}{<M>}}$$

(A.19)

Consequently, the difference of variances of N and D gives the variance of the number of photon. It relates to the "excess" component which is an additional fluctuation to statistical one.

From equation A.17 points out that the statistical fluctuation of the photoelectron can be obtained if photoelectrons collected at cathodes of PMT_1 and PMT_2 is equal in quantity. Fig. A.1 illustrates the correlation of signals between PMT_1 and PMT_2. σ_N and σ_D are the variances along the $\pm 45^0$ axes, respectively. The statistical fluctuation of the number of photoelectrons can be obtained in this method.
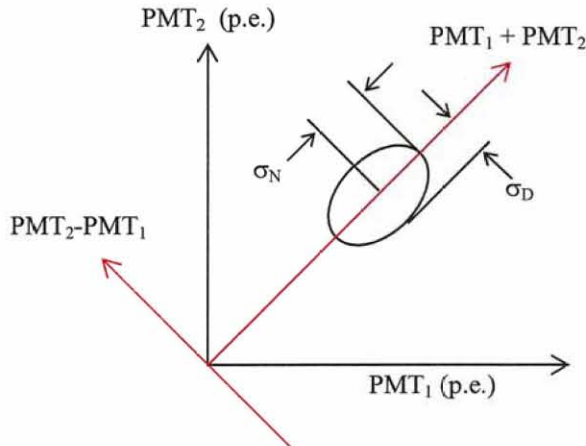

Fig. A.1 Illustration of the correlation of 4 PMTs in terms of the σ_N (variance of $PMT_1 + PMT_2$) and σ_D (variance of $PMT_2 - PMT_1$). σ_N and σ_D are the variances along the $\pm 45^0$ axes, respectively.

APPENDIX B:

Simulation for sensitivity to neutrinoless double beta decay

In this section, the sensitivity to $0\nu\beta\beta$ signals is studied with Monte-Carlo simulation. It is for ^{100}Mo foil, which is considered as a source of double beta decays. The energy loss in ^{100}Mo foil of 40 mg/cm^2 is taken into account. Only 2ν-$\beta\beta$ events are counted on as background events. No background by radioactivity takes into account. Theoretical energy spectrum of double beta decay is referred to [38] and [39]. The simulation deals with the endpoint region of 2ν-$\beta\beta$ spectrum, where 0ν-$\beta\beta$ spectrum appears. The energy deposited in the ^{100}Mo foil is evaluated from NIST data [40]. The detector response of the plastic scintillator is assumed in form of Gaussian function. 500 ton·year events are generated in this simulation to obtain good statistics.

B.1 Assumptions and conditions for simulation

The energy spectrum for double beta decay is referred to [38]. The transition probability of the 2ν-$\beta\beta$ decays is described as follows:

$$\frac{dR}{dT} \propto (Q-T)^5 \times T \times [(T+2mc^2)^4 - \frac{2}{3}(T+2mc^2)^2 T^2 + \frac{1}{5}T^4] \qquad (B.1)$$

And the energy difference of two beta rays is described as:

$$\frac{dR}{dt} \propto ((T+2mc^2)^2 - t^2)^2 \qquad (B.2)$$

where T is the sum energy of two beta rays (T = E$_{e1}$ + E$_{e2}$ − 2mc^2); t is the energy difference of two beta rays (t = E$_{e1}$ − E$_{e2}$). E$_{e1}$, E$_{e2}$ are the energy of each beta ray. mc^2 = 0.511 MeV (mass of the electron). Q is the decay energy. Q = 3.034 MeV for ^{100}Mo.

Fig. B.1a shows the spectrum of the sum energy of two beta rays in the 2ν-$\beta\beta$ decay mode for ^{100}Mo with Q-value of 3.034 MeV.

For neutrinoless double beta decay, the sum energy is the mono-chromatic energy peak. The energy difference of two beta rays in the 0ν-$\beta\beta$ decay mode is described as the same as that of 2ν-$\beta\beta$ decay mode i.e. T = Q in equation B.2. It is shown in Fig. B.1b.
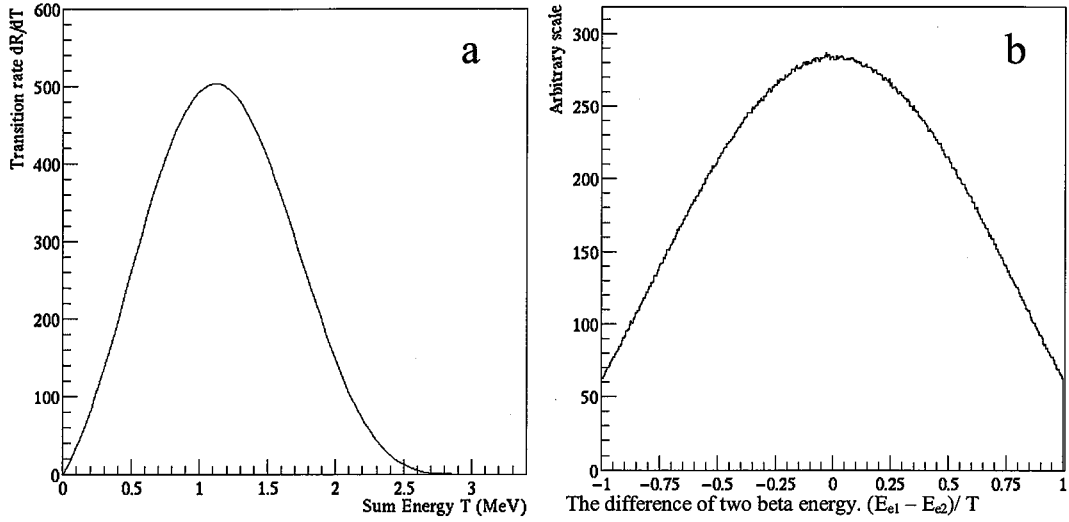
Fig .B1 Spectrum for ^{100}Mo with Q-value of 3.034 MeV.
a. The spectrum of the sum energy of two beta rays in the 2ν-ββ decay mode.
b. The spectrum of the energy difference of two beta rays in the 0ν-ββ decay mode.

B.1.1 Assumptions for the simulation

The assumptions of the simulation for 2ν-ββ and 0ν-ββ signals are described as follows:

- No radioactivity background is taken into account.

- The angular correlation between two beta rays is in condition of $(1 - \cos\theta)$, θ being the angle between two emitted beta rays [39].

- Multiple scattering of electron in foil is not taken into account. Electron is assumed pass straight line.

- The energy loss in the ^{100}Mo foil is evaluated from NIST data [40]. The distribution of the energy loss is not taken into account. Here, the projected range of electron for ^{100}Mo material is shown in Fig. B.1 [40].

- Detector response is assumed as the Gaussian function. The energy resolution of the beta-ray energy is assumed as $R \propto \frac{1}{\sqrt{E(MeV)}}$, where, E is the beta-ray energy.

B.1.1 Conditions for the simulation

This simulation is performed in following conditions:

- 2ν-ββ half life is 7.1×10^{18} years [3].

- 0ν-ββ half life is studied from 2×10^{25} years to 13×10^{25} years.

- In the sum-energy region of interest, the 2ν-ββ events are generated from 2.7 MeV to the endpoint, so as to reduce computation time.

- The two beta event is selected if 2-beta rays hit different plastic scintillators.

- Threshold of the detector is as 0.2 MeV.

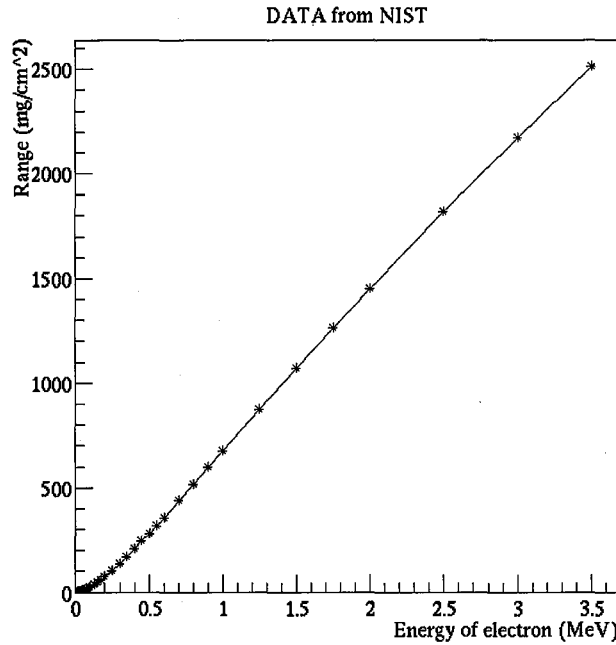- The energy resolution of the detector is studied from 3.4 % to 8% (FWHM) at 3.034 MeV (Q-value of ^{100}Mo).

Fig. B.2 The projected range of electron for ^{100}Mo versus electron energy. Data point is referred to NIST [40].

B. 2 Energy loss in ^{100}Mo foil

In this simulation, the multiple scattering is not taken into account. Electron passes straight line. The NIST data is used to obtain the energy loss, corresponding to electron's path in ^{100}Mo foil. Calculation of the energy loss in the Mo foil is shown in Fig. B.3.

E_i, E_f is the initial and final energy, respectively, when electron loss its energy in ^{100}Mo foil. R_i and R_f is the projected range of ^{100}Mo with respect to E_i and E_f, respectively.

Since electron passes straight. The path length, x, is calculated from the 'vertex_z' and angle θ. The range R_i is obtained from the initial energy E_i. R_f is calculated by subtracting x from R_i. The final energy E_f is obtained from the range R_f.

Here, R_i and E_f are calculated by the interpolation with two adjacent points from the NIST data in Fig. B2.
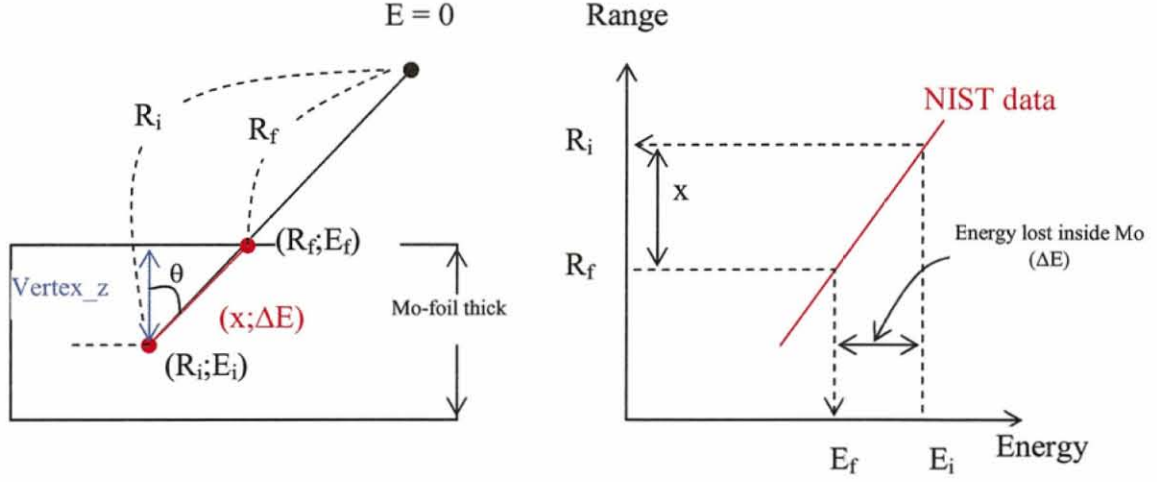

Fig. B.3 Calculation of the energy loss in the ^{100}Mo foil.
    a. The electron passes straight line. No multiple scattering is taken into account.
    b. Calculation the energy loss in ^{100}Mo foil using the NIST data.

B.4 Results and discussions

Fig. B.4 shows the sum energy spectrum of 2ν-$\beta\beta$ (background signal) and 0ν-$\beta\beta$ (signal of interest). Fig. B.4.b shows the energy loss in the foil of 40 mg/cm^2. It is plotted in conditions of $N_{2\nu\text{-}\beta\beta}/N_{0\nu\text{-}\beta\beta}$ ratio of 10^7. This data is used for simulating the detection response with finite energy resolution from 4 % to 8 % (FWHM) at 3.034-MeV region.

Taking into account the detector response as the Gaussian function, Fig. B.5 shows a sum energy spectrum of 2ν-$\beta\beta$ and 0ν-$\beta\beta$ with a finite energy resolution. Fig. B.5a and Fig. B.5b are for 4 % and 6.8 % energy resolution, respectively, at 3.034-MeV energy region. Better energy resolution results in the reduction of 2ν-$\beta\beta$ event background in the signal region. It is good for the detection sensitivity to 0ν-$\beta\beta$ signal.

We estimate the statistical significance from the number of 2ν-$\beta\beta$ events and 0ν-$\beta\beta$ events in the signal region. The signal region is defined at the energy region of $^{0\nu\beta\beta}/_{2\nu\beta\beta}$ ratio $\geq$ 1:1 (shaded area in Fig. B.5). It depends on the energy resolution. The statistical significance of 0ν-$\beta\beta$ event in the signal region is evaluated as [16]:

$$n[\sigma] = \frac{N_{0\nu}}{\sqrt{N_{0\nu} + N_{2\nu}}} \tag{B.2}$$

where, N_{0v} and N_{2v} are the number of events in the signal region for $0v$-$\beta\beta$ and $2v$-$\beta\beta$, respectively. The selected signal region depends on the energy resolution.

We discuss about the statistical significance to the sensitivity to $0v$-$\beta\beta$ signals for different finite energy resolution. The next generation double beta decay experiments, MOON and SuperNEMO, would use about several hundred kg to 1-ton of foil for their detector.

We discuss the sensitivity to the $0v$-$\beta\beta$ half life in 10 ton·year measurement. Fig. B.6a shows the obtained statistical sensitivity, $n[\sigma]$, as a function of the $0v$-$\beta\beta$ half life. The results show that the statistical significance is improved as better energy resolution.

In the next generation double beta decay experiments, MOON and SuperNEMO is interesting the inverted mass hierarchy case. The effective neutrino mass of about 50 meV corresponds to the $0v$-$\beta\beta$ half life of 1.2×10^{26} years [2]. Therefore, we analyze the statistical significance for inverted hierarchy case. Fig. B.6b shows the statistical significance as a function of the energy resolution for inverted mass hierarchy case. The systematic error of the measurement may affect the result. We need to require high statistical significance to be sensitive to $0v$-$\beta\beta$ signals. The energy resolution of 4 % can achieve around 6σ statistical significance to observe the $0v$-$\beta\beta$ decay signal if neutrino mass hierarchy is inverted.
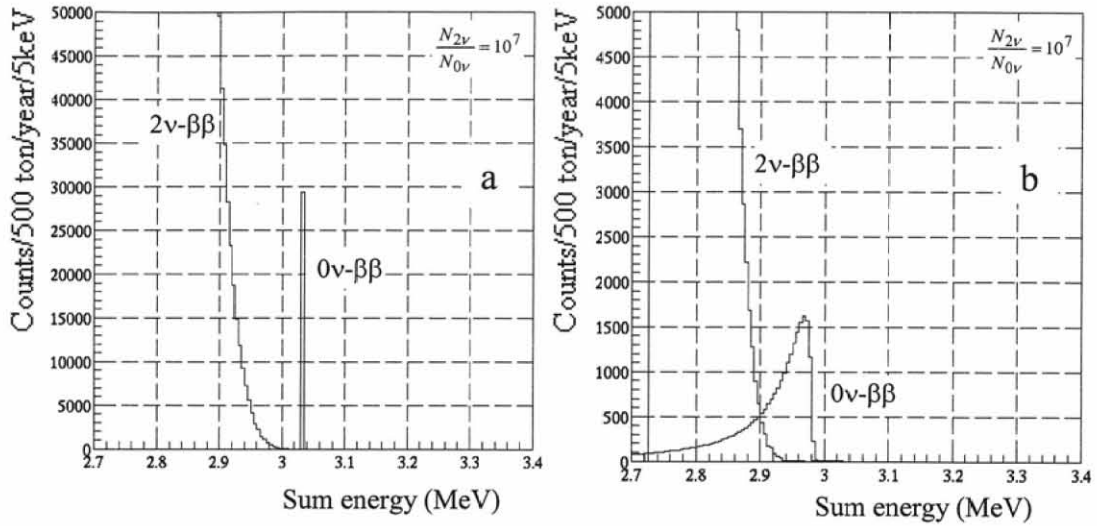
Fig. B.4 The sum-energy spectra of 2ν-ββ (background signal) and 0ν-ββ (signal of interest) with $N_{2\nu}/N_{0\nu} = 10^7$.

a. In ideal condition.

b. 0ν-ββ and 2ν-ββ take into account of the energy loss in ^{100}Mo foil of 40 mg/cm^2 thick.
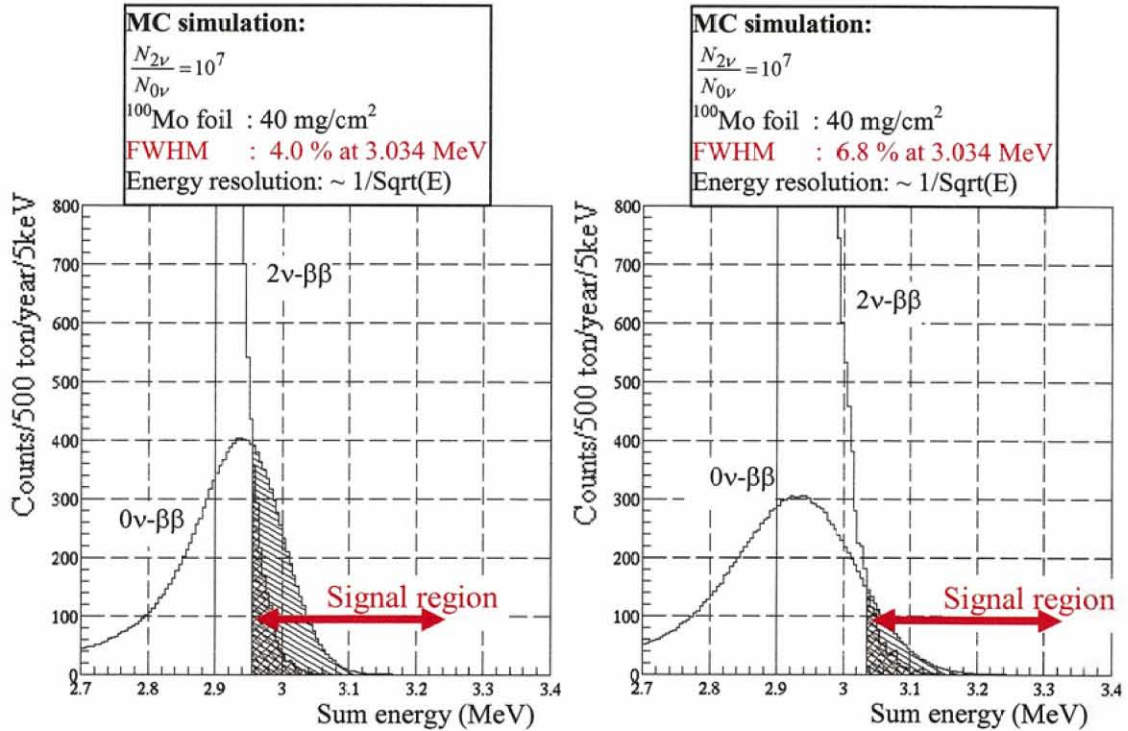
Fig. B.5 The spectrum of 0ν-ββ (signal of interest) and the 2ν-ββ (background signal) with assumptions as following: $N_{2\nu\text{-}\beta\beta}/N_{0\nu\beta\beta}$ ratio is 10^7, the energy loss in ^{100}Mo foil (40 mg/cm^2 thick), and finite energy resolution.

    a.   Energy resolution of 4 % (FWHM) at 3.034 MeV.

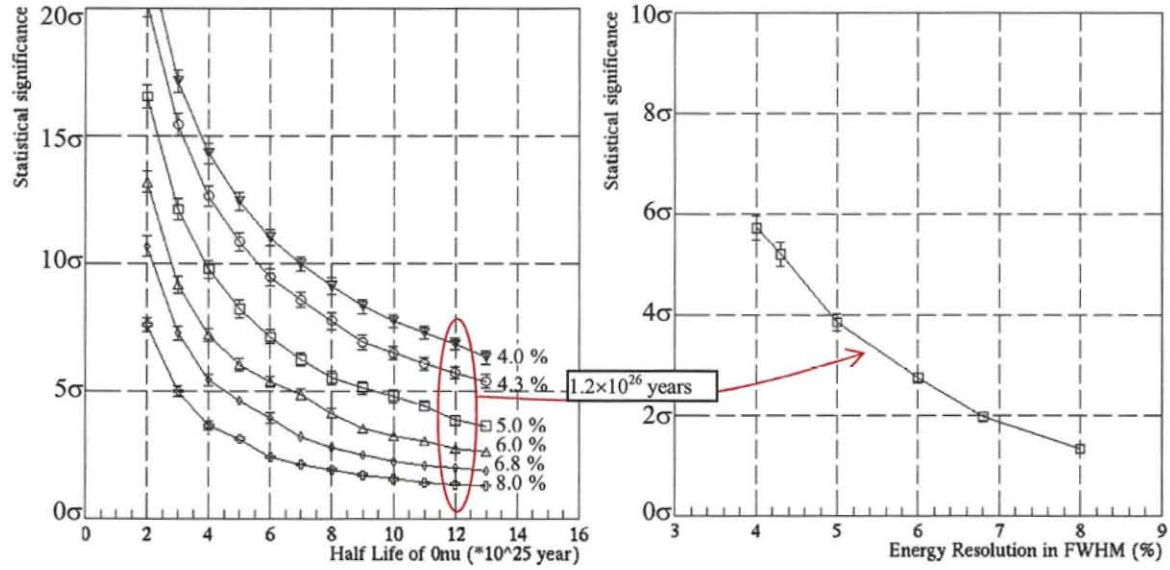   b.   Energy resolution of 6.8 % (FWHM) at 3.034 MeV.

Fig. B.6 a. Statistical significance, n[σ], is plotted against the to the 0ν-ββ half life with different finite energy resolution using 10 ton·year measurement of ^{100}Mo foil. It is for 40 mg/cm^2 thickness. The event number of $N_{0ν}$ and $N_{2ν}$ in the signal region for 10 ton·year data is shown in Fig. B.7.

b. Statistical significance at 0ν-ββ half life of $1.2×10^{26}$ years as a function of the energy resolution.
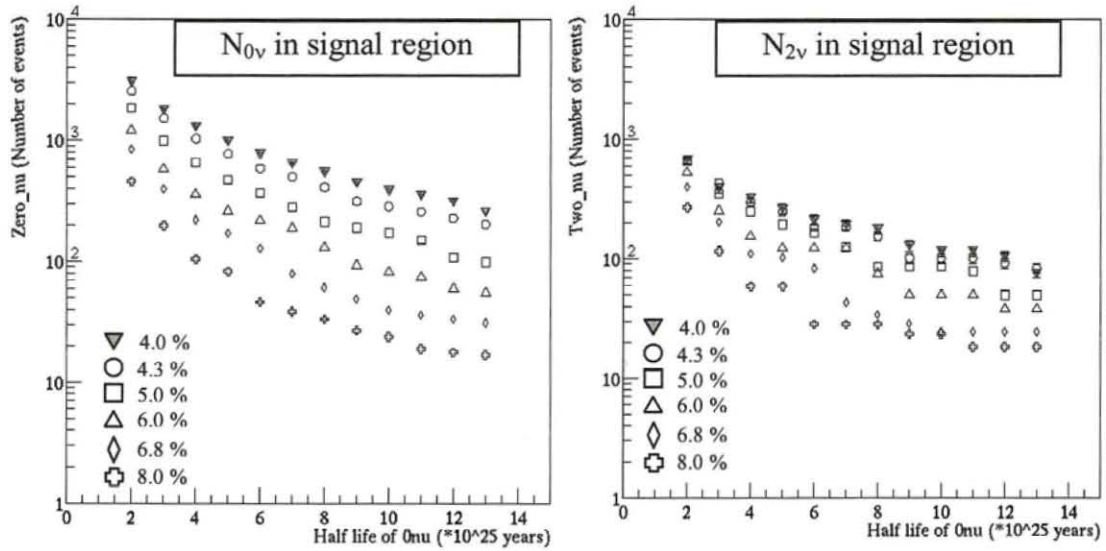

Fig. B.7 The event number of $N_{0ν}$ and $N_{2ν}$ in the signal region for 10 ton·year data.

APPENDIX C

Characteristics of plastic scintillator BC-408

In this section, we describe the characteristics of the plastic scintillator BC-408 (manufactured by BICRON, [21]), which is used for β-ray energy measurement. The properties and the performance test are discussed.

C.1 Properties of BC-408

The properties of the plastic scintillator BC-408 is noted and shown in Table C.1 and Fig. C.1.

Table C.1 The properties of the plastic scintillator BC-408 [21]

Plastic scintillator BC-408	Properties
Chemical name	Polyvinyl Toluene & Organic Flours
Formula	$C_{10}H_{11}$
Ingredient	Polyvinyl Toluene > 97 %; Organic Flours < 3.0 %
Light output	64 % of Anthracene
Rise time	0.9 ns
Decay time	2.1 ns
Pulse Width (FWHM)	2.5 ns
Wavelength of max emission	425 nm
Attenuation Length*	210 cm
Bulk light attenuation length	380 cm
Refractive Index	1.58
Density	1.032
Atomic ratio H/C	1.104
Atomic Density	H. 5.23×10^{22} cm^3; C. 4.74×10^{22} cm^3
No. of Electrons per cc ($\times 10^{23}$)	3.37

* The typical 1/e attenuation length of a 1×20×200 cm^3 cast sheet with edges polished as measured with a bialkali photomultiplier tube coupled to the one end.
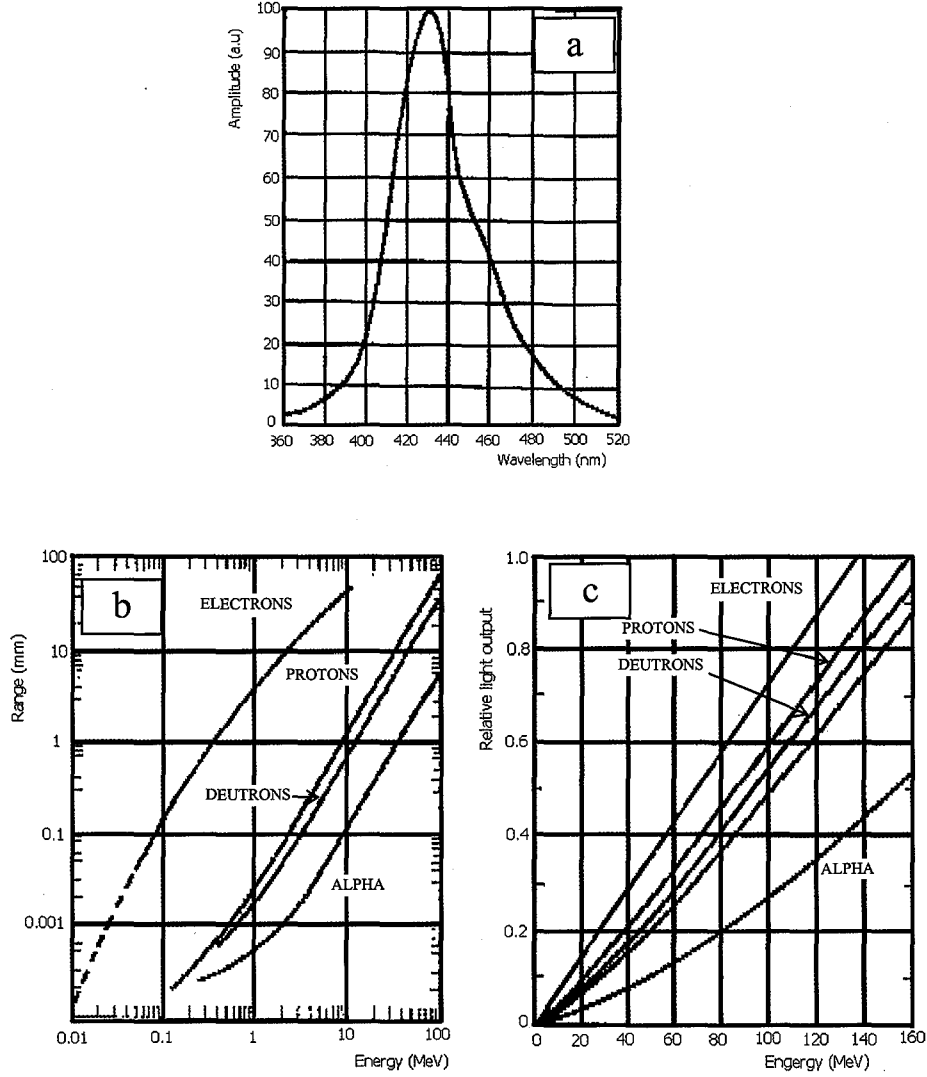
Fig C.1 Properties of plastic scintillator to atomic-particle energies [21]

    a. Emission spectrum of BC-408

    b. Range of atomic particle in mm versus energy (MeV) in plastic scintillator

    c. Scintillator response versus energy (MeV) of atomic particles.

C.2 Emission spectrum of BC-408

It is necessary to measure the emission spectrum of the plastic scintillator with the same condition measurements in this thesis, so as to know the quantum efficiency of the PMT for the scintillation photon.

To measure the spectrum of the plastic scintillator BC-408, a UV-light LED of 375 nm in wavelength (NSHU590A, manufactured by NICHIA [25]) is utilized to excite scintillation. The UV-VIS spectrometer (USB4000 [42]) is used for measuring the emission spectrum of the plastic scintillator BC-408 (6cm×6cm×1cm). The experimental arrangement is shown as Fig. C.2. The position of the LED is set at the

center of plastic scintillator. Photons from the UV-light LED illuminate the plastic scintillator BC-048 through the collimator made of the 2-mm thick dark plastic with hole of 2-mm in diameter. This set-up is arranged similar to the electron and proton measurements i.e. the radiation source is perpendicular to the detector. The emission photons from BC-408 are passed through the optical fiber (P400-2-UV/VIS [42]) and transmitted to the UV-VIS spectrometer. One end of the optical fiber is coupled to the side of BC-408 by the optical grease BC630 [23]. The other end is connected to the optical slit of the spectrometer.

Fig. C.3 shows the scintillation spectrum. It shows different from Fig. C.1a at short-wavelength region. It is because of the attenuation.
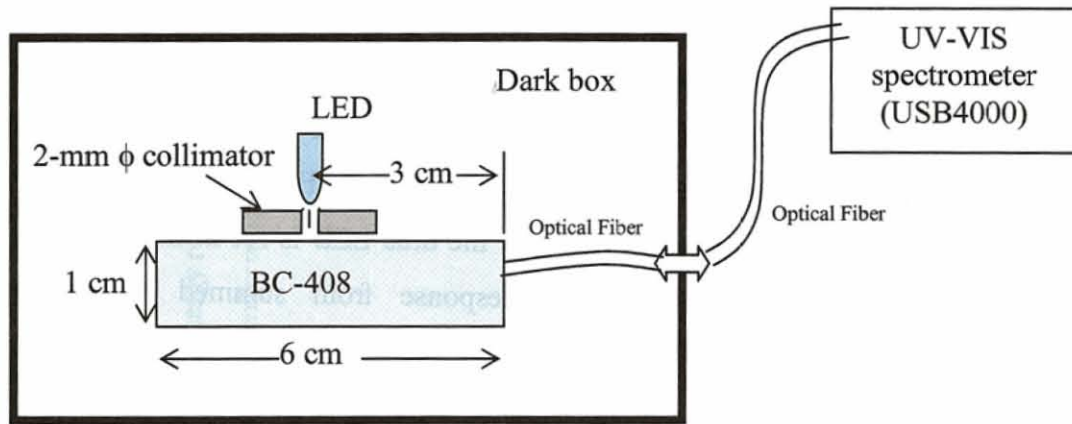

Fig. C.2 Experimental arrangement for measuring the emission spectrum of the plastic scintillator BC-408 by the UV-light LED.
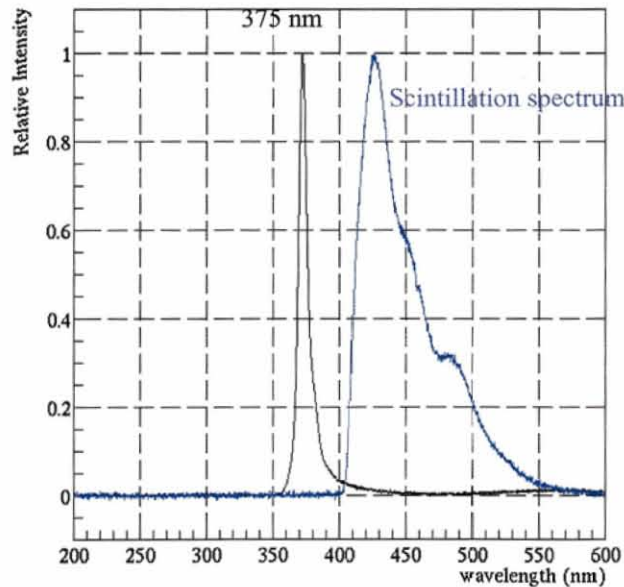

Fig. C.3 Emission spectrum (blue line) of the plastic scintillator BC-408 with the UV-light LED of 375 nm (black line). The peak emission is measured as 425 nm in wavelength.

Appendix D

LED measurement

In this appendix, we discuss the effect of the coherent electrical noise from the detector on the energy resolution. The coherent electrical noise is evaluated through the coherent fluctuation of PMT signals. The LED flash is used to measure the correlation between the PMT signals.

D.1 Set up for LED measurement

For the LED measurement, we use the same scintillation detector which is used for electron and proton measurements. The 470-nm wavelength LED light [25] is transmitted through an optical fiber of 1 mm in diameter and illuminated at the center of the plastic scintillator. One end of the fiber connects directly to the LED, the other end is put at the center of the plastic scintillator. The LED is pulsed by the function generator [42]. Fig. 2.5.1 shows the set-up for LED measurements. The width of pulse is 12-ns. The voltage driven for the blue LED is set from 2.1 volts to 2.5 volts, corresponding to light yield response from summed number of photoelectrons in 4 PMTs from (900 − 4000) photoelectrons.
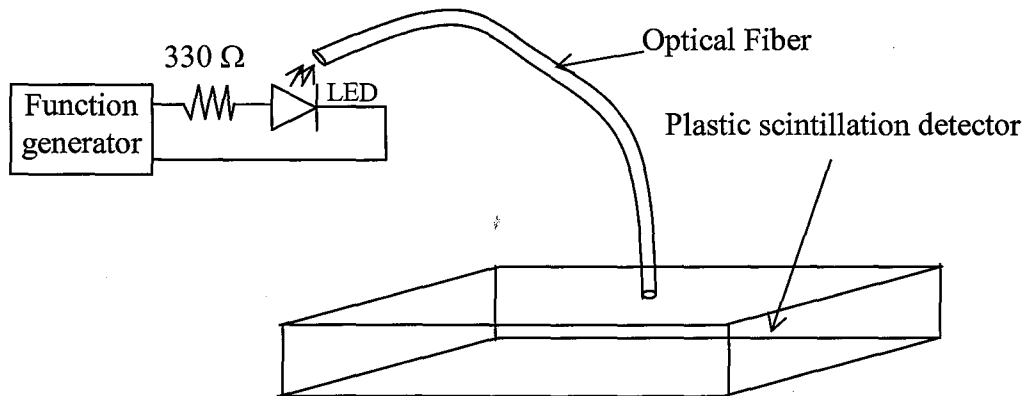

Fig. D.1 Set up for LED measurement.

D.2 coherent electrical noise

In the work, we are interested in the non-statistical component. The coherent electrical noise may affect this component.

We use the 475-nm LED-light flash to measure the correlation of the number of photoelectrons between PMT_{13} and PMT_{24}. Here, PMT_{13} is the summed number of photoelectrons of PMT1 and PMT3; PMT_{24} is the summed number of photoelectrons

of PMT2 and PMT4. The LED measurement was carried out for a full range of ADC channel. Fig. D.2 shows the result of the LED measurement. The upper horizontal scale corresponds to the electron equivalent energy.

We measure the total resolution (square points), which is the variance of the sum of the number of photoelectrons, and the uncorrelated component (triangle points), which is the variance of the difference of the number of photoelectrons. The difference is of those measurements is less than 1% (FWHM).
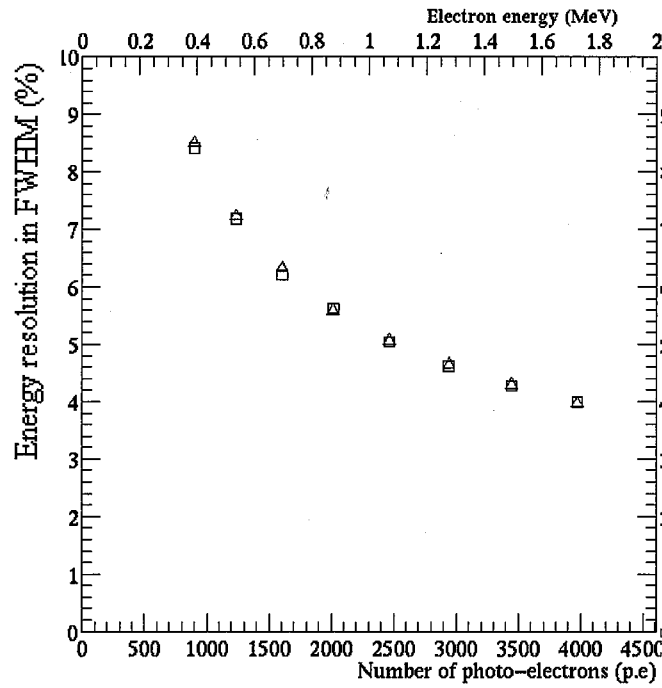

Fig. D.2 The energy resolution versus the number of photoelectrons using LED flash. The upper horizontal scale shows the electron equivalent energy.
Square point is for total resolution in FWHM.
Triangle point is for the uncorrelated component in FWHM.